UNIVERSITÉ DE LORRAINE | BIBLIOTHÈQUES UNIVERSITAIRES

AVERTISSEMENT

Ce document est le fruit d'un long travail approuvé par le jury de soutenance et mis à disposition de l'ensemble de la communauté universitaire élargie.

Il est soumis à la propriété intellectuelle de l'auteur. Ceci implique une obligation de citation et de référencement lors de l'utilisation de ce document.

D'autre part, toute contrefaçon, plagiat, reproduction illicite encourt une poursuite pénale.

Contact bibliothèque : ddoc-theses-contact@univ-lorraine.fr
(Cette adresse ne permet pas de contacter les auteurs)

LIENS

Code de la Propriété Intellectuelle. articles L 122. 4
Code de la Propriété Intellectuelle. articles L 335.2- L 335.10
http://www.cfcopies.com/V2/leg/leg_droi.php
http://www.culture.gouv.fr/culture/infos-pratiques/droits/protection.htm

THÈSE

Présentée et soutenue publiquement le 09 septembre 2025 à Metz pour l'obtention du

DOCTEUR DE L'UNIVERSITE DE LORRAINE

(Science des Matériaux)

par **Ashutosh SINGH**

Development of a Remelting-Aware Modelling Framework for Microstructure Evolution and Mechanical Properties in Laser Powder Bed Fusion

---

Développement d'un cadre de modélisation de l'évolution de la microstructure et des propriétés mécaniques lors de la fusion laser sur des lits de poudre

---

Directeur de thèse :	Pr. Luis Barrales Mora	Professeur associé, Georgia Tech Europe, France
Président de jury :	Pr. Laszlo Toth	Professeur émérite, LEM3, Université de Lorraine, France
Rapporteur:	Pr. Satyam Suwas	Professeur, Department of Materials Engineering, IISC, Inde
Rapporteur:	Pr. K. G. Prashanth	Professeur, Additive Manufacturing Laboratory, TallinnUniversity, Estonie
Examinateur:	Pr. Barbara Previtali	Professeure, Department of Mechanical Engineering, Politecnico Di Milano, Italie
Examinateur :	Dr. Thiebaud Richeton	Chargé de recherche, LEM3, Université de Lorraine, France

Dedicated to….

Dedicated to the memory of the 26 innocent lives lost in the barbaric terrorist attack of 22 April 2025 in Pahalgam, India, and to my beloved family.

22 अप्रैल 2025 को भारत के पहलगाम में हुए बर्बर आतंकवादी हमले में जान गंवाने वाले 26 निर्दोष लोगों की स्मृति और अपने पूरे परिवार को समर्पित……

न हि ज्ञानेन सदृशं पवित्रमिह विद्यते ।
तत्स्वयं योगसंसिद्धः कालेनात्मनि विन्दति ॥

There exists no purifier similar to the knowledge. The purity of other things is due to the touch of Consciousness and is not intrinsic.

Il n'existe pas de purificateur semblable à la connaissance. La pureté des autres choses est due au contact de la conscience et n'est pas intrinsèque.

~Bhagavad-gītā 4.38

Acknowledgement

Before moving forward, I would like to express my gratitude to all those without whom completing this thesis would not have been possible at all.

First and foremost my sincere gratitude to my supervisor, Professor Luis Barrales Mora, for his continuous support, guidance, and trust in me during my doctoral trajectory. His scientific direction and patience helped shape both my research and personal development.

I would also like to thank Professor Surya Kalidindi and the entire MINED Lab at Georgia Tech, Atlanta, for the valuable time I spent there. Their technical inputs, teamwork, and helpful discussions were very important in shaping this project. I also appreciate Professor Daniel Barba and his team at the Universidad Politécnica de Madrid, where I spent some months of experimental activity and high-level material characterization. I would also like to state the immeasurable support and collaboration of Professor Christian Haase from Technische Universität Berlin, whose comments shaped several key issues in this thesis and scientifically enhanced the project.

My sincerest appreciation is extended to the members of my thesis follow-up committee: Professor Stéphane Berbenni from Université de Lorraine, France; Professor Ali Gökhan Demir from Politecnico di Milano, Italy; and Professor Francisco Javier Mountains, with a double affiliation to Universidad Politécnica de Madrid and the University of Florida, for their thoughtful early revisions, constructive comments, and consistent participation that worked to orient this research in productive directions. This Ph.D. research was carried out in the framework of the European Union Horizon 2020 XS-Meta Project that not only financed the scientific and logistic part of the research, but also provided an intellectually challenging and multicultural environment for collaboration.

This project has received funding from the European Union's Horizon 2020 research and innovation programme under the Marie Skłodowska-Curie Grant Agreement No. 956401

Special thanks to Miss Christina Corduri of IRL 2958, who provided frequent assistance on various technical and administrative matters related to the mission. I am grateful to Professor Jean-Paul Salvestrini, Director of IRL 2958, for ensuring a pleasant and conducive research environment during my time at GeorgiaTech Europe.

To my friend and colleague Jialiang Chen, I express hearty thanks for the many hours of joint work, scientific discussion, and the spirit of collegiality that made this long process more rewarding. I am also profoundly thankful to my friends Ashutosh**,** Vishnu, Vineet, Ikhtihaam, and Abhishek for their direct and indirect support throughout my time living in France.

I am indebted to my wife, Aditi Singh, for standing by me with unwavering support, patience, and belief. She provided me with strength at the most challenging times. I'm also deeply thankful to my parents, Dr. Arvind Singh and Mrs. Pratima Singh, my brother Abhishek Kumar,my sisters Kusum, Vandana, Rashmi , my sister-in-law Rishu Singh, and the entire Singh family, whose unflinching encouragement and love constituted the foundation of all my efforts. Their influence went far beyond just encouragement; they taught me values like discipline, integrity, and sound morals that continue to guide me on my path, both as an academic and as a person.

Finally, I offer my sincere gratitude to the creator, whose guidance and grace have followed me through every step along the way. Anything that I have achieved, and anything that I have become today, is through His/Her will and blessing.

This project has received funding from the European Union's Horizon 2020 research and innovation programme under the Marie Skłodowska-Curie Grant Agreement No. 956401

Table of Contents

Dedicated to…. iii

Acknowledgement v

List of Tables xi

List of Figures xiii

List of Abbreviations ii

List of Symbols iv

Introduction 1

Chapter 1 6

Literature Review 6

1.1 Introduction 6

1.2 Laser Powder Bed Fusion Process 6

1.3 Solidification 10

1.3.1 Preliminary Concepts 10

1.3.2 Nucleation 11

1.3.2.1 Homogenous nucleation 11

1.3.2.2 Heterogeneous nucleation 13

1.3.2.3 Dominant Nucleation Mechanism in LPBF 15

1.3.3 Crystal Growth and Interface Stability 16

1.3.4 Grain Structure Evolution in LPBF 18

1.3.4.1 Epitaxial Growth and Columnar Grains 19

1.3.4.2 Columnar-to-Equiaxed Transition (CET) 19

1.3.5 Texture Development and Mechanism 20

1.3.5.1 Solidification Texture 21
1.3.5.2 Deformation Texture 21
1.3.5.3 Recrystallization Texture 22
1.3.5.4 Texture Development Mechanism in LPBF 23
1.4 Microstructure Modelling Techniques 23
1.4.1 Phase-Field Modelling 24
1.4.2 Kinetic Monte Carlo 28
1.4.3 The Cellular Automaton Method 31
1.5 Conclusion 35
Chapter 2 38
Development of a Remelting-Aware 3D Cellular Automaton (RA-CA) Model 38
2.1 Introduction 38
2.2 The CA model 39
2.3 Nucleation Mechanisms 42
2.4 Crystal growth and crystallographic orientation 46
2.4.1 Crystallographic orientations of the nuclei 46
2.4.2 Kinetic growth model 49
2.4.3 Crystal growth 52
2.5 Coupling of finite element method and cellular automaton 53
2.6 Parallelization technique 55
2.7 A novel algorithm handling redundancies arising from remelting in LPBF 57
2.8 Conclusion 60
Chapter 3 63
Model Validation 63
3.1 Introduction 63

3.2 RA-CA Simulation Setup 64
3.2.1 Thermal Field Generation 66
3.2.2 Effect of Nucleation type 67
3.2.2.1 Grain Morphology and Surface Structure 68
3.2.2.2 Texture and Orientation Distribution 70
3.2.3 Effect of growth kinetics 74
3.3 Conclusion 77
Chapter 4 80
Microstructure development in a LPBF-processed Steel 80
4.1 Introduction 80
4.2 Experimental Procedure 80
4.2.1 Microstructural Characterization of LPBF-Processed X30Mn21 82
4.2.1.1 Grain Morphology and Crystallographic Orientation 83
4.2.1.2 Grain Size and Aspect Ratio Distributions 85
4.3 RA-CA Simulation Analysis 87
4.3.1 CA Simulation Setup 87
4.3.2 Microstructural Characterization of Simulated X30Mn21 88
4.3.2.1 Grain Morphology and Crystallographic Orientation 89
4.3.2.2 Grain Size and Aspect Ratio Distribution 92
4.3.3 Comparison between Simulations and Experiments 94
4.3.4 Morphology Comparison and Statistical Comparison 94
4.3.5 Texture and Orientation Comparison 96
4.4 Efficiency of the Cellular Automaton model and simulation setup 98
4.5 Discrepancies between Simulation and Experiment 99
4.6 Conclusions 100

Chapter 5 103

Effect of Preheating on Microstructure and Property Relationships in LPBF-Processed X30Mn21 103

5.1 Introduction 103

5.2 RA-CA Simulation Setup 104

5.3 Overview of the Crystal Plasticity Finite Element Method 107

5.4 Microstructure Evolution under Different Preheating Temperatures 110

5.4.1 Grain Morphology and Crystallographic Orientation 111

5.4.2 Grain Size Distributions 114

5.4.3 Mechanical Behavior and P–S–P Linkage 116

5.5 Conclusion 118

Chapter 6 121

General Conclusion and Future Scope 121

6.1 Limitations of the Present Model 123

6.2 Future Scope 124

Funding 126

Appendix A: Pseudocode Algorithms 127

A.1 Generate Uniform Random Quaternion 127

A.2 Final Solidification Time Tracking (CA Cell Activation) 128

Abstract 130

Résumé 132

Bibliography 134

Extended Summaries in French 152

List of Tables

Table 1.1 Preferred growth direction of the lattices structure 21
Table 1.2 A Comparative Overview of Microstructure Modeling Techniques in LPBF 36
Table 2.1 Transition rule of CA cells 41
Table 3.1 Thermo-physical properties of X30Mn21 and calculated growth coefficients 65
Table 3.2 Nucleation density for different simulation 68
Table 3.3 Growth coefficient values $\alpha \; and \; \beta$ used in the simulations to investigate the influence of solidification kinetics on microstructure evolution 76
Table 4.1 LPBF process parameter 81
Table 4.2 Chemical compositions of X30Mn21 metal powder 82
Table 4.3 RA-CA model parameters 88
Table 5.1 Melt pool dimensions obtained from ABAQUS thermal simulations at different preheating temperatures. 105
Table 5.2 RA-CA model parameters 106
Table 5.3 LPBF process parameters for the microstructure simulation 107

List of Figures

Figure 1.1 Laser Powder Bed Fusion Process 7
Figure 1.2 Simplified Ishikawa/fishbone for LPBF 7
Figure 1.3 SEM images showing two types of porosity observed in LPBF-processed parts. (a) Lack of fusion defect due to insufficient energy input, with irregular pore shapes and unmelted powder particles and, (b) Gas-induced porosity formed under high energy conditions, characterized by spherical pores [36]. 8
Figure 1.4 Schematic of the solidification of liquid metal: (a) Initial nucleation with dispersed nuclei in the liquid phase, (b) Growth of dendritic structures from the nuclei, representing directional solidification, and (c) Final microstructure with well-defined grains separated by grain boundaries. 10
Figure 1.5 Free-energy relationship with radius of growing spherical nuclei during solidification 13
Figure 1.6 Spherical crystal formation on the heterogeneous surface material 14
Figure 1.7 Different morphology of the solid/liquid interface: (a) planar interface,(b)cellular interface,(c)columnar interface and, (d) dendritic interface 16
Figure 1.8 Effect of cooling rate and temperature gradient on the morphology 17
Figure 1.9 Schematic illustrations of typical grain structures formed during directional solidification in casting. (a) Pure metals showing a chill and columnar zone; (b) solid-solution alloys with a central equiaxed zone; (c) structure with full equiaxed grains 18
Figure 1.10 A drawn wire with preferential ⟨110⟩ direction parallel to drawn axis (b) A rolled sheet showing three grains with different orientations: Grain 1 with (001) [010], grain 2 with (110) [001], and grain 3 with (001) [110] 22
Figure 1.11 (a) Simulated solute concentration field during rapid solidification of Ti-6Al-4V at the dendritic scale, resolved at 30 nm, under a high cooling rate of 50,000 K/s;(b) Phase-field simulation at the grain scale for electron beam powder bed fusion (E-PBF) of Ti-6Al-4V, with spatial resolution of 100 nm, using a beam power of 420 W and scan speed of 0.8 m/s 27
Figure 1.12 Schematic of a KMC modelling technique 29
Figure 1.13 Schematic of the Cellular Automaton (CA) modeling framework for LPBF microstructure simulation. Each cell in the 3D lattice stores four key parameters: state (S), temperature (T), orientation (O), and grain index (I). 32
Figure 2.1 (a) 3D CA representation: green, blue, red, and white represent solidified, liquid, growing and powder cells, respectively. Each cell stores its state (S), temperature (T), crystallographic orientation (O) and the unique index (I); (b) 2d representation..... 40
Figure 2.2 Von-Neumann neighborhood configuration: (a) in 2 dimension space and, (b) in 3 dimensional space 42
Figure 2.3 Moore's neighborhood configuration: (a) in 2-dimension space and, (b) in 3 dimensional space 42
Figure 2.4 Schematic representation of the type of nucleation considered 43
Figure 2.5 Flowchart for the nucleation algorithm within CA model 45

Figure 2.6 Flowchart explaining the assignment of crystallographic orientation to the nuclei based on the thermal gradient 49
Figure 2.7 A regular octahedron depicting the preferential growth direction of the primary dendrites..... 53
Figure 2.8 (a) Coarser FEM mesh overlapping fine mesh of CA; (b) schematic representation of the tri-linear interpolation technique. 55
Figure 2.9 (a) RVE domain decomposed into 4 subdomains, dashed lines represent the subdomain boundaries, subdomain 1 and subdomain 4 contain active nuclei N1 and N2, a, b and c represent the cells via which the nuclei touch the boundary. (b) When nuclei encounter the subdomain boundaries, additional ghost layers (a', a", b', b", c', c") are introduced to ensure proper information transfer across subdomains, thereby allowing growth to be tracked consistently without discontinuities. 57
Figure 2.10 Schematic representation of the framework for avoiding redundancy because of remelting in LPBF: (a) RVE representing the growth of dendrites at a time t_{n-1}: green cells are solidified, blue cells are liquid state, hatched cells will be re-melted at next time interval and therefore, are not available for nucleation and crystal growth, red cells are growing cells with activated nuclei; (b) RVE representing the cells after complete solidification at time t_i ($t_i > t_{n-1}$), where black cells represent the cells that were melted at t_{n-1} and will be melted again at t_n ($t_n > t_i > t_{n-1}$) and were never activated in the previous time step; (c) RVE of the cells at time t_n, where several cells have melted again and were activated based on their respective temperature profile. 58
Figure 2.11 Temperature-time profile of cell R in Figure 2.10: this cell melts twice during the process, namely at tn-1 and tn..... 59
Figure 2.12 Program flowchart where $M \times N \times O$ processes are started in parallel. Data is globally shared before domain subdivision. Once parallel execution begins, all tasks are performed locally with communication exchanges occurring periodically. Execution continues until the AM process ends or the full melting of the powders and solidification are completed, or the maximum user-defined maximum solidification time is reached 61
Figure 3.1 Growth velocity as a function of undercooling for X30Mn21 alloy wherein the red circles represent LGK model calculations, while the dashed line shows the second-order polynomial fit used in the RA-CA simulations. $\boldsymbol{\alpha}$ and $\boldsymbol{\beta}$ are the polynomial coefficients 65
Figure 3.2 Temperature dependent thermos-physical properties X30Mn21 alloy (a) specific heat, (b) thermal conductivity, (c) density and,(d) Isometric section of the thermal simulation indicating the sub-section taken for CA simulation 67
Figure 3.3 Simulated grain morphologies (top row) and corresponding top view (bottom row) for different nucleation strategies: (a, d) only bulk, (b, e) only epitaxial, and (c, f) both bulk and epitaxial nucleation. Section planes are marked in the 3D views. 70
Figure 3.4 IPF map of the Y-X section (a) only bulk, (b) only epitaxial, and (c) both bulk and epitaxial nucleation. 72
Figure 3.5 The IPF of Y-X section of the RA-CA simulation with of RA-CA simulation with (a) only bulk, (b) only epitaxial, and (c) both bulk and epitaxial nucleation 72

Figure 3.6 IPF map of the Y-Z section of RA-CA simulation with (a) only bulk, (b) only epitaxial, and (c) both bulk and epitaxial nucleation 73
Figure 3.7 The IPF of Y-Z section of the RA-CA simulation with of RA-CA simulation with (a) only bulk, (b) only epitaxial, and (c) both bulk and epitaxial nucleation 73
Figure 3.8 Simulated 3D grain morphologies and cross-sectional views illustrating the influence of solidification kinetics on microstructure evolution. (a–c) 3D grain structures obtained using (a) reduced growth kinetics(simulation 1), (b) baseline growth kinetics fitted from Equation 2.25 (simulation 2), and (c) enhanced growth kinetics (simulation 3). (d–f) Top surface views corresponding to each scenario, showing the distribution and size of grains at the build surface. (g–i) YZ cross-sectional views highlighting the columnar growth morphology and extent of grain impingement. 77
Figure 4.1 (a) EBSD inverse pole figure (IPF) map of the X30Mn21 specimen, with BD as the reference axis, (b) a magnified view, highlighting alternating <101> and <100> orientations and finer sub grain features ... 82
Figure 4.2 The IPF for X30Mn21 fabricated with LPBF 84
Figure 4.3 Pole figures <100>, <101> and, <111> crystallographic direction for specimen fabricated with LPBF 84
Figure 4.4 Histogram of grain size distribution obtained from experiments 86
Figure 4.5 Histogram of grain aspect ratio distribution obtained from experiments 86
Figure 4.6 Isometric view of the simulated grain structure at different CA cell sizes: (a) d_{cell}= 2 µm and (b) d_{cell} = 0.8 µm. 89
Figure 4.7 IPF map of the X30Mn21 sample obtained with: (a) RA-CA simulation with CA cell size of d d_{cell}= 2 µm; (b) RA-CA simulation with CA cell size of d_{cell}= 0.8 µm 90
Figure 4.8 The IPF for X30Mn21 (a) RA-CA simulation with CA cell size of d d_{cell}= 2 µm; (b) CA simulation with CA cell size of d_{cell}= 0.8 91
Figure 4.9 Pole figures <100>, <101> and, <111> crystallographic direction for: (a) CA simulation with CA cell size of d_{cell}= 2 µm; (b) CA simulation with CA cell size of d_{cell}= 0.8 92
Figure 4.10 Histogram of grain size distribution obtained from simulation 93
Figure 4.11 Histogram of grain aspect ratio distribution obtained from simulation 94
Figure 4.12 Pair Correlation Functions (PCF) of microstructures obtained by simulation and experiment. 96
Figure 4.13 Pole figures subtraction of: (a)RA-CA simulation with cell size of 2 µm and experiment; (b RA-CA simulation with cell size of 0.8um and experiment 97
Figure 4.14 Computational time and the efficiency of parallelization of the 3D CA model. 99
Figure 5.1 Longitudinal and cross-sectional views of melt pool profiles at different preheating temperatures obtained from ABAQUS thermal simulations 105
Figure 5.2 A schematic of laser scan pattern 106
Figure 5.3 3D grain morphologies, IPF map across the portioned section and corresponding IPF of the simulated microstructure of X30Mn21 113
Figure 5.4 Cooling rate along the center of the melt pool depth at different pre-heat temperature 114
Figure 5.5 Simulated average grain size of X30Mn21 at different preheat temperatures in comparison with experimental grain sizes reported by Köhnen et al. [119]under similar LPBF conditions. 115

Figure 5.6 Grain size distribution and cumulative frequency plots for X30Mn21 simulated at different preheat temperatures. 116
Figure 5.7 a) tensile test stress strain relations, (b) 0.2% yield strength for different preheating temperatures 117

List of Abbreviations

Abbreviation	Full Form
AM	Additive Manufacturing
CA	Cellular Automaton
CAFE	Cellular Automaton Finite Element
CAD	Computer-Aided Design
CLM	Crystallographic Lamellar Microstructure
CP-FEM	Crystal Plasticity Finite Element Method
DED	Directed Energy Deposition
EB-PBF	Electron Beam Powder Bed Fusion
EBSD	Electron Backscatter Diffraction
FCC	Face-Centered Cubic
FEM	Finite Element Method
HD	Hatch Distance
IPF	Inverse Pole Figure
ISHKAWA	Ishikawa Diagram (Cause-Effect)
KGT	Kurz-Giovanola-Trivedi Model
KMC	Kinetic Monte Carlo
LGK	Lipton-Glicksman-Kurz Model
LPBF	Laser Powder Bed Fusion
MAM	Metal Additive Manufacturing
MPI	Message Passing Interface
MTEX	MATLAB Texture Toolbox
ODF	Orientation Distribution Function
PCF	Pair Correlation Function

PF	Phase Field
PFM	Phase Field Method
P–S–P	Process–Structure–Property
RA-CA	Remelting-Aware Cellular Automaton
RVE	Representative Volume Element
SLM	Selective Laser Melting
STL	Stereolithography
TWIP	Twinning-Induced Plasticity
TRIP	Transformation-Induced Plasticity

List of Symbols

Symbol	Definition	Unit
S	Total surface area	m^2
T_m	Melting temperature	°C
T_l	Liquidus temperature	°C
σ	Standard deviation of the nucleation distribution	-
μ	Mean of the probability function	°C
T_{max}	Maximum temperature	°C
V	Total volume	m^3
N_v	Number of nuclei per unit volume	m^{-3}
N_s	Number of nuclei per unit surface area	m^{-2}
ΔT	Undercooling	°C
G	Thermal gradient	K/m
R	Solidification rate	m/s
r*	Critical nucleus radius	m
q	Quaternion component	-
C_p	Specific heat capacity	J/kg·K
L	Latent heat of fusion	J/kg
α	Thermal diffusivity	m^2/s
Γ	Gibbs-Thomson coefficient	K·m
Pe	Peclet number	-
v	Growth rate	m/s
Φ_1	Euler angle 1 (rotation about Z axis)	rad
Φ	Euler angle 2 (rotation about X’ axis)	rad

Φ_2	Euler angle 3 (rotation about Z'' axis)	rad
γ	Surface energy or Gibbs free energy	J/m²
Ω	Solid angle in orientation space	sr
ΔG	Change in Gibbs free energy	J
f	Phase-field order parameter	-
c	Solute concentration	wt%
M	Mobility constant	-
η	Viscosity or another material parameter	Pa·s
F	Total deformation gradient	-
$\mathrm{F_e}$	Elastic deformation gradient)	-
$\mathrm{F_p}$	Plastic deformation gradient	-
$\dot{F}_\mathrm{p}$	Rate of change of the plastic deformation gradient	s^{-1} (tensor rate)
$\mathrm{L_p}$	Plastic velocity gradient	s^{-1}(tensor)
f_{tw}	Volume fraction of twinned regions	-
f_{tr}	Volume fraction of transformed regions	-
$\dot{\gamma}$	Shear rate on slip/twin/transformation system	s^{-1}
N_S	Total number of slip systems	-
N_{tw}	Total number of twinning systems	-
N_{tr}	Total number of transformation systems	-
s	Slip direction unit vector	-
m	Slip plane normal unit vector	-
η	Viscosity or another material parameter	Pa·s
ρ_m	Mobile dislocation density	m^{-2}
$\dot{\rho_m}$	Rate of change of mobile dislocation density	$m^{-2}.s^{-1}$

D	Average grain size	m
λ_s	Mean spacing between dislocation obstacles	m
λ_{ts}	Mean spacing between twinning obstacles	m
λ_{tr}	Mean spacing between transformation obstacles	m
b_s	Burgers vector magnitude	m
$\hat{d}$	Dipole formation parameter	-

Introduction

Additive manufacturing (AM) is an innovative manufacturing technique in which complex components with high material efficiency and design flexibility could be fabricated with ease. Unlike traditional subtractive methods, AM builds parts layer by layer, allowing for intricate geometries that are otherwise difficult or impossible to fabricate [1]. This novelty of AM has spurred extensive research efforts on AM for the past couple of decades. Additive manufacturing has initially emerged as a prototyping tool, however, with the development of process like laser powder bed fusion (LPBF), directed energy deposition (DED), electron beam powder bed fusion (EB-PBF), AM evolved to include metal additive manufacturing (MAM) which in this era is being considered as a potential replacement to the conventional manufacturing techniques [2]. In sectors such as aerospace, automobile, biomedical where the components need to be very specific and sometimes very complex, the transition from conventional manufacturing techniques to metal additive manufacturing (MAM) has already begun [3]. The LPBF technique is one type of MAM which utilizes a high-quality laser as an energy source to selectively fuse metallic powder and create three-dimensional components [4].

Among all the AM techniques, LPBF has become a leading technique for manufacturing near-net-shape metallic parts. LPBF employs a laser beam, which scans the layer of powder in a controlled trajectory and induces melting and solidification of the material locally. As a layer-by-layer manufacturing process, LPBF can produce near net shape parts of any complex design and structure, and thus it is a highly desired technique among the industries [5–7]. One of the key advantages of LPBF is also its potential to locally tailor mechanical properties by controlling the microstructure. In LPBF, this is possible due to the process's highly localized thermal input, which allows designers to fine-tune the microstructure at specific regions of a component. By adjusting scan speed, hatch spacing, or laser power, it is feasible to intentionally

promote columnar versus equiaxed grain growth, ultimately enabling site-specific performance optimization within the same part [8]. Furthermore, it is possible to change the local chemical compositions to obtain graded materials. Therefore, understanding the mechanisms governing microstructure evolution during LPBF is a topic of immense interest.

LPBF, although having manufacturing capabilities and design flexibility, is yet to reach its potential. One of the major challenges lies in the microstructure, texture, and mechanical properties of components manufactured through LPBF, which often exhibit notable distinctions from those produced through conventional processes [9,10]. This deviation is mainly attributed to the rapid solidification rates and high thermal gradients inherent in the LPBF process. Moreover, the range of materials that could be processed using LPBF is limited which also adds up to the challenges that AM is facing in the current scenario. In practise, a rigorous experimental campaign is designed whenever a new material must be processed with LPBF. Additionally, LPBF involves numerous process variables, namely, laser power, scan speed, hatch distance, and layer thickness that result in a vast parameter space which renders almost impossible to conduct comprehensive experimental studies [6,7,9,11].

To address these limitations, computational modelling techniques are increasingly used as alternatives or complements to experimental work. Various modelling approaches have been proposed which includes Phase Field (PF) [12,13], Kinetic Monte Carlo (KMC) [14,15], and Cellular Automaton (CA) [16–20]. Each with their own capabilities and drawbacks. PF models provide detailed simulation of dendritic growth and solute redistribution but are computationally intensive and limited in scale [21]. KMC models offer statistical efficiency and scalability but lack physical coupling with crystallographic fields [12]. CA models strike a balance by offering relatively efficient simulations while capturing important physical phenomena like grain morphology and texture evolution [22,23].

Existing CA models have been effectively used to simulate nucleation and grain growth during solidification in LPBF. However, two major limitations persist: (i) the need for high-resolution grids to capture fine dendritic features, which increases computational load, and (ii) the lack of efficient strategies to handle remelting cycles, which are a fundamental aspect of LPBF. As studies suggest, up to 80% of the build volume may undergo remelting, which introduces computational redundancy and significantly increases simulation time [24]. Although parallelization strategies have been adopted to manage computational load from fine cell sizes [16,25], there is a lack of literature addressing redundancy specifically caused by repeated remelting-solidification cycles.

To address these challenges, the main objective of this thesis is to develop an accelerated Finite Element (FE) CA model framework tailored for LPBF. This has been achieved through the following specific objectives:

1. Eliminate computational redundancy associated with remelting cycles in LPBF by introducing a remelting-aware tracking algorithm that records the thermal history of each cell and selectively processes only the final solidification event, thereby developing a Remelting Aware Cellular Automaton Model (RA-CA).
2. Improve computational efficiency by parallelizing the developed framework using the Message Passing Interface (MPI) to enable simulation of large representative domains.
3. Incorporate realistic microstructural physics by integrating a detailed stochastic nucleation mechanism and a kinetic growth model governed by local thermal gradients and crystallographic orientation.
4. Establish a Process–Structure–Property (P–S–P) linkage by coupling the simulated microstructural features with CP-FEM to evaluate their influence on mechanical behaviour.

This thesis is structured in six chapters. Following the introduction, extensive literature review is covered in Chapter 1. The chapter begins with an overview of the LPBF technique and then discusses the fundamentals of solidification, including nucleation, crystal growth, and texture development. A major part of the chapter is dedicated to reviewing different microstructure modelling approaches, such as Phase-Field, Kinetic Monte Carlo, and Cellular Automaton methods, with particular attention given to their application in LPBF.

The developed accelerated three-dimensional Cellular Automaton (CA) model is detailed in chapter 2. It describes the nucleation mechanism, crystal growth, and the incorporation of crystallographic orientation into the model. The chapter discusses the implementation of noble algorithm that eliminates redundancies arising from remelting during LPBF along with parallelization technique

Chapter 3 focuses on the results obtained from the simulations carried out using the developed CA model. The simulations are analyzed to understand the grain evolution, texture development, and solidification behaviour under various simulation parameters. Chapter 4 deals with the validation of the simulation results using experimental data. The experimental study was carried out using X30Mn21 high-manganese steel, and the simulated microstructure is compared with the experimentally observed one, both qualitatively and quantitatively.

In chapter 5, the impact of varying powder bed preheat temperatures on microstructure evolution in LPBF is examined computationally using the developed RA-CA model. The study explores how preheating influences grain morphology and texture, and links these structural changes to mechanical performance through crystal plasticity finite element (CP-FEM) simulations, thereby establishing a process–structure–property relationship .Finally, chapter 6 concludes this thesis and outlines the possible directions for future investigation.

Chapter 1

Literature Review

1.1 Introduction

This chapter presents a focused literature review on the LPBF process, emphasizing the solidification behavior that governs grain structure and texture formation. Key process parameters, crystallographic mechanisms, and the fundamentals of microstructure modeling techniques are discussed to provide a basis for the model development in later chapters.

1.2 Laser Powder Bed Fusion Process

Laser Powder Bed Fusion (LPBF) is one of the major Additive Manufacturing (AM) processes, wherein a moving laser selectively melts metallic powder to build a 3D object layer by layer[6]. This technique enables the direct fabrication of near-net-shape components from a digital CAD model. Typically, the CAD model is converted into a stereo-lithography (STL) file, which is then sliced into thin layers. These individual layers are sequentially fused to form the final component using laser energy. Due to its layer-wise fabrication approach, LPBF is classified as a layer-by-layer technique. A general configuration of the LPBF process is shown in Figure 1.1. The set up essentially, includes a laser which is the energy source for melting the melting powder, build chamber/platform which hold the part being fabricated, powder delivery chamber,

waste powder collector which collect that excess powder and a re-coater which spread the powder as each layer to be printed.

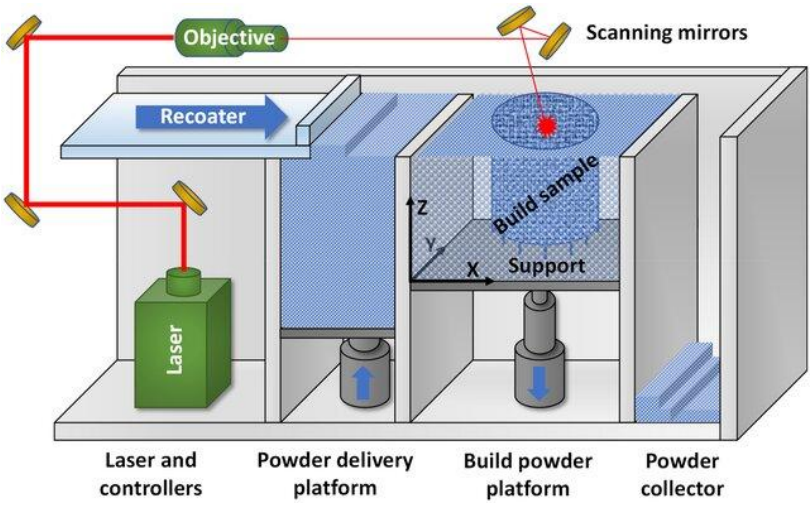


Figure 1.1 Laser Powder Bed Fusion Process [26]

The fabrication of the part is carried out in an inert environment. According to literature most studied process parameters of LPBF include: the laser power[27], the scan speed of laser[28], the layer thickness [29], the laser spot diameter [30], the hatch distance [4], the pre-heat bed temperature [31], the laser emission mode [32], and the scan strategy [33] among others. Figure 1.2 illustrates more exhaustively the process parameters.

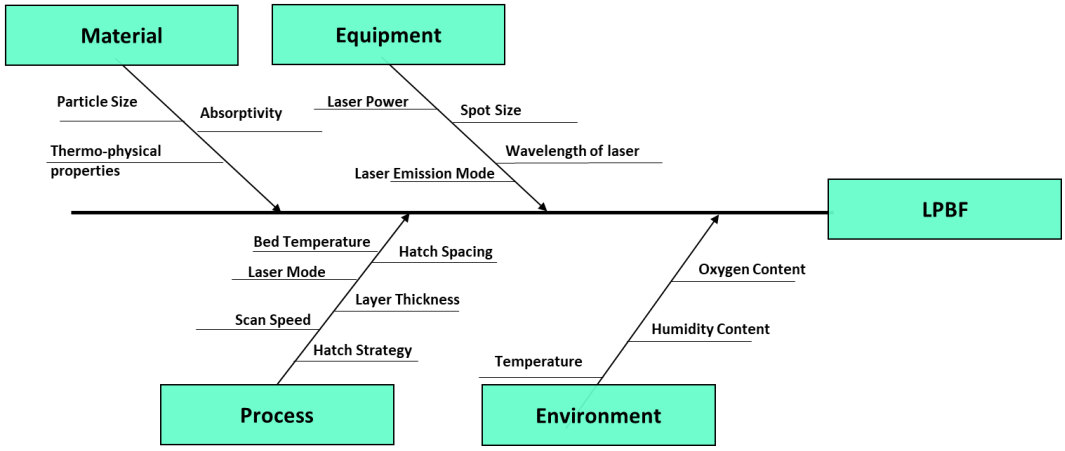


Figure 1.2 Simplified Ishikawa/fishbone for LPBF

The LPBF process can essentially be divided in two parts: melting and solidification [1]. Complete melting of metallic powder is essential for avoiding process related issues like porosity [33]. Such kind of defects are formed when the energy density ($\mathrm{E_v}$) as defined by equation *(1.1)*, which is a function of laser power, scan speed, hatch distance and layer thickness is not optimum [34].

$$\mathrm{E_v} = \frac{\mathrm{P}}{\mathrm{V.d.h}} \tag{1.1}$$

where in $\mathrm{E_v}$ is energy density (J/mm^3), P is laser power (w), V is the scanning speed (mm/s), d is the layer thickness and h is the hatch distance.

While the low energy density leads to a lack of fusion defect, the high energy density often leads to gas induced porosity[35]. Lack of fusion defect is basically porosity caused due to incomplete melting of the metallic powder, such a porosity is characterized by irregular shapes as shown in Figure 1.3 (a). Gas induced porosity on the other hand is due to excessive energy which leads the metallic powder to sometimes vaporised leading to the entrapation of the gas. Such a porosity is often spherical in shape as presented in Figure 1.3 (b)

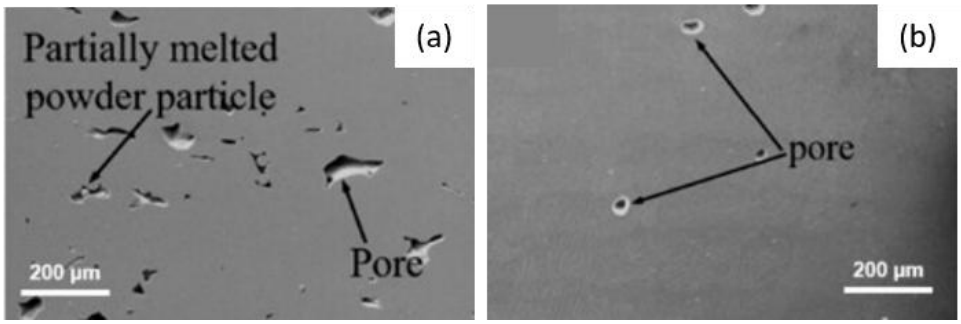


Figure 1.3 SEM images showing two types of porosity observed in LPBF-processed parts. (a) Lack of fusion defect due to insufficient energy input, with irregular pore shapes and unmelted powder particles and, (b) Gas-induced porosity formed under high energy conditions, characterized by spherical pores [36].

Solidification on the other hand does not only decide the microstructural development but could also lead to the induction of thermal stresses. One of the defining characteristics of the Laser Powder Bed Fusion (LPBF) process during solidification is the extremely high cooling rates and steep thermal gradients experienced during fabrication. Due to the localized nature of the laser heat source and the layer-by-layer deposition, LPBF often involves cooling rates in the range of 10^3 to 10^6 K/s [10]. These rapid thermal cycles lead to non-equilibrium solidification conditions, which result in unique microstructural features compared to conventional manufacturing methods. For instance, grains tend to grow epitaxially from the previously solidified layer, often resulting in highly anisotropic columnar microstructures aligned along the build direction[37] . Moreover, the rapid solidification can suppress the formation of equilibrium phases and instead promote the development of fine cellular or dendritic substructures, particularly in alloys such as IN718 [38] and Ti-6Al-4V [39]. The interplay between cooling rates, thermal gradients, and alloy composition governs the transition between columnar and equiaxed grains, often described using the G/R ratio, where G is the thermal gradient and R is the solidification rate [33]. This makes microstructure prediction in LPBF highly complex, yet critically important, as it directly influences the final mechanical properties and performance of the printed part. Moreover, as a result, understanding and modelling microstructure evolution in LPBF has become a key area of research in recent years.

1.3 Solidification

Solidification plays an acute role in microstructure development. Understanding solidification and its effect on the microstructural development remains vital for the present work. In this sub section, the principle of solidification, its component and its effect on grains structure will be presented.

1.3.1 Preliminary Concepts

Solidification is essentially defined as a process by which liquid transforms into solid [40]. Metal solidification is divided into two steps namely: (a) nucleation, which is defined as formation of stable nuclei in the liquid metal and, (b) growth of the nuclei usually into dendrites to finally form the grain structure. The schematic of the solidification in metals is presented in Figure 1.4 .

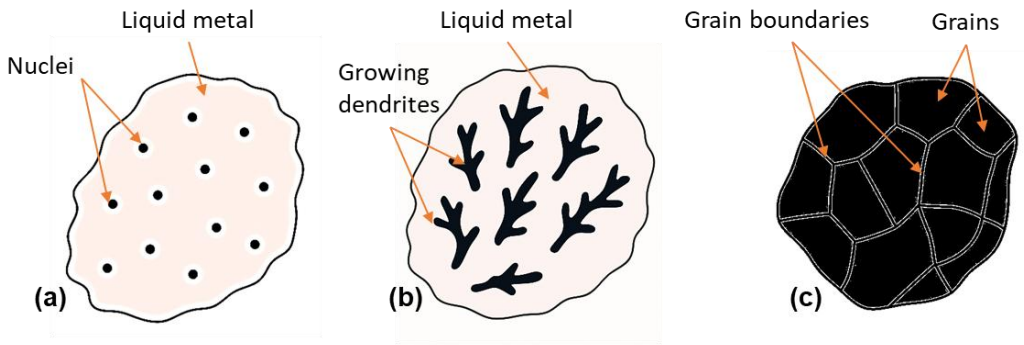


Figure 1.4 Schematic of the solidification of liquid metal: (a) Initial nucleation with dispersed nuclei in the liquid phase, (b) Growth of dendritic structures from the nuclei, representing directional solidification, and (c) Final microstructure with well-defined grains separated by grain boundaries.

Figure 1.4 illustrates the sequential process of solidification in metals: initial nucleation (a), dendritic growth (b), and grain boundary formation (c). This evolution

plays a key role in defining the final grain structure and thus the bulk properties of the material. Moreover, the texture of the component also develop during solidification.

1.3.2 Nucleation

The transformation of a metal from the liquid to the solid state begins with nucleation. Nucleation starts with a formation of stable solid crystals (nuclei) within a liquid. Nuclei are often termed as embryonic crystal which are formed by clustering of atoms which combine during their random motion in the liquid phase. During the process of nucleation, several embryos are formed but most of them dissolve in the liquid. Only those embryos, which are stable and satisfy the thermodynamics criteria become nuclei and grow in due process of solidification. Broadly, there are two types of nucleation mechanism namely: homogenous nucleation and, heterogeneous nucleation.

1.3.2.1 Homogenous nucleation

Homogenous nucleation is defined as clustering of randomly moving atoms within the liquid to form embryonic crystals. This process leads to the disturbance of the free energy of the system (liquid + embryos). According to thermodynamics, nucleation becomes feasible only when the total free energy of the system is minimized with the formation of solid particles. This starts at a temperature known as the thermodynamic melting point T_m, at which the free energies of the solid and liquid phases are equal i.e:

$$G_l = G_s \tag{1.2}$$

$$\Delta G = G_s - G_l = 0 \tag{1.3}$$

Wherein G_l is free energy of liquid phase and G_s is free energy of the solid phase. Below this melting temperature ($T < T_m$), the solid phase becomes thermodynamically more stable, and the difference in free energy becomes negative:

$$\Delta G = \ G_s - G_l < 0 \tag{1.4}$$

Nonetheless, the formation of a solid nucleus involves not only the bulk free energy (which favors the transformation) and is negative but also the transformation leads to creation of a new interface between solid and liquid, which leads to increment of total energy due to surface tension γ. Therefore, the total free energy change ΔG for forming a spherical nucleus of radius r is given by equation (1.5) and is the combination of two energies namely [40,41]:

1. Volume free energy change ($\Delta\ G_v.V$), which is negative and favors growth.

2. Surface energy term ($\gamma.\mathrm{A}$), which is positive and acts as a barrier to nucleation, due to the energy required to form the solid-liquid interface.

$$\Delta G = \frac{4}{3}\pi r^3.\Delta\ G_v + 4\pi r^2\gamma \tag{1.5}$$

Wherein $\Delta\ G_v$ Gibbs free energy change per unit volume, γ is the solid-liquid interfacial energy per unit area, r is the radius of the spherical solid nucleus. As shown in Figure 1.5, the total free energy ΔG initially increases with radius due to the dominance of the surface term, reaches a maximum, and then decreases as the volume term takes over. The point at which ΔG is maximum corresponds to the critical radius r^*. The critical radius given by equation (1.6) is calculated by differentiating equation (1.5) and equating it to zero[41].

$$r^* = \frac{-2\gamma}{\Delta\ G_v} \tag{1.6}$$

At critical radius r^* the free energy of solid phase and liquid phase becomes. Therefore, the radius of the embryos must be greater than r^* to ensure that total free

energy change ΔG becomes negative. The growth of nuclei i.e the growth of solid phase starts only after this point which leads to decreasing free energy [40].

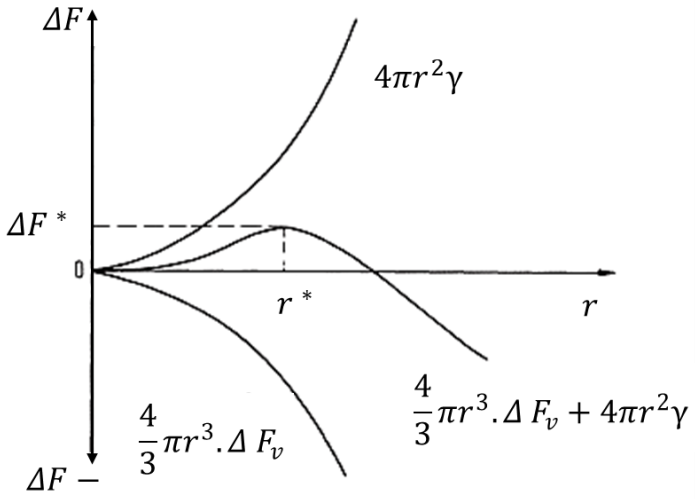


Figure 1.5 Free-energy relationship with radius of growing spherical nuclei during solidification

Nucleation studies have shown that with a reduction of the liquid metal temperature, the driving force for solidification increases and thus, the critical radius r^* decreases. Meaning that, with the reduction of temperature more and more stable embryonic crystals forms and probability of stable nucleation increases [42]. For homogeneous nucleation, a considerable undercooling is required [43]. However, in practical solidification process liquid metal needs not be super-cooled to start the growth of solid phase due to the heterogeneous nucleation [42].

1.3.2.2 Heterogeneous nucleation

The formation of an embryonic crystal on an existing surface is considered as heterogeneous nucleation [42,44]. This type of nucleation commonly occurs at interfaces such as the mold walls during casting, the surfaces of the base materials in welding, pre-solidified layers in metal additive manufacturing, or on impurities and other foreign inclusions or particles formed by the addition of nucleating agents. A heterogeneous solid nucleus on a pre-existing surface is presented in Figure 1.6.

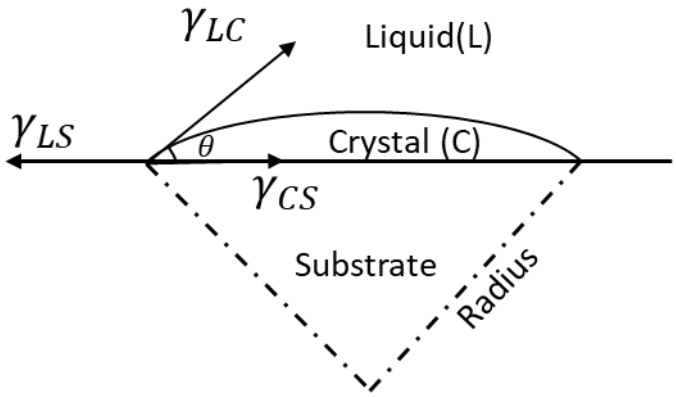


Figure 1.6 Spherical crystal formation on the heterogeneous surface material

In this figure, the terms $\gamma_{LS}, \gamma_{CS}, \gamma_{LC}$ are the surface energies of the liquid–substrate interface, crystal–substrate interface and, liquid–crystal interface respectively. The free energy barrier that must be exceeded for the heterogeneous nucleation is given by equation (1.7) [45].

$$\Delta G = \frac{4\pi\, {\gamma_{LC}}^3 {T_m}^2}{3(\Delta H_m \Delta T)^2}(2 - 3cos\theta + cos^3\theta) \tag{1.7}$$

Wherein ΔH_m is the latent heat of melting, θ is the contact angle and ΔT is the undercooling. Theoretically, if the contact angle θ is zero, the liquid metal completely wet the substrate and the driving force ΔG required for nucleation becomes zero which means that nucleation can occur instantly at the surface without overcoming any barrier free energy. Heterogeneous nucleation is very common in LPBF, electron beam melting, and casting fusion welding [46]. Since heterogeneous nucleation requires less activation energy than homogenous nucleation, this kind of nucleation initiates during the start of solidification process of metal alloys. Heterogeneously nucleated embryos begin to grow once the thermodynamic conditions for growth are satisfied. As the cooling continues and the temperature of the melt decreases further, a critical level of undercooling is eventually reached, enabling the onset of homogeneous nucleation. Once stabilized, these homogeneously formed nuclei also begin to grow. At the same time, additional

nucleation events may occur, forming new stable nuclei that could either belong to the same phase as the initial ones or represent a different phase altogether.

1.3.2.3 Dominant Nucleation Mechanism in LPBF

In LPBF, solidification is dominantly induced by the process of heterogeneous nucleation because the process is driven by the availability of energetically favorable interfaces. These are residual solidified layers, melt-incompletely solidified powder particles, oxides films, and other microstructure defects, which all greatly reduce the nucleation thermodynamic barrier[47].

LPBF typically involves epitaxial and bulk nucleation [23]**.** One of the most influential forms of heterogeneous nucleation in LPBF is epitaxial nucleation. This process, widely described in the literature[48,49] entails the nucleation of new grains at the solid-liquid interface. Solidification-induced defects and thermal and structural continuity across the layers, coupled with conduction-driven cooling and fast thermal cycling, helps the new nucleated grains favorably orient with the parent structure [44]. Epitaxial nucleation tends to produce directionally consistent grain microstructures owing to the strong inheritance of the orientation.

In parallel, bulk nucleation occurs within the melt pool, away from established solid interfaces. It takes place in regions with relatively uniform thermal fields and sufficient undercooling [48,50,51]. Depending on the material system and local solidification conditions, bulk nucleation can be either homogeneous or heterogeneous in nature. However, in practical LPBF environments, heterogeneous bulk nucleation remains more common due to the presence of non-metallic inclusions, oxide particles, or spatters acting as nucleation catalysts [12]. This occurs when sufficient undercooling is achieved in the melt, often in the central regions of the melt pool, away from the previously solidified layers.

1.3.3 Crystal Growth and Interface Stability

Once the nuclei are formed, the subsequent evolution of the solid-liquid (S/L) interface is governed by the dynamics of crystal growth. The morphology of the growing front can be planar, cellular, or dendritic as depicted in Figure 1.7 . The development of morphology is strongly influenced by the interplay between the thermal gradient (G) and solidification velocity (R)**.** Understanding the stability of this interface under the extreme thermal conditions of LPBF is critical, as it dictates grain structure and texture formation. As the stable nuclei grows with attachment of atoms around it, it leads to instabilities also termed as local perturbations. This leads to the formation of the Solid-Liquid interface. When the instabilities do not survive, it leads to formation of the planar interface as depicted in Figure 1.7 (a). During solidification of pure metal, there is only one source of the instability which is the thermal field or thermal undercooling and therefore S/L interface during solidification of pure metal is generally planar in the absence of excessive undercooling. However, in conditions where the perturbations become stable they grow, it leads to morphological instabilities and transitions to cellular or dendritic structures. (Figure 1.7 (b)- (d)) [52].

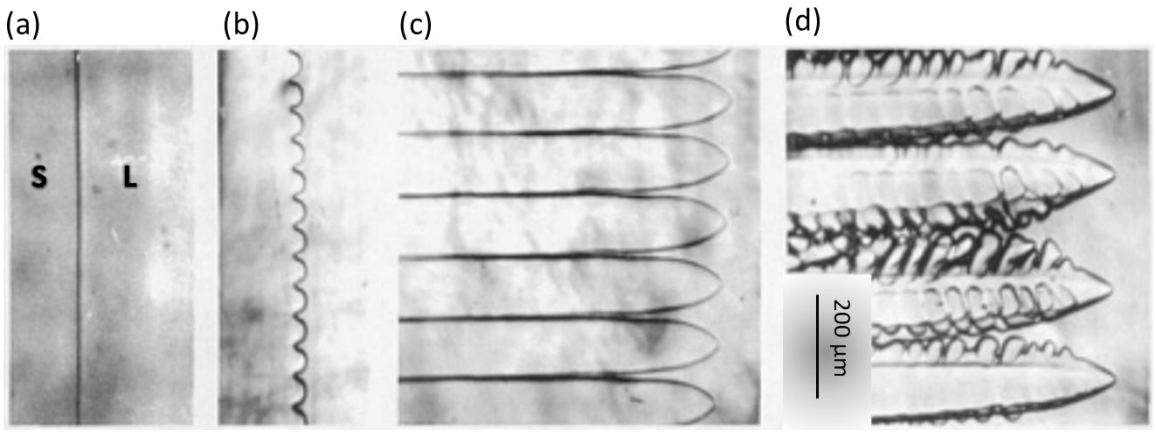


Figure 1.7 Different morphology of the solid/liquid interface: (a) planar interface,(b)cellular interface,(c)columnar interface and, (d) dendritic interface [52]

The relationship between the thermal gradient and the solidification front velocity plays a pivotal role in determining the stability and morphology of the solid–liquid (S/L) interface. The combination of these two parameters (G and R) governs whether the interface will remain planar or undergo a transition to cellular or dendritic growth. Their morphological stability diagram is shown in Figure 1.8 [53]. The transitions presented in Figure 1.8 is based on experimental and theoretical analysis of directional solidification[53]. When the G/R ratio is high, the planar front is thermodynamically stable due to effective heat removal. As G/R decreases, instabilities develop, first forming cells, and then more complex dendritic structures as the system enters a constitutionally undercooled regime. This diagram is particularly relevant in processes like Laser Powder Bed Fusion (LPBF), wherein thermal gradients and interface velocities vary rapidly and spatially.

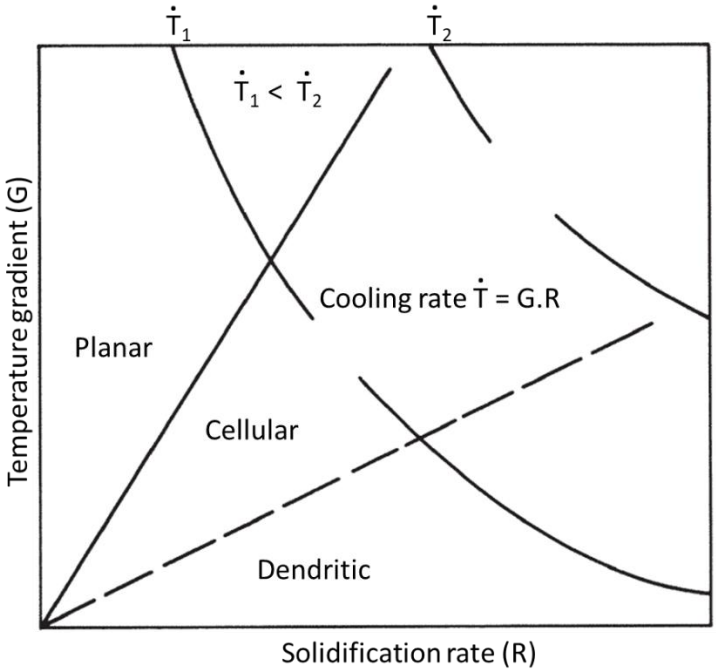


Figure 1.8 Effect of cooling rate and temperature gradient on the morphology [53]

The discussed microscopic interface morphologies ultimately lead to different kinds of grain structures within the solidified metal. In Figure 1.9 it is shown that

variations in solidification conditions lead to distinct macroscopic grain morphologies: (a) strong columnar grains typical of pure metals with high G/R; (b) mixed columnar and equiaxed zones in alloys; and (c) fully equiaxed grain structure obtained by heterogeneous nucleation in the melt and very high cooling rate [52]

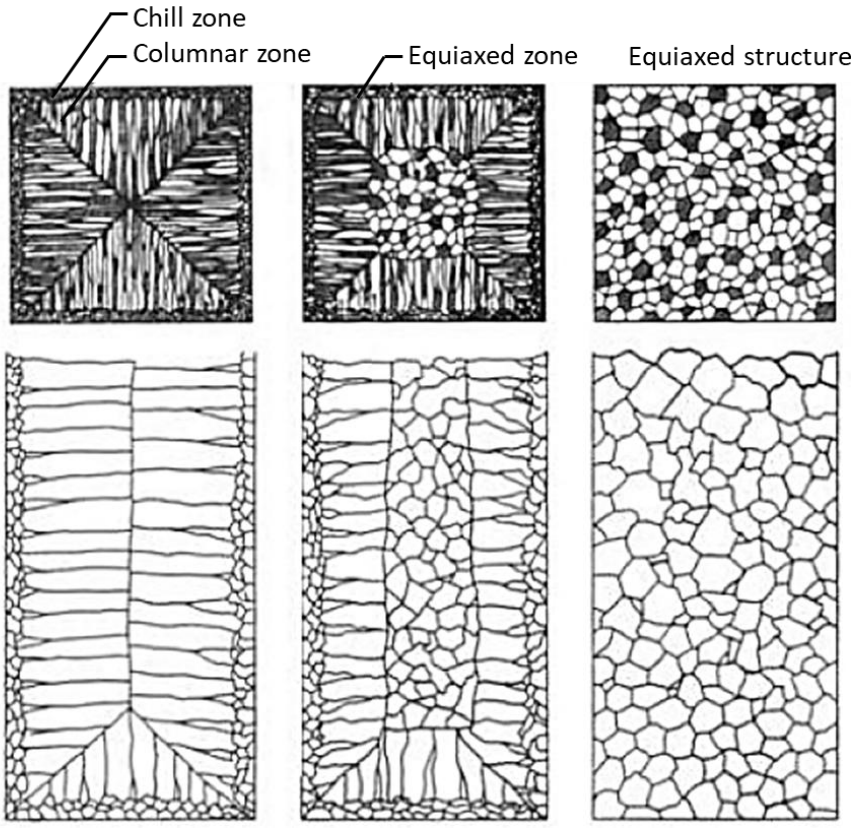


Figure 1.9 Schematic illustrations of typical grain structures formed during directional solidification in casting. (a) Pure metals showing a chill and columnar zone; (b) solid-solution alloys with a central equiaxed zone; (c) structure with full equiaxed grains [54]

1.3.4 Grain Structure Evolution in LPBF

Grain morphology development during LPBF is a direct consequence of the highly dynamic thermal environment and the accompanying solidification mechanisms. The interplay of nucleation behavior, interface stability, and thermal gradients governs the

size, shape, and crystallographic orientation of the grains. Though morphology often depends on the selected process parameters, in the experiments it has been observed that equiaxed grains form at the center of the melt pool (commonly termed as CET zone) while the columnar grain develops across the build direction.

1.3.4.1 Epitaxial Growth and Columnar Grains

One of the most distinctive qualities of LPBF is its layer-by-layer solidification in which the melt pool comes into frequent contact with its previously solidified counterpart. This arrangement supports epitaxial nucleation, where new grains tend to take on the crystallographic orientation of the substrate below because of reduced undercooling at the solid-liquid interface. As a result, grains tend to grow along the direction of the maximum thermal gradient, often vertically aligned with the build direction forming long, columnar grains that span multiple layers [55].

1.3.4.2 Columnar-to-Equiaxed Transition (CET)

Despite the prevalence of columnar grains, under certain processing conditions, LPBF can also lead to equiaxed grain formation. This occurs because of constitutional undercooling in the melt pool center or when grain refiners or oxide particles provide sites for heterogeneous nucleation away from the build substrate [23]. The columnar-to-equiaxed transition (CET) is governed by the relative values of the thermal gradient (G) and the solidification rate (R). When the G/R ratio is low, the interface becomes unstable, promoting nucleation ahead of the interface, which favors equiaxed grains [53]. Additionally, turbulent flow or Marangoni convection within the melt pool can enhance nucleation at multiple points in the bulk, reinforcing the equiaxed mode. Equiaxed grains typically take random orientations because they are often subject to uniform thermal gradient.

1.3.5 Texture Development and Mechanism

The properties of a crystalline material are inextricably related to its microstructure, including characteristics of grain shape and size, second-phase distributions, dislocation structures, and interfacial properties. However, a full description of microstructure must also take into consideration the crystallographic orientation of the grains.

In a polycrystalline material, each grain is considered as a single crystal wherein the atoms are arranged in a specific repeating lattice structure. The crystallographic orientation of such a grain is referred to the spatial arrangement or alignment of this lattice relative to a fixed reference frame, such as the rolling direction in sheet metals or the build direction in additive manufacturing. These orientations are commonly described using Miller indices to denote lattice directions and planes [56]. The orientation of each grain can also be represented using Euler angles (generally denoted as (Φ_1, Φ, Φ_2), which define the rotation required to align the crystal coordinate system with the sample coordinate system. Texture is nothing but a statistical concept and when a significant number of grains share similar orientations, the material is said to have a crystallographic texture. Texture generally results in anisotropy of physical and mechanical properties. As opposed to a visual grain orientation or phase distributions in observations from optical or electron micrographs, texture addresses preferred crystallographic orientations specifically, and its statistical nature dictates that a material can be regarded as strongly textured if 30–40% of the grains have similar orientations [57]. The crystallographic texture development in polycrystalline materials is governed by a combination of thermodynamic and kinetic factors during various stages of a material's processing. The primary texture mechanisms responsible for texture formation are: (a) solidification**,** (b) plastic deformation**,** and (c) recrystallization. Different mechanisms contribute to the alignment of grains in specific crystallographic

orientations. The nature and extent of texture depend on the dominant mechanism, material system, and processing path [56,57].

1.3.5.1 Solidification Texture

Solidification texture mechanism is observed in the processes where the complete melting and solidification of metal is involved, like in casting, additive manufacturing and welding. Texture formed during solidification is primarily a result of directional growth influenced by thermal gradients and anisotropy in interface kinetics. In metallic systems, grains grow such that their preferred crystallographic direction align with the heat-flow direction. The preferred crystallographic direction depends on the lattice structure of the metal in discussion. In Table 1.1, preferred growth direction of different lattice structure is reported [35].

Table 1.1 Preferred growth direction of the lattices structure [53]

Lattice Structure	Preferred Growth direction
Face-centred cubic	<100>
Body-centred cubic	<100>
Body-centred tetragonal	<110>
Hexagonal close-packed	<1010>,<0001>

1.3.5.2 Deformation Texture

Deformation texture develops during different deformation processes like forging, rolling, compaction, and extrusion. During plastic deformation, grains rotate in response to the applied stress, leading to the development of deformation textures.

These are modified by the material's crystal structure and the active slip systems. In FCC materials subjected to rolling, for instance, the typical texture components include the Copper {112}⟨111⟩, Brass {011}⟨211⟩, and S {123}⟨634⟩ orientations. In body-centered cubic (BCC) materials, the α- and γ-fiber textures are commonly observed. The development of such textures is not random but often governed by the symmetry and geometry of deformation, such as uniaxial tension, compression, rolling, or extrusion. These orientation changes is represented in Figure 1.10**,** which shows typical grain alignments in a drawn wire and rolled sheet, underlining the correlation between processing directions and crystallographic orientations [56].

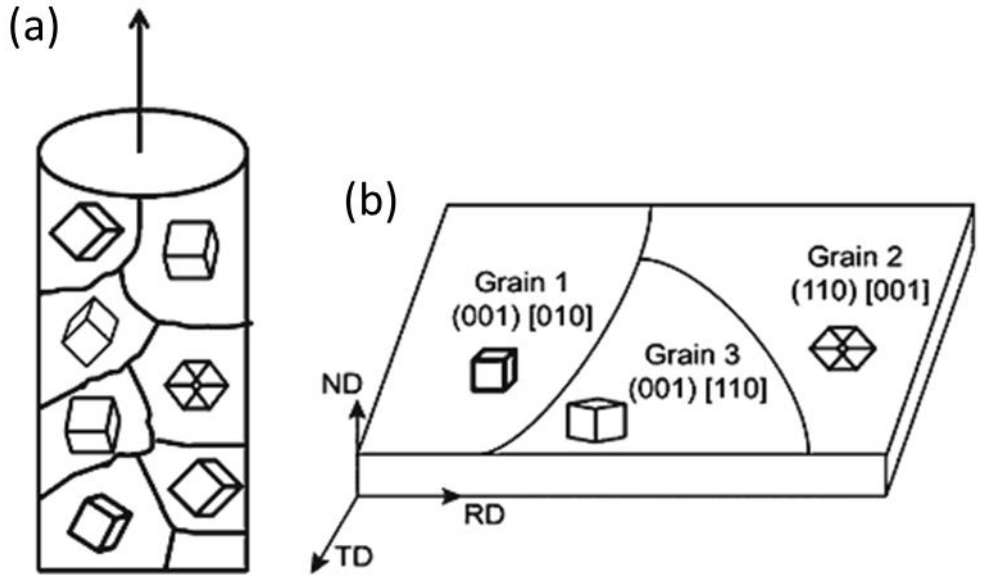


Figure 1.10 A drawn wire with preferential ⟨110⟩ direction parallel to drawn axis (b) A rolled sheet showing three grains with different orientations: Grain 1 with (001) [010], grain 2 with (110) [001], and grain 3 with (001) [110] [56]

1.3.5.3 Recrystallization Texture

Recrystallization texture is generally developed in the heat treatment processes like annealing when a heavily plastically deformed metal is subjected to prolonged annealed at a sufficiently high temperature. This leads to the nucleation and growth of

new strain-free grains. These recrystallized grains often inherit a preferential orientation related to the stored energy distribution and the orientation of deformed subgrains. The recrystallization texture can differ significantly from the preceding deformation texture. In some cases, such as cube texture in high-purity aluminum, recrystallization can produce a very sharp and strong texture that dominates the material's properties [56] .

1.3.5.4 Texture Development Mechanism in LPBF

LPBF is subjected to complete melting and solidification, therefore, texture development during LPBF is primarily governed by the solidification texture mechanism. In LPBF, texture development is predominantly governed by the highly directional nature of solidification and rapid thermal cycling. Due to the steep thermal gradients along the build direction, grains tend to grow along the build direction with their preferred growth directions aligned towards the heat flow. For example, in FCC and BCC alloys, the commonly observed texture is ⟨001⟩. Nevertheless, depending on the local melt pool dynamics, build orientation, and scanning strategies, additional texture variants may emerge, though the directional solidification process often dominates [55,58].

1.4 Microstructure Modelling Techniques

Understanding and predicting the evolution of microstructure and texture in polycrystalline materials is critical in materials science. The mechanical and physical properties of metals are controlled by their microstructure. Therefore, the study of microstructure development during processing remains a priority in materials science. This becomes even more critical in the case of AM, particularly the LPBF technique.

Components produced with LPBF often exhibit distinctive microstructures compared to those produced using conventional manufacturing methods, which ultimately leads to distinctive mechanical properties. Moreover, unlike conventional processes, LPBF offers the unique advantage of local tailoring of microstructure, making

it a powerful method for producing components with customized property profiles. As a result, various experimental studies on microstructure development during LPBF have been conducted [39,59,60]. However, understanding the underlying mechanisms governing microstructure evolution in LPBF is not straightforward. LPBF is associated with complex phenomena like rapid solidification, steep thermal gradients, and, residual stress formation. These factors, combined with a wide range of process parameters such as laser power, scan speed, hatch spacing, and layer thickness (as discussed in Section 1.2), make experimental investigation both costly and time-consuming.

To address this, computational techniques have been developed to study microstructure evolution in LPBF. Different modelling techniques have been developed and used in recent years to simulate the microstructure. These models are based on fundamental principles of thermodynamics, kinetics, crystallography, and transport phenomena to capture processes such as grain nucleation, competitive growth, orientation selection, recrystallization, and texture formation. Based on the objectives and computational requirements, different approaches such as the Phase-Field (PF), Cellular Automaton (CA), Kinetic Monte Carlo (KMC) have been employed. In this section, the commonly used modelling techniques for simulating microstructure evolution during LPBF will be discussed briefly, highlighting their working principles, applications, and limitations.

1.4.1 Phase-Field Modelling

The Phase-Field Method (PFM) is a powerful and versatile mesoscale computational technique to model and simulate the morphology and microstructural evolution in materials. It provides a continuous field description of microstructural features such as interfaces, grains, and phases without the need for explicit interface tracking. PFM consists of a smoothly varying function, commonly called a phase field, which describes the interface between the two variable phases. The temporal evolution

of the phase, i.e. the microstructure in PFM, is strongly based on thermodynamic and kinetic principles and is highly suited for capturing fine-scale morphological evolution during solidification[12].

In PFM, the microstructure evolution model is described using one or more non-conserved scalar field (φ) and conserved (c) order parameters. During microstructure evolution in solidification, there exists interfaces (solid/liquid). Therefore, for solidification, in PFM a single-phase field φ (ranging from 0 in liquid to 1 in solid) is frequently coupled with a concentration field c to relate the interfacial energy to the gradient energy terms. Mathematically, the behavior of the model is given by a total free energy function as [61]:

$$F = \int_v \left[\mathrm{f}(\varphi, \mathrm{c}, \mathrm{T}) + \frac{\epsilon^2}{2} |\nabla\varphi|^2 \right] \ \mathrm{dV} \tag{1.8}$$

Wherein $\boldsymbol{F}$ is the energy function, $\mathrm{f}(\varphi, \mathrm{c}, \mathrm{T})$ is the bulk energy density, c is the concentration field, V is volume, T is the temperature field, the product of parameter ϵ^2 $|\nabla\varphi|^2$represents the gradient energy density, which contributes to the interfacial energy. During the process (for e.g., solidification), the free energy function reduces monotonously. The time evolution description of the equations of motion of the system is calculated by solving a set of equations[12].

The first equation is the Allen-Cahn equation (given by equation (1.9)), which is solved for a non-conserved variable φ. It governs how fast the field φ evolves based on a thermodynamic driving force, which in the case of solidification is typically undercooling.

$$\frac{\partial\varphi}{\partial t} = -M_\varphi \frac{\delta F}{\delta\varphi} \tag{1.9}$$

wherein M_{φ} is the mobility of the phase boundary and is often dependent on the temperature [62]. The second equation which controls the evolution of solute field/ concentration field c is given by Cahn-Hilliard equation (equation (1.10)). This equation describes the separation of the phases (solid/liquid in case of solidification)

$$\frac{\partial c}{\partial t} = -M_{\mathrm{c}} \frac{\delta F}{\delta \mathrm{c}} \tag{1.10}$$

wherein, M_{c} is the mobility coefficient for the concentration field which is a parameter that controls how fast solute redistributes in the system during phase separation or solidification.

The PF method often needs to be coupled with temperature model to describe the evolution of phase and the concentration [61]. Often, a thermal field, which is generated parallel to PF, is directly coupled with PFM. The PF method requires many model parameters as input factors such as temperature dependent mobility and kinetic coefficients [21]. The spatial resolution of the PF models are generally of the order of nanometers. This allows the model to capture dendritic structures and concentration fields. Such a high resolution and high computational load during PF, however, limits the simulation domain to the order of micrometer. Nevertheless, efforts have been made to use PF on a grain scale, which significantly reduces the computational load. A typical PF simulation employed to capture both dendritic-scale solute redistribution during rapid solidification and grain-scale microstructural evolution is presented in Figure 1.11.

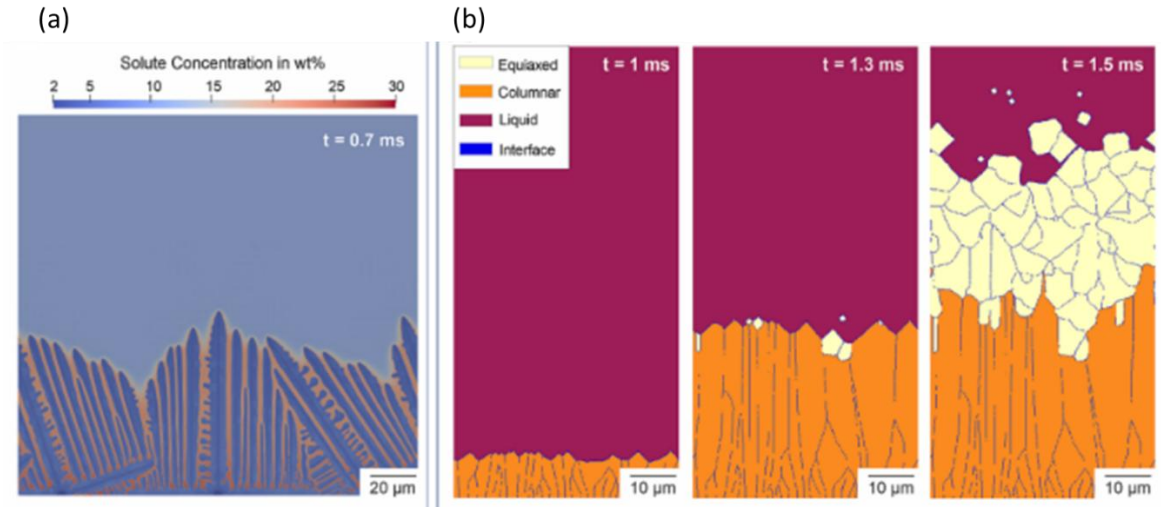


Figure 1.11 (a) Simulated solute concentration field during rapid solidification of Ti-6Al-4V at the dendritic scale, resolved at 30 nm, under a high cooling rate of 50,000 K/s;(b) Phase-field simulation at the grain scale for electron beam powder bed fusion (E-PBF) of Ti-6Al-4V, with spatial resolution of 100 nm, using a beam power of 420 W and scan speed of 0.8 m/s [12]

Various researchers have employed the PF method to model microstructure evolution in LPBF. Yang et al.[63] developed a fully three-dimensional PF model coupled with thermal-fluid dynamics to simulate nucleation, epitaxial grain growth, remelting, and coarsening over a multilayer LPBF process. Their simulation domain was limited to an RVE of approximately 150 × 150 × 150 µm³ due to computational constraints. Ma et al. [64] integrated PF modeling with machine learning to predict microstructure evolution in Inconel 718. The authors were able to achieve high predictive accuracy while reducing computation time. Their simulations used RVE sizes on the order of 100 µm³, reflecting typical trade-offs in scale and fidelity. Chen et al. [65] employed a multiphase PF model linked to CALPHAD thermodynamics to study the dissolution of Laves phases during post-processing. Radhakrishnan et al.[66] investigated dendritic solidification and segregation in a Ni–Fe–Nb alloy using PF methods in 2D domains spanning.

While the aforementioned studies illustrate that the PF method is able to capture intricate microstructural features, they also highlight a common limitation of restricted domain sizes. This is due to the fine spatial resolution, which leads to a high

computational load. Consequently, although PF models offer excellent physical detail, their scalability is reduced, making them less practical for part-scale LPBF builds or large design-of-experiments studies without access to high-performance computing resources. Furthermore, the PF simulations often require careful calibration of interface mobility, free energy formulations, and anisotropy parameters, many of which are not readily available for new alloys. This lack of accurate material constants, particularly temperature-dependent thermophysical and kinetic data, presents a significant barrier to applying PF models to novel materials systems without extensive experimental support.

1.4.2 Kinetic Monte Carlo

The Kinetic Monte Carlo (KMC) algorithm is a probabilistic, lattice-driven stochastic simulation methodology that is employed to simulate the time evolution of the microstructure following probabilistic atomic or mesoscale events. In contrast to continuum methods like the PFM, the KMC algorithm simulates microstructure evolution through randomly chosen and enacted events, such as atomic diffusion, driven by principles of local minimization of energy. It is particularly well suited for simulating processes that involve grain growth, pore elimination, recrystallization, and sintering, which are driven by curvatures and gradients in energy.

In KMC, the system is discretized into lattice sites, and each site is attributed to have a state variable, often a phase label or a grain ID. The schematic of a particular KMC approach used to model the evolution of grain structure during solidification is presented in Figure 1.12. Due to surface energy effects, the structures/cells during solidification start to coarsen. Moreover, coarsening is possible within the heat affected zone (HAZ). When the temperature falls down to a certain level where no transformation is possible, the grain structure becomes stable.

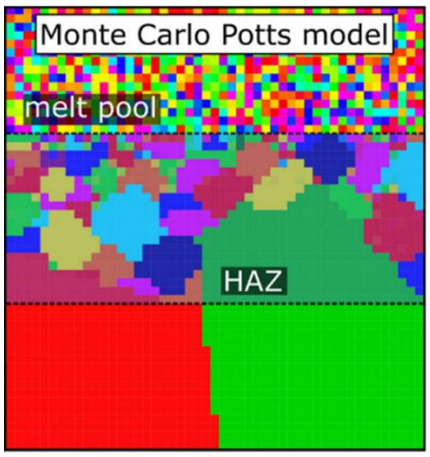


Figure 1.12 Schematic of a KMC modelling technique

Events are chosen based on their occurrence rate, which is often characterized by an Arrhenius-type relation such as:

$$\Gamma_{\mathrm{i}} = -v_{\mathrm{i}} \exp\left(\frac{E_{\mathrm{i}}}{k_{\mathrm{B}} T}\right) \tag{1.11}$$

wherein Γ_{i} is the transition rate for event i, v_{i} is the attempt rate, E_{i} is the activation energy, k_{B} is Boltzmann's constant, and T is the temperature. The simulation time advances by selecting the most probable event and updating the system state accordingly. The time increment is governed by:

$$\Delta \mathrm{t} = -M_{\mathrm{c}} \frac{ln(R)}{\Gamma_{\mathrm{total}}} \tag{1.12}$$

wherein R is a uniformly distributed random number in (0,1), and Γ_{total} is the sum of all possible event rates. Such an approach enables time evolution of the system without resorting to time-dependent partial differential equations.

One standard model formulation employed by KMC is the Potts model, whose overall system energy is expressed by:

$$\mathrm{E} = \frac{1}{2}\sum_{i}\sum_{j} J_{ij}\left(1 - \delta(q_i, q_j)\right) \tag{1.13}$$

q_i and q_j represent neighboring sites' states (e.g., grain IDs), J_{ij} is the grain boundary energy between them, and δ is the Kronecker delta function. The evolution is carried out by randomly choosing lattice sites and checking if changing their state decreases the total energy of the system, using the Metropolis acceptance rule.

$$\mathrm{P} = \begin{cases} 1, & \Delta\mathrm{E} \leq 0 \\ \exp\left(-\dfrac{\Delta\mathrm{E}}{k_{\mathrm{B}}T}\right), & \Delta\mathrm{E} > 0 \end{cases} \tag{1.14}$$

wherein, $\Delta\mathrm{E}$ is the change in energy from the proposed update, T is a simulation temperature. This approach enables curvature-driven grain boundary migration and allows modeling of microstructure evolution over extended time scales. The KMC technique is computationally efficient and can simulate large domains (to millimeter size) over long time durations. It does not, however, have the capability to rigorously simulate interface curvature, anisotropic growth, or solute redistribution since it is not physically coupled to thermal or chemical fields except when other models are coupled into it.

Researchers have used the KMC model to simulate microstructure evolution in AM, especially the post-solidification phase of LPBF. Rodgers et al. [15] used a 2D KMC Potts model to simulate LPBF microstructure grain coarsening. They modeled the grains as lattice sites, which evolved using rules based on energy minimization. Even though the model was able to simulate large domains effectively, it did not consider crystallographic orientation evolution, which restricts its accuracy for texture prediction.

Zhang et al.[14] created a 3D KMC model based on experimentally reconstructed microstructures of stainless steel. Their simulation space was a cube of side length equal to 120 µm, which was divided into $1\ X\ E^6$ voxels. Sintering behavior, grain coarsening,

and pore evolution were successfully modeled at various temperatures by the model. Outcomes illustrated densification-driven behavior below lower relative densities, which changed to grain growth-dominated evolution for above 70% density.

Körner et al. [45] presented an exhaustive review of AM microstructure modeling methodologies and placed KMC as an effective simulation methodology for statistically driven processes such as sintering and coarsening. They noted, though, that KMC does not have the capacity to simulate solidification-related events such as dendritic growth, nucleation by epitaxy, and solute redistribution, which are pivotal in LPBF. Coupling KMC with thermal histories and crystallographic information is still a daunting challenge.

Even though the KMC technique facilitates rapid simulation of extensive domains and extensive time scales, it is beset with significant limitations. These are the absence of thermodynamic coupling and the absence of crystallographic orientation tracking. As such, though KMC methodology is worth using to model statistical grain growth and post-solidification phenomena, it is not effective in predictive terms for indicating primary microstructural features developed in LPBF solidification.

1.4.3 The Cellular Automaton Method

The Cellular Automaton (CA) method is a lattice-based, mesoscale computational modeling technique which is widely used to simulate the microstructural evolution during recrystallization [67–70], casting [71,72], welding [73,74] and additive manufacturing [20,75]. This technique was first developed by von Neumann, in which the simulation domain is divided into a regular grid of cells where each of the cells represents a small volume of the material [76]. In a typical microstructure simulation using CA method, the computational domain is discretized into a 3D lattice of cells, each storing a set of variables. These variables generally include the phase state (S), temperature (T), grain orientation (O), and grain index (I). A schematic of CA method simulation is depicted in Figure 1.13. Wherein the color represents grain identity. Cells

belonging to the same grain share the same index and orientation, represented visually by the same color in the domain. This type of data structure enables the simulation of grain competition, epitaxial growth, and texture evolution in LPBF. The evolution from one state to another of the cells is given by physical rules simulating nucleation and grain growth phenomena[77].

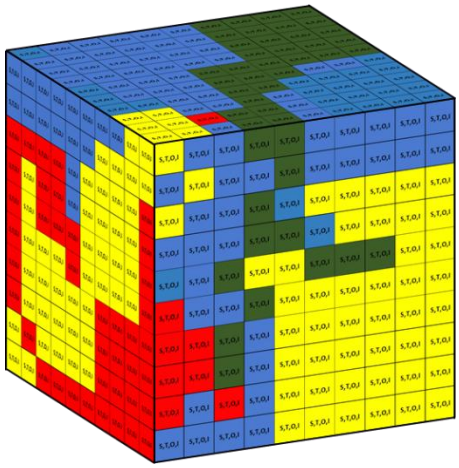


Figure 1.13 Schematic of the Cellular Automaton (CA) modeling framework for LPBF microstructure simulation. Each cell in the 3D lattice stores four key parameters: state (S), temperature (T), orientation (O), and grain index (I).

The CA method is widely used by researchers to simulate the microstructure because of its versatility and capability to consider the crystallographic orientation of the grains. Unlike the PF model which completely relies on solidification thermodynamics and the KMC model which is entirely stochastic, the CA technique uses a stochastic sub model for nucleation [12] and a physics based sub model for the crystal growth [12]. The CA model for microstructure evolution was first introduced by Gandhin and Rappaz, who were the first to introduce the CA technique for microstructure modelling [78] in solidification. At first they proposed a CA framework for a 2-dimensional microstructure evolution during casting considering a uniform temperature field which they later extended to a 3-dimensional domain by coupling CA model with finite element simulations to capture realistic temperature distribution [79,80]. Gandhin

et al. employed phenomenological approach to model the nucleation and physics based model to capture the growth of the crystal [77]. Under this method, the nucleation density is defined as a Gaussian function, which is the function of undercooling ($\Delta \mathrm{T}$) and is given by equation (1.15):

$$\mathrm{N}(\Delta \mathrm{T}) = \frac{N_{\mathrm{o}}}{\Delta T_{\sigma}\sqrt{2\pi}} \int_{0}^{\Delta \mathrm{T}} e^{\left(\frac{\Delta \mathrm{T} - \Delta T_{\mathrm{c}}}{\Delta T_{\sigma}\sqrt{2\pi}}\right)} d(\Delta \mathrm{T}) \tag{1.15}$$

The parameters N_{o}, ΔT_{c}, and $\Delta \mathrm{T}$ are related to how nuclei form during solidification, and they need to be determined through experiments. N_{o} represents the maximum possible number of nuclei that can form in a given volume, essentially the upper limit of how many grains can appear. ΔT_{c}, is the critical undercooling needed for nucleation to start and $\Delta \mathrm{T}_{\sigma}$ is the standard deviation In other words, the material must cool below this threshold before any new grains can form. $\Delta \mathrm{T}$ defines the range of temperatures over which nucleation happens. So, instead of all nuclei forming at a single temperature, they form gradually as the temperature drops within this interval. At the time of nucleation, each nucleus is given a set of Euler angles based on the process and the thermal field. This allows the CA model to also simulate the texture of the specimen being simulated.

Upon the formation of nuclei, the growth model controls the expansion of such grains into neighboring liquid cells. The growth model is generally deterministic and is controlled by the local thermal gradient and crystallographic orientation. The growth rate is typically anisotropic and can be expressed through the concept of a preferred direction of solidification, possibly along the thermal gradient. Grain growth proceeds until they impinge on adjacent grains, or until local equilibrium is achieved. Gandin and Rappaz [78] in their original model, applied Kurz, Giovanola and Trivedi work for determining the growth of the crystal [81] and established a polynomial function of undercooling to predict the crystal growth as given in equation (1.16) .

$$\mathrm{v}(\Delta \mathrm{T}) = a_2(\Delta T)^2 + a_3(\Delta T)^3 \quad (1.16)$$

wherein a_2 and a_3 are parameters to be defined for the material used.

In microstructure modelling, the CA method is often coupled with finite element (FE) simulations of the thermal field. Such a combined modelling technique is commonly referred to as a Cellular Automaton–Finite Element (CAFE) model. Herein, the temperature field of the RVE is predetermined using FE method and then coupled with CA model.

One of the most significant advantages of the CA method is its ability to simulate large domains with relatively low computational cost compared to phase-field models. Moreover, the CA method allows predicting the texture of specimen. It therefore provides a good balance between physical accuracy and simulation speed, making it suitable for 2D and 3D simulations of polycrystalline solidification. The CA method is particularly strong at capturing morphological features like columnar and equiaxed grains, epitaxial growth, and grain competition phenomena and texture typical in metal additive manufacturing.

CA techniques have been employed by a number of researchers to simulate microstructure evolution in LPBF. Koepf et al.[19] applied a 3D CA model to simulate the grain structure in electron beam powder bed fusion (EB-PBF) of Inconel 718. Their model successfully reproduced the characteristic columnar grains observed in experiments. Zinoviev et al. utilized a 2D CA model to simulate morphology and grain size for 316 steel [82]. These studies highlight the CA method's ability to capture critical aspects of microstructural development under additive manufacturing conditions.

However, the CA method also presents several limitations. The resolution of CA models is dependent on the size of individual cells. Especially for LPBF applications, where microstructures such as dendrite arm spacing can be on the order of micrometers or even sub-micrometers, this requires a very fine grid and leads to increased

computational cost. Additionally, LPBF is subjected to melting and remelting of layers, because of which the CA cells undergo multiple solidification cycles, which adds to the computational burden. While parallelization strategies have been used to reduce computation time, existing CA models still do not handle the repeated melting and solidification cycles that happen in LPBF. This remelting behavior introduces redundancy and increases computational cost. Because of this, applying CA models to simulate the microstructure of full sized parts remains a difficult task.

1.5 Conclusion

In this chapter, a the three primary mesoscale approaches feasible for modeling microstructure evolution during LPBF have been broadly explored along with the main concepts of LPBF including nucleation and solidification. The modelling approaches explained are namely: (1) Phase-Field (PF), (2) Kinetic Monte Carlo (KMC), and (3) Cellular Automaton (CA). Each of the techniques has its own specific strengths and limitations. The PF method offers high physical accuracy and captures fine-scale morphology, but it is limited by computational expense and parameter sensitivity, making it unsuitable for part-scale or large domain LPBF simulations. KMC, on the other hand, being a stochastic method, provides efficient simulations over large domains and time scales but is not capable of capturing the texture evolution, which is central to LPBF microstructure. In contrast, the CA method, strikes a balance between the required details of microstructure and the computational load. It is capable of simulating grain morphology, epitaxial growth, and texture evolution at realistic scales with significantly lower computational cost compared to PF, while also offering texture predictability which is not possible in KMC. Although its application to LPBF is challenged by remelting cycles and resolution constraints, these very limitations form the motivation of this work. The comparative assessment of these models is summarized in Table 1.2. These observations reinforce the rationale behind selecting CA as the modeling foundation for

this thesis, particularly aimed at overcoming current limitations in remelting representation and computational efficiency.

Table 1.2 A Comparative Overview of Microstructure Modeling Techniques in LPBF

Method	Pros	Cons	References
Phase Field (PF)	• Captures fine-scale morphological details like dendritic growth and solute segregation • Based on solid thermodynamic and kinetic principles • Suitable for modelling solidification dynamics	• High computational cost; limited to small domains • Requires many material specific parameters • Challenging scalability for large parts	[61,62,83]
Kinetic Monte Carlo (KMC)	• Efficient for simulating large domains and long time scales • Suitable for grain coarsening and post-solidification phenomena • Statistically driven, less parameter-heavy	• Lacks coupling with thermal and chemical fields • Cannot simulate texture evolution • Limited predictive accuracy for LPBF primary features	[14,15,84]
Cellular Automaton (CA)	• Captures grain morphology and texture evolution effectively • Computationally more efficient than PF • Flexible to couple with thermal simulations (CAFE) • Can simulate epitaxial growth, grain competition	• Grid resolution affects accuracy • Computational burden increases with remelting and cyclic solidification • Needs a techniques/algorithm to address the computational loads arising from the remelting phenomenon in LPBF	[16,17,90,22,25,80,85–89]

Chapter 2

Development of a Remelting-Aware 3D Cellular Automaton (RA-CA) Model

2.1 Introduction

The Cellular Automaton (CA) modelling approach is an effective and versatile computational framework suitable for simulating microstructural evolution processes typical of additive manufacturing (AM). Fundamentally, a CA model is a mathematical model, governed by a defined set of deterministic and/or probabilistic transition rules, enabling it to represent the spatial and temporal evolution of physical systems accurately. A CA model for solidification, which is the dominant physical phenomenon in additive manufacturing, is basically constituted by the nucleation and crystal growth mechanisms under consideration of the crystallographic orientations of the crystals, that is the crystallographic texture, and the acting thermal field. These constituents significantly influence the microstructure evolution and must be effectively accounted for by appropriate sub-models and computational strategies for accurate predictions. In this section, the developed CA model is discussed in detail, clearly explaining its underlying mechanisms, computational algorithms, and the interactions between its essential components.

2.2 The CA model

A comprehensive Cellular Automata model coupled with a Finite Element Method (FEM) heat transfer simulation has been developed in the present thesis with the objective to predict accurately microstructure evolution during Laser Powder Bed Fusion (LPBF). The developed framework aims at capturing, efficiently and accurately, the critical dynamics associated with the rapid solidification and cooling processes characteristic of LPBF, thus enabling precise predictions of resulting microstructural features along with the texture development.

The CA model incorporates conceptual framework similar to the one introduced by Gandin et al. [79] in the context of solidification during casting processes. In this 3D CA modelling, the representative volume element (RVE) is partitioned into discrete volumetric cells. These cells essentially represent the smallest volumes resolved within the model. Each cell in the CA grid holds critical state information that governs how it evolves over time. A representation of such a discretization adapted for the simulation of microstructure in LPBF is presented in Figure 2.1. For the current CA model under AM conditions, three state variables are defined as:

Phase: The phase indicates whether a cell is in a solid, liquid, powder, or gas state. In the classical solidification models, phases can be either solid or liquid. However, including a powder state is vital in LPBF simulations to represent the unmolten powder. Additionally, certain regions may be subject to vaporization or keyhole formation, therefore in the present model phase can be either solid, liquid, powder or gas.

Temperature: The temperature profile obtained from a finite element method (FEM) heat transfer model is interpolated for each CA cell at discrete time steps. CA cell resolution is generally finer than the FEM simulation therefore, generally temperature for each cell is interpolated from the temporal profile of FEM simulation. The

temperature history of each cell is crucial in determining phase transitions (solidification, melting, or remelting), as well as in defining growth kinetics.

Grain Index (or Unique Identification Number): Each solid cell belongs to a specific grain, which holds information about the grain's crystallographic orientation. The index allows the model to track grain boundaries and orientation relationships in three-dimensional space during simulation. Tracking orientation is essential for capturing phenomena of competitive grain growth, texture formation, and the anisotropy of mechanical properties.

The CA cells change its state based on predefined rules. The rules governing transitions between states are defined in Table 2.1. These rules depend primarily on local temperature conditions of the cells. Powder-state cells transit into liquid when local temperatures exceed melting points. Once liquefied, cells undergo nucleation based on probabilistic nucleation mechanism governed by local thermal history. Nucleated cells subsequently can evolve into crystalline states, and the crystallization process completes once a cell is fully surrounded by crystalline neighbours. These rules enable the CA model to replicate stochastic nucleation and deterministic crystal growth effectively.

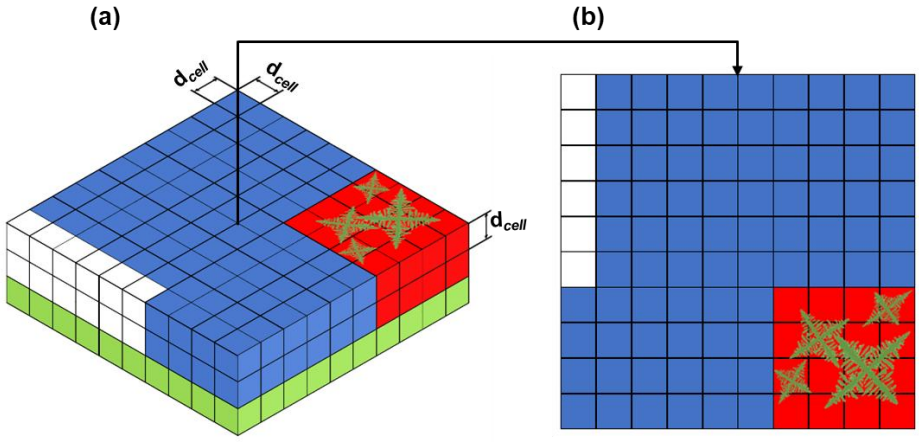


Figure 2.1 (a) 3D CA representation: green, blue, red, and white represent solidified, liquid, growing and powder cells, respectively. Each cell stores its state (S), temperature (T), crystallographic orientation (O) and the unique index (I); (b) 2d representation

Table 2.1 Transition rule of CA cells

Rule of transition	State index of the cell before transition	Transition rule	New state of the cell after transition
Powder	0	$T_{max} \leq T_l$	0
Melting	0	$T_{max} \geq T_l$	1
Nucleation	1	The cell pass the nucleation conditions	2
Crystal growth (activation)	2	Cell's undercooling is greater than a critical temperature	3
Retirement of the cell	3	All the nearest neighbours are captured	4

The neighbourhood configuration is another aspect of the CA modelling [91]. Depending upon the nature of the process, a particular neighbourhood configuration must be selected. In additive manufacturing, two primary neighbourhood configurations are commonly employed: the Von Neumann neighbourhood [12] and the Moore neighbourhood [72]. In two dimensions, the Von Neumann neighbourhood consists of the focal cell and its four orthogonally adjacent neighbours (top, bottom, left, and right). In three dimensions, it similarly includes the focal cell and its six orthogonal neighbours (front, back, left, right, top, and bottom). By contrast, the Moore neighbourhood expands upon the Von Neumann framework by incorporating diagonal interactions, resulting in eight neighbours in 2D and twenty-six in 3D [67,92]. Figure 2.2 and Figure 2.3 illustrate these two configurations for two-dimensional and three-dimensional spaces, respectively. While the Moore neighbourhood provides a more comprehensive representation of local interactions which is particularly valuable for capturing diagonal effects, it also entails a slightly higher computational cost [67]. Nonetheless, it is frequently selected for its advantageous balance between physical realism and numerical efficiency.

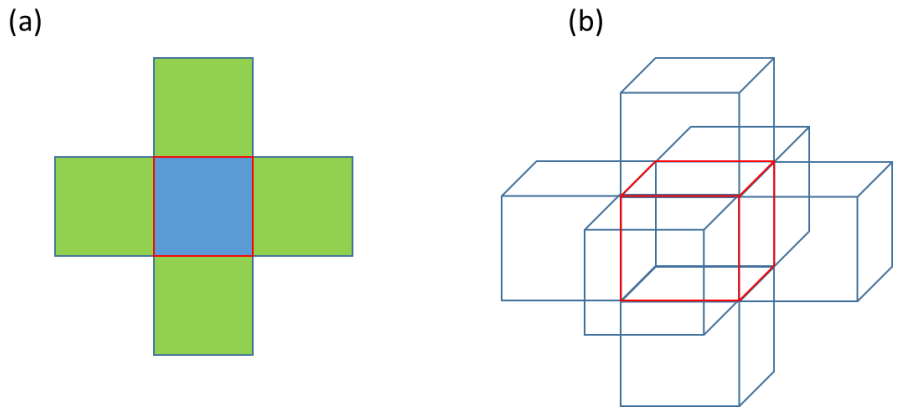


Figure 2.2 Von-Neumann neighborhood configuration: (a) in 2 dimension space and, (b) in 3 dimensional space

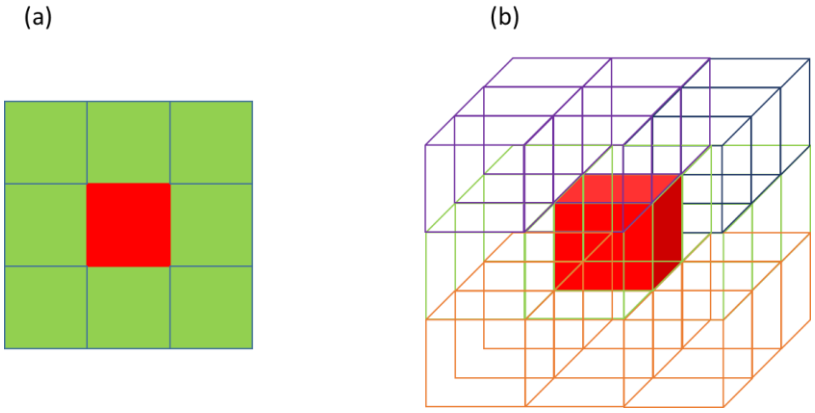


Figure 2.3 Moore's neighborhood configuration: (a) in 2-dimension space and, (b) in 3 dimensional space

2.3 Nucleation Mechanisms

Nucleation plays a crucial role in the microstructure evolution during additive manufacturing. Experimental studies on the LPBF process reveals the presence of both columnar and equiaxed grains [36]. Their proportions are often controlled by the processing parameters of LPBF. These grains often form due to a different nucleation mechanism. The two most reported types of nucleation in AM are: (1) Bulk nucleation [16,22] and, (2) epitaxial nucleation [23]. The schematic of the nucleation mechanism is depicted in Figure 2.4.

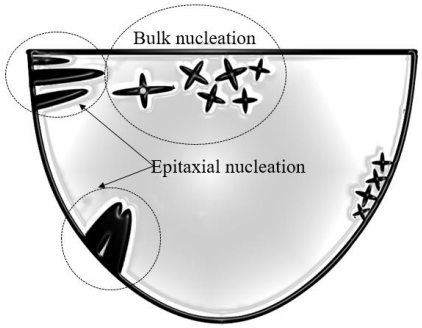


Figure 2.4 Schematic representation of the type of nucleation considered

As discussed in the introduction, bulk nucleation in MAM leads to equiaxed grains while epitaxial nucleation is the source of the columnar grains. To incorporate these nucleation processes, in the current model a heterogeneous nucleation approach is considered which is consistent with the physical observation in LPBF [12]. As explained in Section 1.3.2.2, heterogeneous nucleation occurs at energetically favourable sites, such as pre existing solidified surfaces (epitaxial nucleation) , partially fused particles, or oxide inclusions (bulk nucleation), which lower the nucleation barrier. Owing to the complexity of nucleation in the liquid, nucleation is usually modelled as a phenomenological process [12]. Therefore, the developed CA model is based on the enriched stochastic nucleation mechanism. Under this mechanism, nucleation may occur in the bulk as well as on the pre-existing solidified layer (epitaxial nucleation). The sites of nucleation are predetermined using equations (2.1) and (2.2):

$$N_v = \emptyset_v . V \tag{2.1}$$

$$N_s = \emptyset_s . S \tag{2.2}$$

where N_v is the total number of bulk nucleation sites, N_s is the total number of surface nucleation sites, V is the total volume, S is the total surface area, $\emptyset_v$ (m^{-3}) and $\emptyset_s$ (m^{-2}) are volume and surface nucleation densities. The parameters $\emptyset_v$ and $\emptyset_s$ are the model input parameters. These parameters depend on the process parameters and are

based on the experimental observations. The core of the nucleation mechanism is stochastic determination of the nucleation sites. Under this mechanism a random site within the RVE is selected for nucleation and evaluated using a nucleation probability test based on the local undercooling. Specifically, the probability of nucleation is modeled as a Gaussian function of undercooling as given by equation (2.3). For considering bulk nucleation, the pool of cells that can be chosen corresponds to all cells in liquid state, whereas for epitaxial nucleation only the cells in contact with pre-existing surfaces are considered. For each selected site, its corresponding probability of nucleation (p) is calculated based on equation (2.3) and nucleation is accepted only when the evaluated probability (p) is greater than a certain probability (p'). This threshold (p') is generated using the stochastic number generated within the modelling algorithm. If the site satisfies the nucleation condition, then its state changes from 1 (liquid) to 2 (nucleated) as per the transition rule stated in Table 2.1.

$$p = \frac{1}{(\Delta T_\sigma)\sqrt{2\pi}} \exp\left(-\frac{(\Delta T - \Delta T_m)^2}{2((\Delta T_\sigma)^2}\right) \tag{2.3}$$

wherein, p is the probability of the nucleation, ΔT_σ is standard deviation of the probability function, ΔT_m is the mean nucleation undercooling and ΔT is the local thermal undercooling given by:

$$\Delta T = T - T_l \tag{2.4}$$

In above equation T represents the local (cell) current temperature and T_l is the liquidus temperature. Furthermore, the nucleus starts to grow only after its temperature drops below a certain threshold temperature (undercooling) [12,16]. In the present model, nucleation is controlled by a critical undercooling condition. The chosen nucleation site, remains inactive until its local undercooling exceeds the critical undercooling. This critical undercooling (ΔT_{crit}) is assigned randomly for each

nucleation site based on Gaussian probability distribution and is calculated as per equation (2.5).

$$p((\Delta T_{crit})_i) = \frac{1}{(\Delta T_\sigma)\sqrt{2\pi}} \exp\left(-\frac{(\Delta T - \Delta T_m)^2}{2((\Delta T_\sigma)^2}\right) \quad (2.5)$$

Where ΔT_m and ΔT_σ are the mean and standard deviation, respectively. The actual values ΔT_{crit} are sampled randomly from this distribution and assigned to individual nucleation sites. Once the local undercooling exceeds its assigned $(\Delta T_{crit})_i$, the nucleation site becomes activated (please refer Table 2.1) and subsequently grows according to the crystal growth mechanism. The flow chart for the nucleation algorithm is presented in Figure 2.5.

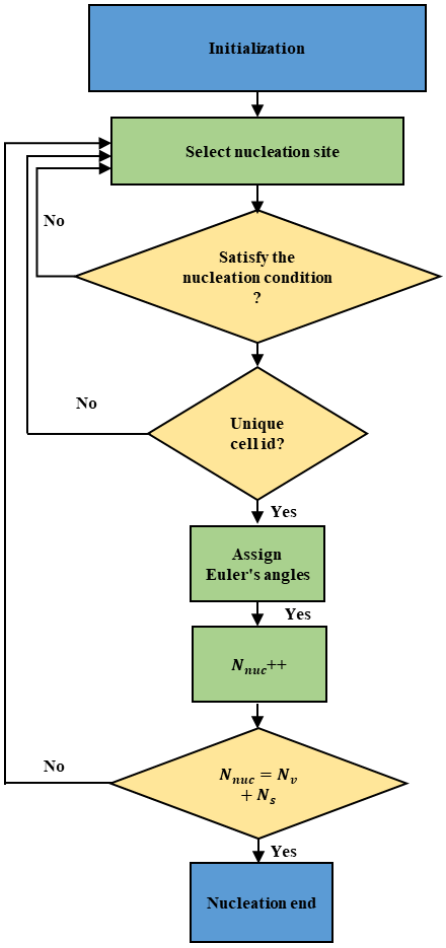


Figure 2.5 Flowchart for the nucleation algorithm within CA model

2.4 Crystal growth and crystallographic orientation

Once the state of a site changes to nucleated (state 3; please refer Table 2.1), it begin to grow and is assigned a unique index number which is the representative of its crystallographic orientation. The cell then follows the rules defined by the growth model. The mechanism for assignment of the crystallographic orientation and the growth model is discussed in subsequent subsections.

2.4.1 Crystallographic orientations of the nuclei

As discussed in section 1.3.5.1 and 1.3.5.4, the texture development in LPBF is primarily controlled by the solidification texture mechanism [55,93]. This mechanism implies that, during solidification, grains tend to grow preferentially along crystallographic orientations that are closely aligned with the local thermal gradient. The final texture of LPBF components can, be in some cases, altered by solid state transformations while cooling like in the case of martensitic steel [94]. However, in MAM especially LPBF, the initial crystallographic orientation of the nuclei dominates the final texture of the specimen [95]. Furthermore, researchers have shown in their studies that in metals with a cubic lattice structure, during solidification, the {100} directions align with the maximum thermal gradient direction [55,93,95]. In the present model, the crystallographic orientation assignment algorithm for the nuclei is based on these finding from the literature. To begin with, the orientation at a nucleation site is established by determining the direction of the maximum local thermal gradient. The temperature gradient ($\nabla \mathrm{T}$), is computed from the spatial temperature field $T = f(x, y, z)$. At any given nucleation point with coordinates (x_n, y_n, z_n) the normalized temperature gradient vector $\mathrm{u_T}$, is defined by:

$$\mathrm{u_T} = \frac{\nabla \mathrm{T}}{\|\nabla \mathrm{T}\|} \tag{2.6}$$

This unit vector, u_T, characterizes the local direction of steepest increase in temperature. For practical simulations, the direction of the maximum thermal gradient, $\boldsymbol{u_{T_{max}}}(x_n, y_n, z_n)$, is obtained by evaluating and selecting the direction corresponding to the greatest magnitude of gradient among neighbouring points around (x_n, y_n, z_n).

$$u_{T_{max}}(x_n, y_n, z_n) = \max(u_T(x_n, y_n, z_n)) \tag{2.7}$$

Herein, the neighbourhood refers to the immediate 26 (Moore neighbourhood) surrounding lattice points, as described in the previous section. This allows accurate identification of the local direction with the highest thermal gradient. Once this direction is identified, a crystallographic orientation is assigned to the nucleus such that the angle between the local maximum thermal gradient direction and the nearest crystallographic axis of the grain does not exceed 10^o. This is achieved by first assigning the nucleus a random orientation (Φ_1, Φ, Φ_2). This random orientation is evaluated using the algorithm developed by Kuffner [96]. Under Kuffner's algorithm, at first a random number (s) is generated between 0 and 1. This generated value is then used to calculate two scaling factors namely σ_1 and σ_2 as per equation (2.9) and (2.10) respectively

$$\mathrm{s} = \mathrm{rand}() \tag{2.8}$$

$$\sigma_1 = \sqrt{1 - \mathrm{s}} \tag{2.9}$$

$$\sigma_2 = \sqrt{\mathrm{s}} \tag{2.10}$$

Followed by which two independent angles θ_1 and θ_2 were calculated, each uniformly distributed between 0, 2π:

$$\theta_1 = 2\pi \,.\, \mathrm{rand}() \tag{2.11}$$

$$\theta_2 = 2\pi \,.\, \mathrm{rand}() \tag{2.12}$$

On the basis of these parameters, finally the scalar quaternion components q_0, q_1, q_2, q_3 of an uniform random unit quaternion were calculated:

$$q_0 = \sigma_2 \cos\theta_2 ; \tag{2.13}$$

$$q_1 = \sigma_1 \sin\theta_1 ; \tag{2.14}$$

$$q_2 = \sigma_1 \cos\theta_1 \tag{2.15}$$

$$q_3 = \sigma_2 \sin\theta_2 ; \tag{2.16}$$

$$q = q_0 + q_1\hat{i} + q_2\hat{j} + q_3\hat{k}; \tag{2.17}$$

Subsequently, the quaternion orientation representation is transformed into Euler angles Φ_1, Φ, Φ_2 using the standard Z–X'–Z'' Bunge convention. This robust procedure ensures un-biased distribution of the orientations. Figure 2.6, represent the flowchart of the proposed algorithm. It is noted that all calculations in the models are performed using quaternion operations. The transformation to Euler angles serves only the purpose of consistency with common texture visualization software such as MTex [97] and Atex [98]. The pseudocode for the proposed quaternion-based orientation-sampling algorithm is reported in Appendix A.1.

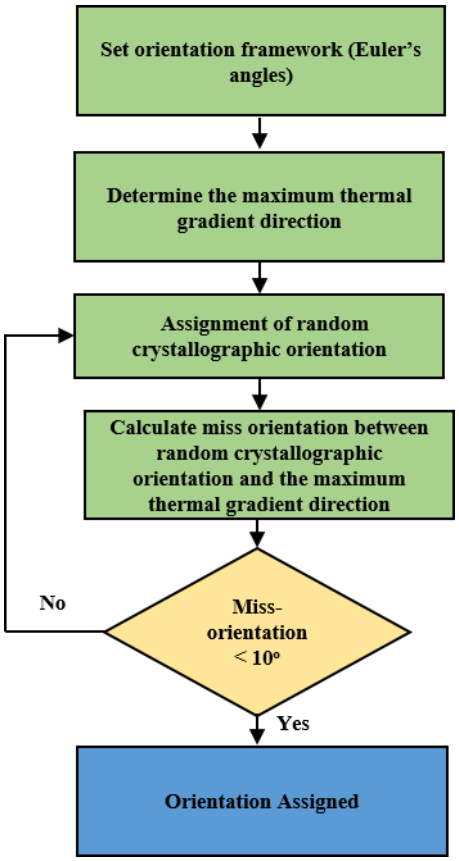


Figure 2.6 Flowchart explaining the assignment of crystallographic orientation to the nuclei based on the thermal gradient

2.4.2 Kinetic growth model

Once, the nuclei are assigned a crystallographic orientation and are activated as defined in equation (2.5), the cell grows under the action of the solidification driving force and infect the neighbouring cells once solidification is completed. The growth velocity of the nuclei plays an important role in the final morphology of the specimen. Therefore, establishing a growth model for the CA simulation is very crucial. The most common growth model used in solidification is the Lipton-Glicksman-Kurz (LGK) model [99] and Kurz-Giovanola-Trivedi (KGT) model [81]. In the present CA model, the LGK model for the dendritic growth is considered. In this model, growth of the nucleated grains is controlled by the dendrite growth kinetics where the rate of the growth is considered a

function of its undercooling ΔT [72]. The undercooling (ΔT) comprises four different components:

$$\Delta T = \Delta T_{th} + \Delta T_c + \Delta T_k + \Delta T_r \tag{2.18}$$

where ΔT_{th} is thermal undercooling and is defined as the difference between the liquidus temperature and the cell temperature, ΔT_c is the constitutional undercooling that is associated with the difference of composition of elements between the solid phase and the liquid phase at the solid-liquid interface, ΔT_k is the kinetic undercooling associated with the transport of atoms from solid phase to liquid and vice-versa. Finally, ΔT_r is the curvature undercooling originating due to formation of solid-liquid interface during solidification [90]. LPBF is subjected to a high thermal gradient, and therefore, in the present model, crystal growth is considered a function of the total thermal undercooling only [100] and hence equation (2.18) can be further reduced to:

$$\Delta T = \Delta T_{th} = T_i - T_l \tag{2.19}$$

It is noted that in conventional solidification, depending on the cooling rate, other contributions cannot be neglected as their magnitude can complete with that of the thermal undercooling. Thermal undercooling can also be expressed using the dimensionless number Ω_t [99], given by:

$$\Omega_t = \frac{\Delta T_{th} c_p}{\Delta H} \tag{2.20}$$

where ΔH is the latent heat, c_p is the specific heat. Moreover, Ω_t can again be defined using the Ivantsov relation [99–102] :

$$\Omega_t = I_v(P_t) = P_t \exp(P_t)\, E_1(P_t) \tag{2.21}$$

wherein, I_v is the Ivantsov function, E_1 is the exponential integral function and (P_t) is the peclet number. When it comes to thermal field, the peclet number is given by:

$$P_t = \frac{V_g R}{2\alpha} \tag{2.22}$$

where V_g is the growth rate of the solid-liquid interface. R is the tip radius of the dendrite and α the thermal diffusivity. Using equations (2.22), (2.23) and (2.24), the undercooling can be expressed as:

$$\Delta T_{th} = \frac{\Delta H}{c_p} I_v \left(\frac{V_g R}{2\alpha}\right) \tag{2.23}$$

In order to further resolve equation (2.23) in ΔT_t and V_g, the stability criterion given by Trivedi [103] and Kurz and Fisher [104] is utilized. Their reduced stability criterion considering only thermal undercooling can be expressed as:

$$R = \frac{c_p \Gamma}{0.05 P_t \Delta H} \tag{2.24}$$

where Γ is the Gibbs-Thomson coefficient. Using equations (2.21), (2.23) and (2.24), the growth rate can be expressed in terms of undercooling. However, solving these equations simultaneously for each cell in CA simulation leads to significant computation load. Therefore, to reduce the computational load a polynomial relationship, often termed as LGK model, between the growth rate and ΔT is usually fitted [99]. This was achieved by solving these equations at every time step Δt. At each step, V_g was calculated and plotted against the undercooling. Thereafter, to reduce the computational effort, a three-order polynomial relationship between the growth rate and ΔT was fitted :

$$V_g = \alpha(\Delta T)^3 + \beta(\Delta T)^2 \quad (2.25)$$

where α and β are the curve fitting parameters which are material dependent and are identified by calculating the V_g at different given ΔT.

2.4.3 Crystal growth

The growth algorithm of the grain in the developed CA model is based on the decentred octahedron algorithm proposed by Gandin et al. [105]. In this approach, the primary dendrites grow along their preferential crystallographic directions. As discussed in Chapter 1.2.5.1, for FCC and BCC metals, the preferential growth direction is <100>. The algorithm developed by Gandhi et al. incorporates it by preferentially propagating the half-diagonals of an octahedron as presented in Figure 2.7.

During the simulation, the decentred octahedron serves as a structured spatial template which determine the possible growth paths from each solidified cell to neighbouring liquid cells. At each simulation step, a growing cell assesses local thermal conditions of its neighbouring cell to determine undercooling and then evaluate the growth speed according to equation (2.25) in all the 26 neighbours. Among these, preference factors are given to the cells, which lies along the half diagonals of the octahedron. The cells keep on growing until it either encounters another growing grain (impingement) or reaches unfavourable thermal conditions. The utilization of this directional algorithm ensures that the crystal growth behaviour simulated by the model closely aligns with actual microstructural evolution, enhancing the predictive capabilities of the developed CA model.

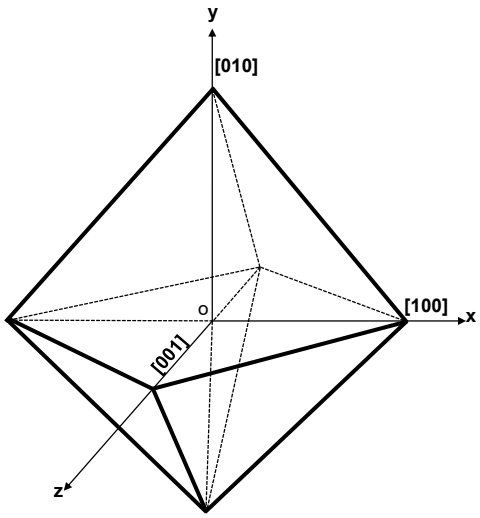


Figure 2.7 A regular octahedron depicting the preferential growth direction of the primary dendrites

2.5 Coupling of finite element method and cellular automaton

The temporal thermal profile of the RVE is core of the microstructure simulation. The temporal profile of the RVE dictates the microstructural development such as growth kinetics, nucleation rates, and resultant crystallographic texture. In the original Cellular Automaton (CA) model developed by Gandin et al. [80], the temperature field for each CA cell was determined directly through the finite element method (FEM). However, employing such a direct simulation approach demands significant computational resources. To overcome this limitation, an alternative strategy is implemented wherein the temperature field of the RVE is first obtained independently using the ABAQUS FEM solver and subsequently coupled with CA model. This decoupled approach is widely accepted and extensively utilized among researchers [20,25]. Thermal data obtained using thermal solvers typically, have a coarser mesh size than the CA cells, whose resolution must be defined by microstructural features occurring at lower length scales. This is usually done to make the simulations technically affordable. The coupling procedure involves superimposing the CA cells onto the FEM mesh, as depicted in Figure 2.8 (a). In the present work, the temperature at each CA cell is

computed at every time step by trilinear interpolation from the surrounding FEM nodes, as illustrated in Figure 2.8 (b). The temperature of any ith cells at any given time step is given by :

$$(T_i)_j = T_j{}^T Q \tag{2.26}$$

where $(T_i)_j$ is the interpolated temperature of ith cell of the CA at any time j, T_j is the temperature field vector of the 8 nearest neighbors (see Figure 2.8 (b)) and Q is the distance vector related with the ith cell. Selection of time step is another vital component of CA simulation. In this thesis work, an adaptable time step has been implemented wherein, the time step for the CA is chosen such that the crystal growth never exceeds 0.2 times the cell size in one type step:

$$\Delta t = 0.2 \left(\frac{d_{cell}}{max\ (v_g)} \right) \tag{2.27}$$

where d_{cell} is the CA's cell size, v_g is the growth rate (m/sec) and the max function ensures to consider the maximum growth rate within the simulation domain. This approach ensures that the time steps are adaptively adjusting its resolution (Δt) based on the undercooling of the cells. Meaning that higher the growth rate, lower will the time step. This ensures a proper morphological development. Furthermore, the time step for the CA simulation is typically finer than the one used in the FEM simulation for determining the temperature field. Therefore, for determining the nodal temperature of the cell at a specific time t_j between two adjacent time steps of the FEM simulation, a linear interpolation technique was used:

$$T_p^j = \frac{T_p^n - T_p^{n-1}}{t^n - t^{n-1}} \left(t_j - t^{n-1} \right) + T_p^{n-1} \tag{2.28}$$

where the subscripts n and n-1 represent the current and the previous time steps of the FEM domain, t_j is any time such that $t^n \leq t_j < t^{n-1}$ and , T_p^j is the temperature of the pth node at t_j.

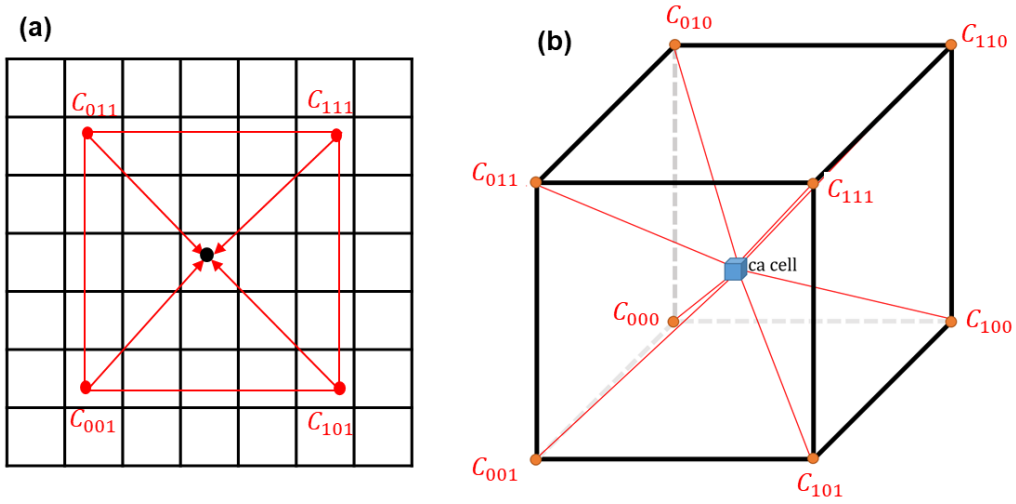


Figure 2.8 (a) Coarser FEM mesh overlapping fine mesh of CA; (b) schematic representation of the tri-linear interpolation technique.

2.6 Parallelization technique

The CA simulation domain often contains millions of cells depending upon the discretization and the size of RVE [67]. As discussed in section 2.2, each of these cells stores crucial state information including phase, temperature, grain index, and crystallographic orientation. During the simulation, each of these cells undergoes frequent state transitions based on their local thermal conditions. For example, a single cell might melt, remelt, nucleate, or grow over different time steps. These transitions involve updating its internal variables and sometimes reallocating its data to different memory spaces. These operation require intensive memory access for reading and modifying the data stored for each cell. These continuous updates lead to intensive memory operation which is referred as memory shuffling [67]. Such operations hamper performance based on the available computing device memory. Furthermore, simulation of microstructure evolution in LPBF requires considering large simulation

domains to represent the microstructural features caused by the melt pools that often extend beyond the microscopic scale. It is noted also that physically faithful simulations of microstructure phenomena requires large RVEs and the consideration of numerous microstructure features to overcome the initial transient caused by departing from initial setups off equilibrium [89]. Simulating, such a microstructural volume significantly increases the time scale. This mandates the development of the parallelized CA models. Therefore, in this work, CA model was parallelized using C++ and the message passing interface (MPI) standard. Wherein, a static domain decomposition strategy within a parallel computing architecture was applied. In this approach, the RVE domain is partitioned into multiple sub-domains. The number sub-domains is equal to the number of processors assigned for the parallel computing. Under the developed model, the workload is evenly distributed among the processors. By evenly distributing the simulation workload among these processors, each one performs its computations independently. Communication between processors, which is needed to guarantee the contiguity of the RVE, is achieved by the MPI to exchange data. Figure 2.9 illustrates this strategy, with the digital interface acting as a boundary to separate the subdomains. This interface ensures that each processor is aware of its designated portion of the overall domain, thereby preventing interference with other processors' computations. Communication and exchange of necessary information between neighbouring subdomains occur through this interface, as depicted in Figure 2.9 (b). For a clearer understanding, a simplified example in Figure 2.9 (a) is presented, where the entire computing domain was divided into four subdomains, each separated by a digital domain boundary. Subdomains 1 and 4 are initially seeded with one nucleus each. As these nuclei grow and encounter the boundary of their respective subdomains, critical growth-related information is stored in the interfaces. Later, this information is communicated to the corresponding subdomains, allowing the growth to continue seamlessly. Overall, employing the static domain decomposition strategy within the

parallel computing architecture addresses the memory limitations of CA and facilitates efficient and reliable large simulations.

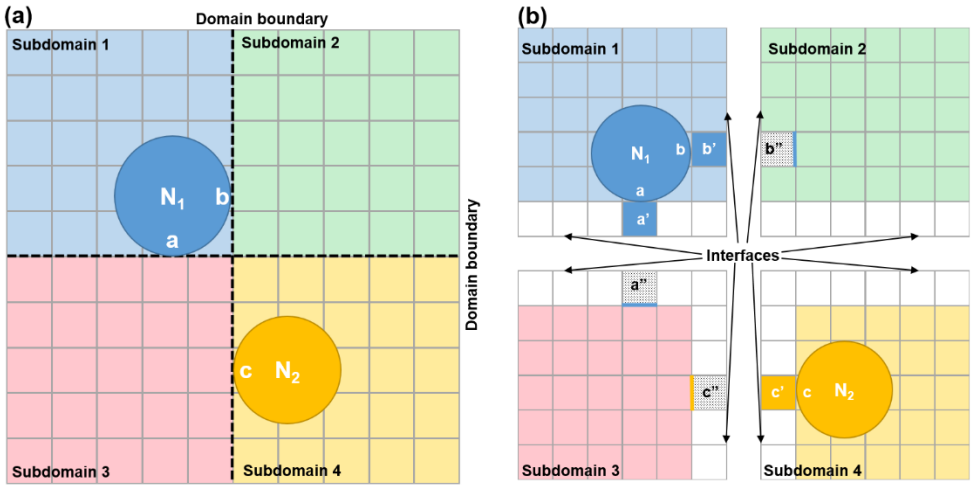


Figure 2.9 (a) RVE domain decomposed into 4 subdomains, dashed lines represent the subdomain boundaries, subdomain 1 and subdomain 4 contain active nuclei N1 and N2, a, b and c represent the cells via which the nuclei touch the boundary. (b) When nuclei encounter the subdomain boundaries, additional ghost layers (a', a", b', b", c', c") are introduced to ensure proper information transfer across subdomains, thereby allowing growth to be tracked consistently without discontinuities.

2.7 A novel algorithm handling redundancies arising from remelting in LPBF

The LPBF process is a layer-by-layer process as outlined in the introduction, which involves repeated melting and solidification cycles. This is an inherent feature of LPBF which happens due to overlapping between successive laser passes and the molten layers. Moreover, depending on the process parameters, a volume ranging from 10% to 80% undergoes remelting throughout the entire process [24]. While such an overlapping is necessary for complete fusion of the materials, this adds up extra burden to the computational domain. In the developed model, a unique algorithm has been embedded which handles the redundancies of the remelting cycle. The present CA operates in a way that only active (solidifying) cells are considered at each time step. The performance

of the CA model depends on the amount of solid/liquid (or generally transformed/untransformed) interface per time step, whose maximum has been found to occur at approximately 50% of the volume fraction of the transformed/solidified phase [106]. As a result, the performance of the model suffers from the non-continuous evolution of the transformed volume fraction since remelting events essentially reset the system to a previous state. Furthermore, these events must be explicitly implemented by shuffling memory algorithms whose performance is well-known to be low [107]. The proposed CA model in this contribution, on the other hand, has a distinctive approach for considering remelting and solidification during LPBF. This allows enhancing the speed of the CA model for faster and more efficient simulations while maintaining accuracy and reliability. To this aim, the temporal thermal field of the CA cells has been used to define the conditions (temperature and time) at which a cell will, with absolute certitude, solidify without further remelting. Figure 2.10 illustrates the schematic framework designed to prevent redundancy resulting from remelting in LPBF.

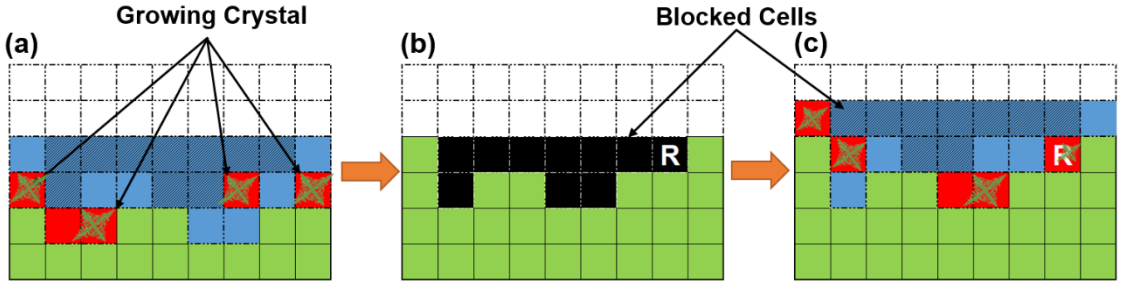


Figure 2.10 Schematic representation of the framework for avoiding redundancy because of remelting in LPBF: (a) RVE representing the growth of dendrites at a time t_{n-1}: green cells are solidified, blue cells are liquid state, hatched cells will be re-melted at next time interval and therefore, are not available for nucleation and crystal growth, red cells are growing cells with activated nuclei; (b) RVE representing the cells after complete solidification at time t_i ($t_i > t_{n-1}$), where black cells represent the cells that were melted at t_{n-1} and will be melted again at t_n ($t_n > t_i > t_{n-1}$) and were never activated in the previous time step; (c) RVE of the cells at time t_n, where several cells have melted again and were activated based on their respective temperature profile.

This image depicts a RVE at different time steps; in it solidified cells are shown in green, liquid state cells in blue and red cells signify growing cells with activated/solidifying nuclei. The hatched cells on the other hand are designated for remelting at the next time interval, rendering them unavailable for nucleation and crystal growth at time $t_I < t_n$

(where t_I is the instantaneous time and t_n is the time after which the temperature of a cell will not exceed the liquidus temperature). The cells whose temperature exceed the liquidus temperature of the material more than once are designated as re-melted cells. All such cells will be available for a nucleation event or crystal growth only at time t_n after which it does not melt. The time t_n for each cell is computed using its temperature history curve. Such a temperature history profile for a cell marked with "R" in Figure 2.10 is presented in Figure 2.11. It could be seen that this cell melts twice, first at time t_{n-1} and then again at time t_n. Therefore, in the present framework, this particular cell will be part of the simulation only at a time greater than t_n, thereby avoiding any redundant nucleation and crystal growth. Once the certain nucleation time t_n for the cells has been determined, the cells are categorized according to this time in time series lists that are defined by discretizing the total simulation time in intervals smaller than the time needed for a laser track to complete its displacement. The interval of a time series is defined by a range $[t_{min}, t_{max}]$. The simulation is accelerated by considering in a time step only the active/solidifying cells and nuclei cells within lists in which the current simulation time t lies between t_{min} and t_{max}. Such an algorithm aims to reduce the computational load and clubbed with parallelized computation will allow the large RVE to be simulated. The pseudocode for the proposed algorithm is reported in Appendix A.2

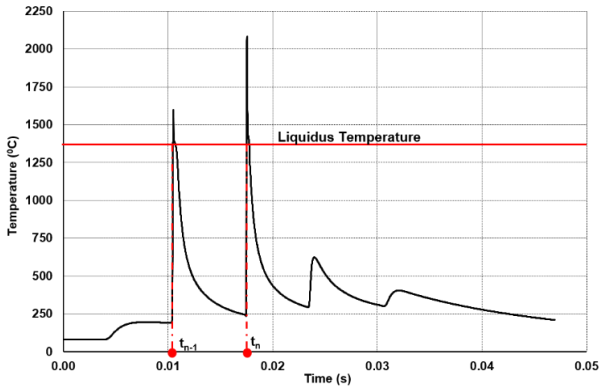


Figure 2.11 Temperature-time profile of cell R in Figure 2.10: this cell melts twice during the process, namely at tn-1 and tn.

2.8 Conclusion

In this chapter, the development of an accelerated three-dimensional CA model for simulating microstructure evolution in the LPBF process was described. The model was designed to capture key solidification phenomena such as nucleation, crystallographic orientation, and crystal growth. A crystallography-based growth algorithm was implemented to reflect the directional nature of dendritic growth. The model was coupled with a finite element thermal simulation to ensure a realistic temperature fields to guide the evolution. To address the computational redundancies which arises due to repetitive remelting in LPBF, a novel algorithm was introduced. Furthermore, to support large-scale simulations, the model was parallelized using a domain decomposition approach. Overall, the developed CA framework provides a computationally efficient tool for investigating microstructure evolution in LPBF. The basic structure of the CA model is exemplified in Figure 2.12 by its flowchart. The following chapters includes the model performance, model validation and the application of the developed model to predict the microstructure evolution of additively manufactured X30Mn21 high manganese high strength steel alloy.

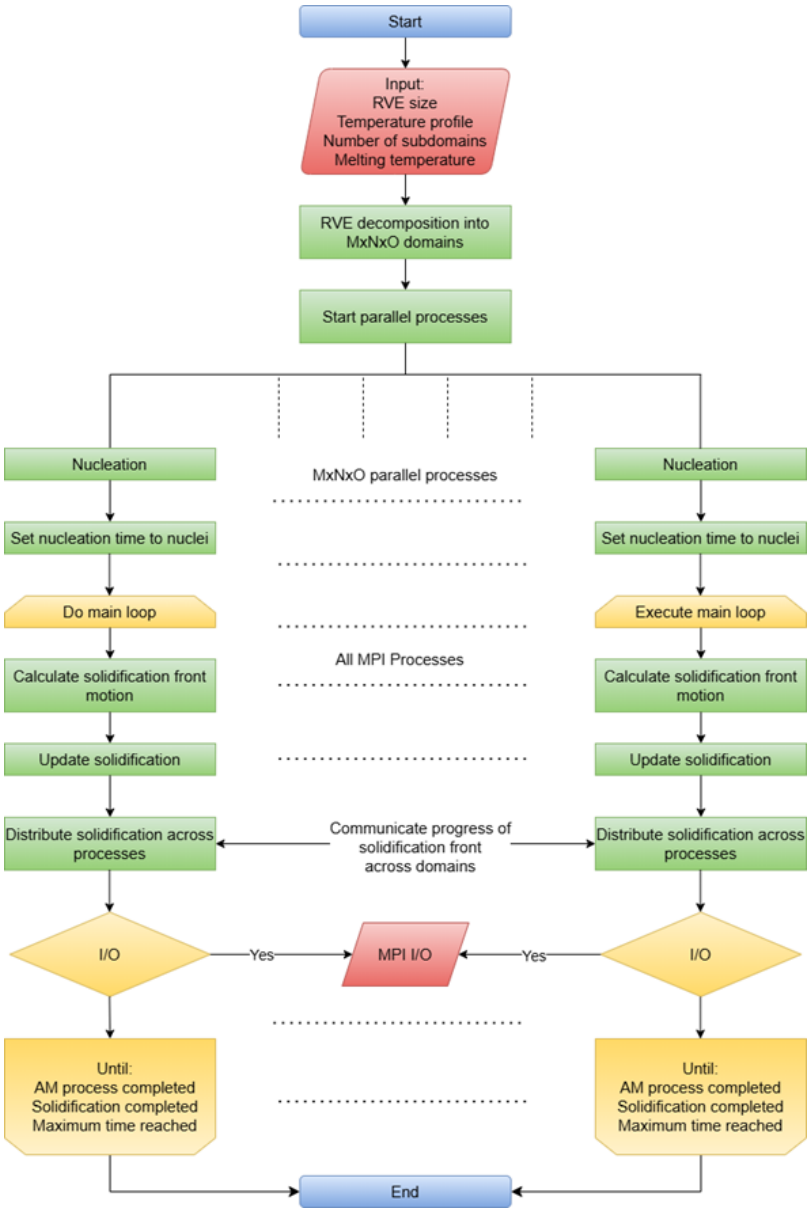


Figure 2.12 Program flowchart where $M \times N \times O$ processes are started in parallel. Data is globally shared before domain subdivision. Once parallel execution begins, all tasks are performed locally with communication exchanges occurring periodically. Execution continues until the AM process ends or the full melting of the powders and solidification are completed, or the maximum user-defined maximum solidification time is reached

Chapter 3

Model Validation

3.1 Introduction

This chapter presents the validation of the RA-CA model developed in Chapter 2. Before moving toward its application in real setups and comparison with experiments, it is important to check if the model behaves in a stable and physically consistent manner under typical LPBF conditions. Two of the most critical factors that influence grain morphology and texture in LPBF are nucleation and growth kinetics. Since the RA-CA model has a novel approach of handling remelting and solidification cycles, it is important to evaluate whether it can still correctly capture the effects of nucleation mechanism and spatial grain development.

To do this, the present chapter explores how the model responds when different nucleation setups are applied namely, bulk, epitaxial, and a combination of both and, different growth kinetics. This helps in checking how well the model handles directional solidification, grain competition, and the emergence of equiaxed structures under varying nucleation strategies. The test material chosen for all simulations is X30Mn21, a single-phase FCC austenitic advanced high-strength steel. This same material is used later for experimental validation (Chapter 4) and property linkage development (Chapter 5).

3.2 RA-CA Simulation Setup

The simulations were carried out with a cubic domain of 400 µm × 400 µm × 400 µm discretized using a cell size of 1 µm. The nucleation mechanism, including both epitaxial and bulk seeding, followed the stochastic framework described in Section 2.3. The sensitivity of simulation results to different nucleation mechanisms is studied in the subsequent sub sections. For all simulations, nuclei were assigned a crystallographic orientation based on the direction of the local thermal gradient, as discussed in Section 2.4.1. Specifically, the orientation assignment favored the <100> direction aligned with the maximum thermal gradient.

The required material properties such as specific heat, thermal conductivity, and density are listed in Table 3.1. The kinetic growth relationship followed the LGK type model, where the growth velocity V_g is expressed as a second-order polynomial function of undercooling ΔT , as described in equation (2.25) of Section 2.4.2. The influence of deviations from these baseline kinetic parameters is examined in Section 3.2.3.

$$V_g = \alpha(\Delta T)^3 + \beta(\Delta T)^2 \qquad (2.25)$$

The coefficients α and β are fitted for X30Mn21 as shown in Figure 3.1 and its value are presented in Table 3.1. The RA-CA model was coupled with the thermal field as described in Section 2.5, and the time step used was adaptive as outlined in the same section. The 3D morphology of the simulated microstructure was visualized using paraview [108] and the corresponding microstructure was analyzed using Atex software [98].

Table 3.1 Thermo-physical properties of X30Mn21 and calculated growth coefficients

Property	Value	Unit
Liquidus temperature (T_l)	1699.23	K
Solidus temperature(T_s)	1648.87	K
Specific heat (c_p)	712	$Jkg^{-1}K^{-1}$
Enthalpy of fusion (ΔH)	280	Kj kg^{-1}
Thermal diffusivity (α)	15.2E-6	m^2s^{-1}
Gibbs-Thomson coefficient (Γ)	2.3E-7	Km^{-1}
growth coefficients α	9×10^{-6}	m k^{-3}
growth coefficients β	3×10^{-3}	m k^{-2}

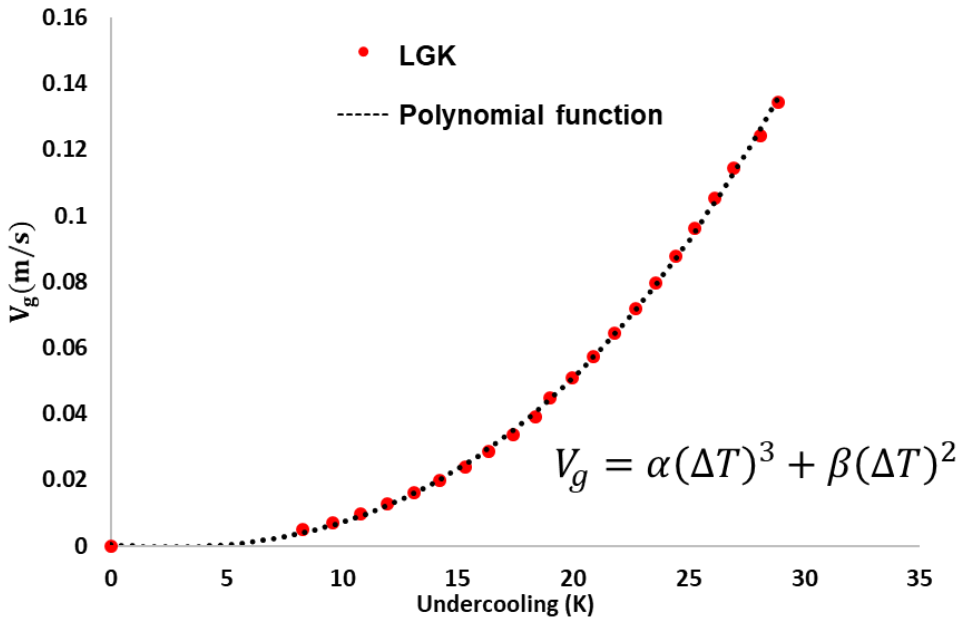


Figure 3.1 Growth velocity as a function of undercooling for X30Mn21 alloy wherein the red circles represent LGK model calculations, while the dashed line shows the second-order polynomial fit used in the RA-CA simulations. α and β are the polynomial coefficients

3.2.1 Thermal Field Generation

Since the focus of this thesis is on the development and performance of the Cellular Automaton (CA) model, the thermal field used for simulations were generated externally using a finite element-based thermal simulation in ABAQUS. The details of this simulation are presented here for completeness.

The LPBF thermal model used a control volume approach, dividing the domain into powder and solidified material. The laser source was modelled using the DEFLUX subroutine and had a Gaussian profile with a spot size of 80 µm. The laser absorption coefficient was set to 0.41 based on an Nd:YAG laser [109] and laser power was set us 120 W. The thermal simulation was done on a 1 mm × 1 mm × 0.4 mm domain. From this, a smaller volume of 400 µm × 400 µm × 400 µm was taken for the CA simulation (see Figure 3.2 (d)). Five tracks were simulated using a bidirectional scan strategy with a hatch of 70 µm and scan speed of 950 mm/s. Between each scan, a laser-off time of 190 µs was used. Temperature dependent material properties like thermal conductivity, specific heat, and density as well as the liquidus temperature ($T_{liquidus}$) and solidus temperatures ($T_{solidus}$) of the X30Mn21 alloys were calculated using Thermo-Calc and the TCFE9 database. The temperature dependence of thermal conductivity, specific heat, and density is reported in Figure 3.2 (a-c).

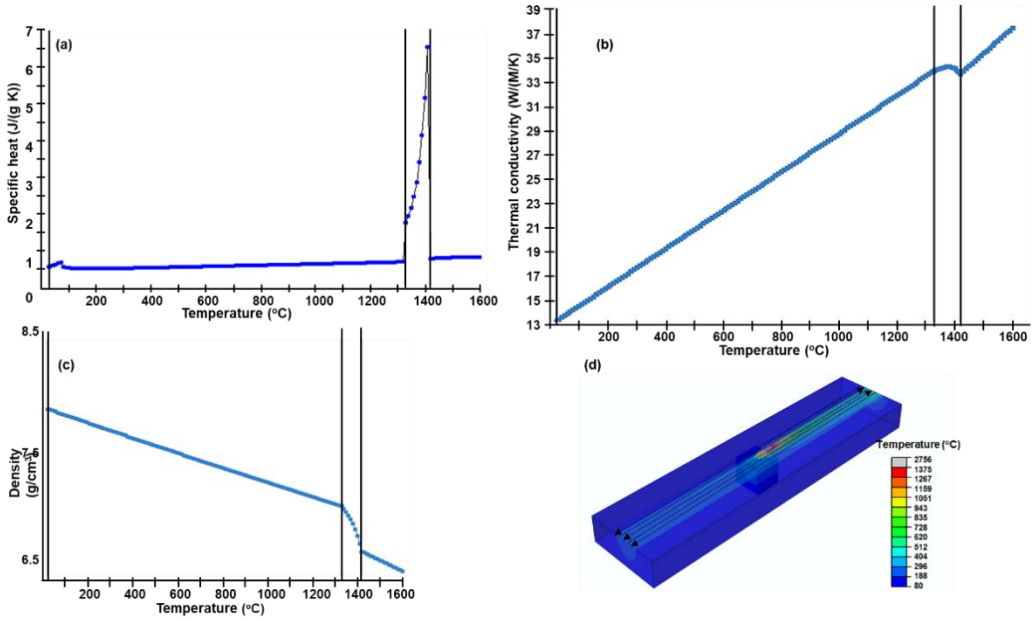


Figure 3.2 Temperature dependent thermos-physical properties X30Mn21 alloy (a) specific heat, (b) thermal conductivity, (c) density and,(d) Isometric section of the thermal simulation indicating the sub-section taken for CA simulation [110]

3.2.2 Effect of Nucleation type

To study the influence of different nucleation strategies on the simulated grain structure, three separate configurations were tested (i) only bulk nucleation, (ii) only epitaxial nucleation, and (iii) both bulk and epitaxial nucleation. In all three cases, the total number of nuclei was kept constant to ensure fair comparison.

For this setup, the nucleation density was chosen arbitrarily not to match experimental data but to simply check whether the RA-CA model behaves logically and consistently under different seeding mechanisms. This approach allows the model's response to be evaluated independently of tuning parameters. The nucleation density employed is listed in Table 3.2 and is adapted from the work carried out by Teferra et. al [25].

Table 3.2 Nucleation density for different simulation

Simulation ID	Type of nucleation	Nuclear density
Simulation 1	Only Bulk	$\emptyset_v = 10^6\ mm^{-3}$
Simulation 2	Only Epitaxial	$\emptyset_s = 10^6\ mm^{-2}$
Simulation 3	Both bulk and epitaxial	$\emptyset_s = 5X10^6\ mm^{-2};\ \emptyset_v = 5X10^6\ mm^{-3}$

3.2.2.1 Grain Morphology and Surface Structure

The simulated 3D grain morphologies for different nucleation strategies are shown in Figure 3.3 (a-c). All three configurations display grains that grow predominantly along the build direction, which is expected due to the steep vertical thermal gradient in LPBF. In the case of only bulk nucleation (Figure 3.3 (a)), grains appear more fragmented and less directional. These grains originate throughout the melt pool volume, resulting in high grain density and more frequent grain boundary intersections. Furthermore, at the centerline of the melt pool, fine grains can be observed. These grains are mostly equiaxed in shape and likely form due to the combination of low G/R ratio (thermal gradient to solidification rate) and high undercooling available in that region. This promotes heterogeneous nucleation and limits directional growth, a trend commonly reported in LPBF studies [111]. This phenomenon is commonly observed in the experiments [51,112].

In contrast, when only epitaxial nucleation is used Figure 3.3 (b) long and continuous columnar grains span the entire melt pool depth. These grains nucleate at the previously solidified interface and grow along the thermal gradient direction with minimal disturbance. Moreover, since the nucleation was restricted to the solid liquid boundary, there are no new grains originating from the central or top regions of the melt pool, which often halts the growth of columnar grains [48]. As a result, no equiaxed zone is seen along the centerline, and the grain boundaries remain parallel and directional.

The simulation results with both bulk and epitaxial nucleation (Figure 3.3 (c)) shows a behavior, which is commonly reported in literature. From Figure 3.3 (c), it is evident that the long columnar grains are still present due to epitaxial growth at the interface, but there also exist additional fine grains, especially in the center region. These grains appear to partially interrupt the growth of some columnar grains, causing grain boundaries to curve, deflect, or terminate earlier. This indirect pinning effect from randomly distributed bulk nuclei creates more fragmentation in the columnar structure, contributing to a mixed morphology of elongated and equiaxed grains. Similar grain competition and impingement behavior has been discussed in prior LPBF modeling studies [113,114].

The grain structure at the top surface is shown in the bottom row of Figure 3.3 (d-f). The bulk-only case (Figure 3.3 (d)) resulted in dense and fine-grained structure, as grains form throughout the melt pool and grow upward. In contrast, the epitaxial-only case (Figure 3.3 (e)) produced large, widely spaced grains at the surface due to the limited number of nucleation points. The combined case again shows balanced grain shapes that remain elongated, but the surface appears more refined than the epitaxial case. Such a kind of morphology is reported in the experiments [115,116].

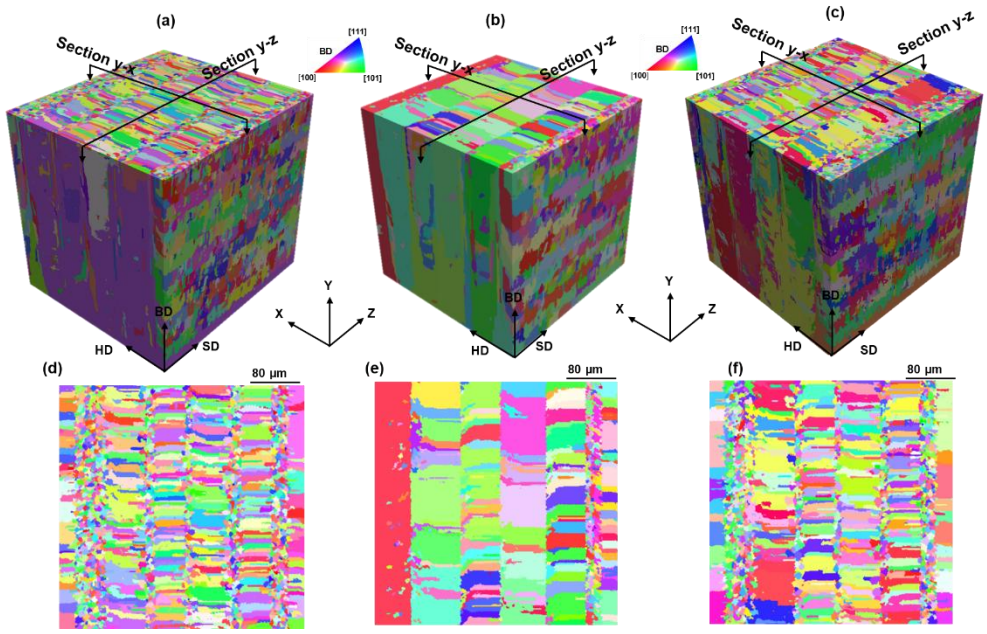


Figure 3.3 Simulated grain morphologies (top row) and corresponding top view (bottom row) for different nucleation strategies: (a, d) only bulk, (b, e) only epitaxial, and (c, f) both bulk and epitaxial nucleation. Section planes are marked in the 3D views.

3.2.2.2 Texture and Orientation Distribution

The 2D grain maps along XY and YZ section (please refer Figure 3.3) is reported in Figure 3.4 and Figure 3.6 respectively. The corresponding IPFs are reported in Figure 3.5 and Figure 3.7. The IPFs help in understanding how grains orient relative to the build direction (BD) for the different nucleation strategies.

In the XY plane (Figure 3.4), the <101> || BD orientation appears to be dominant in the simulations which include epitaxial nucleation (Figure 3.4 (b) and (c)). This is also evident from the corresponding IPF plot in Figure 3.5. Furthermore, the simulation having only epitaxial nucleation, the <100> || BD texture also dominates. In contrast, the bulk nucleation case exhibits strong texture close to <311> || BD (Figure 3.4(a) and Figure 3.5 (a)). This indicates that while grains generally tend to align along the BD, there is some

spread between preferred orientations. This kind of intermediate texture is common when grains nucleate throughout the melt pool volume and are slightly misaligned due to local variations in the thermal gradient [25].

In case of only epitaxial nucleation (Figure 3.4 (b)), the IPF map shows highly aligned columnar grains along the build direction, and the IPF triangle (Figure 3.5(b)) clearly shows a sharp peak near <101>. This confirms a strong <101> || BD texture, which is expected because the epitaxial grains originate from the solid/liquid interface and grow in line with the thermal gradient. Epitaxial growth is known to produce stronger textures as it suppresses the randomness associated with bulk nucleation. Similar trends are found in EBSD based studies of LPBF 316L and Inconel 718 alloys where columnar <101> or <001> textures dominate under epitaxial growth[117,118] .

When both nucleation types are included (Figure 3.4(c)), the grain orientations remain fairly aligned along the BD, but the texture intensity is slightly lower (Figure 3.5(c)). This is because the addition of bulk grains introduces some competition with the epitaxial grains. These bulk nuclei, while still growing along the gradient, are not always perfectly aligned, resulting in a broader orientation spread and a softened texture. Interestingly, despite the random placement of bulk nuclei, the thermal gradient still dominates the growth direction, which keeps most orientations tilted toward <101>. This confirms that the gradient-driven growth mechanism, built into the RA-CA model, is effective in capturing realistic grain behavior.

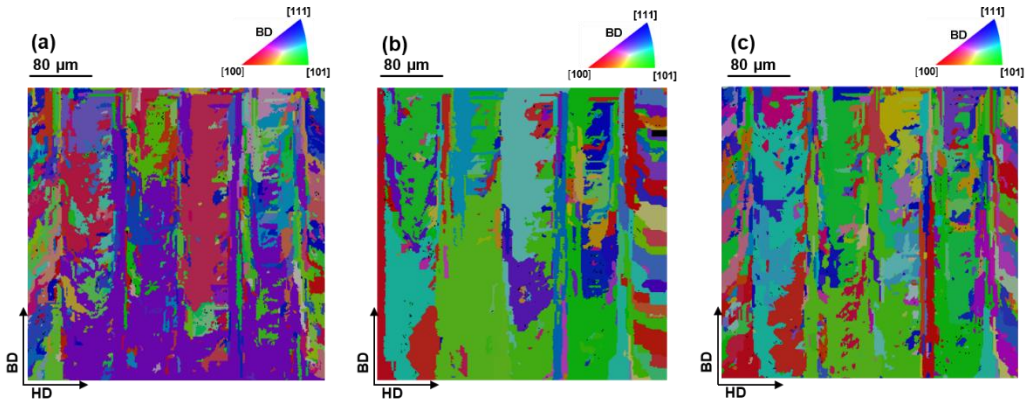


Figure 3.4 IPF map of the Y-X section (a) only bulk, (b) only epitaxial, and (c) both bulk and epitaxial nucleation.

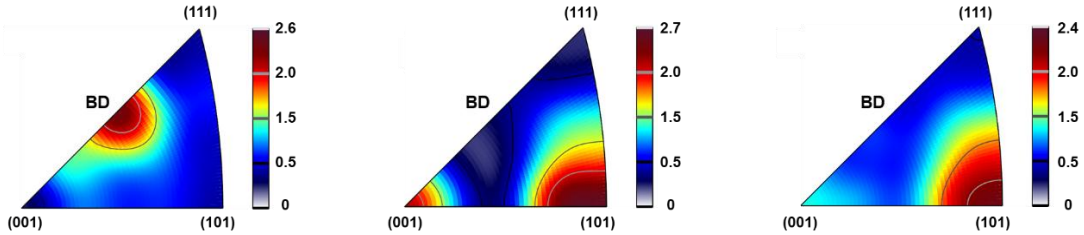


Figure 3.5 The IPF of Y-X section of the RA-CA simulation with of RA-CA simulation with (a) only bulk, (b) only epitaxial, and (c) both bulk and epitaxial nucleation

The trends observed in the YZ section (Figure 3.6) are consistent with those seen in the XY section (Figure 3.4), demonstrating the model's ability to produce coherent texture evolution across orthogonal planes. This consistency reinforces the physical validity of the growth rules embedded in the model

In the simulation with only bulk nucleation (Figure 3.6 (a)), the IPF map again shows a wide range of orientations with a notable <101> preference. The IPF plot (Figure 3.7(a)) confirms this, with intensity clustered near the <101> and <111> orientations. This reflects the random placement of bulk nuclei and local variations in heat flow, leading to more textured but less sharply aligned grains. The simulation with only epitaxial nucleation (Figure 3.6(b)) predicts grains that are much more aligned, especially along the <101> direction, with the IPF plot (Figure 3.7 (b)) showing a strong, sharp peak near <101>. This again supports the idea that epitaxial grains strongly follow the thermal gradient and develop preferred textures. Prior work in LPBF of austenitic steels [4] has

also shown that such textures can lead to anisotropic mechanical behavior due to the alignment of easy slip directions. For the combined nucleation case (Figure 3.6 (c)), the grain orientations resemble the one obtained on the XY cross section but are slightly more aligned. The IPF plot (Figure 3.7 (c)) again shows broadening, but still with the highest intensity near <101>. This result highlights the role of epitaxial grains in steering the growth direction, while bulk nuclei add diversity and break the texture sharpness. This mixed mode texture is useful in cases where controlled grain orientation and reduced anisotropy are desired.

Overall, the simulation results show that the thermal gradient drives grains toward a <101> || BD texture in FCC materials like X30Mn21 which is commonly observed in the experiments [12,119]. Epitaxial nucleation sharpens the texture, while bulk nucleation broadens it. The RA-CA model captures these effects consistently across multiple sections, which supports its reliability for predicting texture evolution in LPBF.

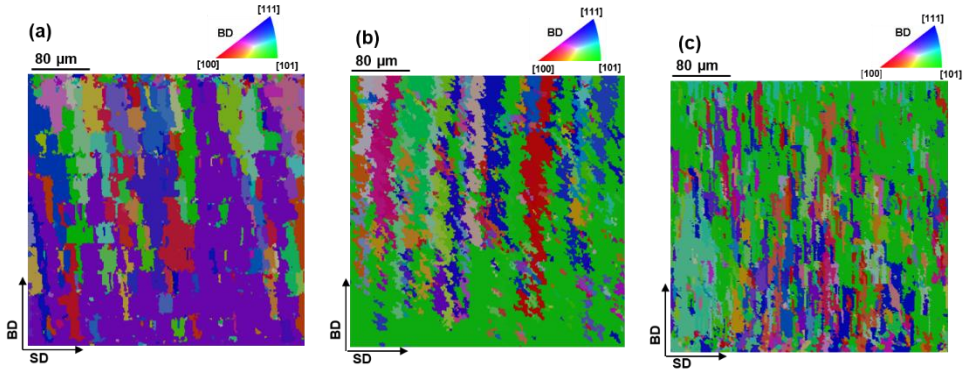


Figure 3.6 IPF map of the Y-Z section of RA-CA simulation with (a) only bulk, (b) only epitaxial, and (c) both bulk and epitaxial nucleation

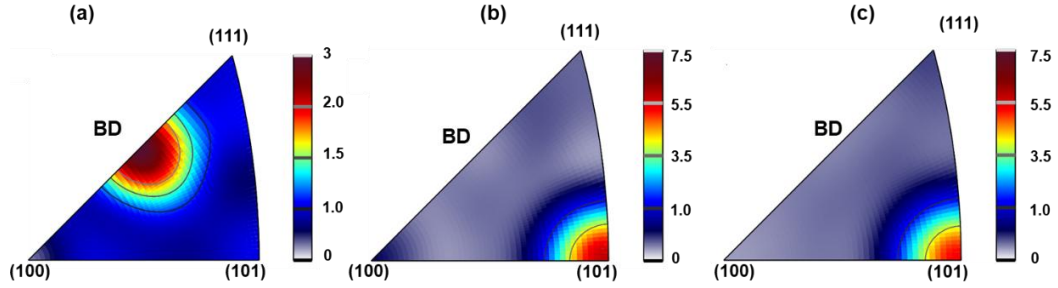


Figure 3.7 The IPF of Y-Z section of the RA-CA simulation with of RA-CA simulation with (a) only bulk, (b) only epitaxial, and (c) both bulk and epitaxial nucleation

3.2.3 Effect of growth kinetics

While the kinetic growth parameters α and β presented in Table 3.1 were calculated based on thermos-physical properties of X30Mn21 to provide a realistic baseline representation for growth kinetics, it is also important to note that these values change as per the materials. Therefore, to systematically evaluate the sensitivity of the developed RA-CA model to growth kinetics, additional simulations were performed with controlled variations in α and β in Equation 2.25. These parameters control the dependence of growth velocity on undercooling and thus directly affect the rate of solid–liquid interface progression. Three scenarios were simulated: (ii) reduced kinetics, (ii) baseline fitted coefficients (as calculated by equation (2.25), and (iii) increase kinetics. The values of respective growth kinetics coefficients namely: α and β are reported in Table 3.3. This parametric exploration allows understanding the effects of deviations from the nominal growth kinetic on the grain morphology and competitive growth during LPBF solidification.

The 3D grain morphologies and cross-sectional views obtained under different growth kinetics are presented in Figure 3.8 (a–i). It is clearly evident that varying the growth coefficients α and β has a significant impact on the development of grain size and morphology.

In the simulation with reduced kinetics (Figure 3.8 (a, d, g)), the grains are fine and highly fragmented, with a dense distribution of narrow columns extending along the build direction. The corresponding top surface view (Figure 3.8 (d)) displays a high density of small, equiaxed-like grains with limited lateral growth, resulting in a fine-grained appearance at the build surface. The YZ cross-section (Figure 3.8 (g)) further highlights the fine-scale columnar structures and frequent impingement between adjacent grains. Notably, in this case, small equiaxed grains are occasionally observed near the centerline region of the melt pool cross-section, reflecting the slower interface progression and increased opportunity for heterogeneous nucleation in the undercooled

melt. This behavior can be understood by considering the nucleation activation process described in Chapter 2. Specifically, each potential nucleation site is governed by a stochastic nucleation probability, modeled as a Gaussian function of local undercooling (Equation (2.3)), and an individual critical undercooling threshold that must be exceeded for activation (Equation (2.5)). Because the growth velocity in this scenario is low, the advancing solid–liquid interface progresses slowly, allowing more time for local undercooling to accumulate. As a result, a larger number of nucleation sites reach their critical undercooling and become active, producing a fine-grained microstructure with frequent impingement between growing grains.

In the baseline case (Figure 3.8 (b, e, h)), grains grow at moderate velocities. The faster interface progression reduces the time window during which undercooling can build up sufficiently to activate additional nucleation sites. As a result, the top surface (Figure 3.8 (e)) shows grains of intermediate size, which are more widely spaced compared to the reduced kinetics case. The cross-sectional view (Figure 3.8 (h)) demonstrates the development of continuous columnar grains extending along the build direction with less fragmentation. In this scenario, the occurrence of fine equiaxed grains along the centerline is notably diminished relative to the reduced kinetics simulation, as the more rapid growth restricts the activation of late nucleation events.

In the simulation with enhanced kinetics (Figure 3.8 (c, f, i)), the growth coefficients were increased by a factor of hundred, resulting in markedly faster solidification. Here, the earliest nucleated grains advance rapidly into the melt, consuming the liquid before many other potential nucleation sites can accumulate the undercooling necessary for activation as specified in Equation (2.5). Since the nucleation probability is highly sensitive to the local undercooling (Equation (2.3)), this rapid growth effectively suppresses the activation of most nucleation sites. As a result, the grain structure is dominated by a few large columnar grains that grow nearly unimpeded across the build direction, with a significant reduction in the overall number of grains. The top surface

morphology (Figure 3.8 (f)) shows large, widely spaced grains with minimal fragmentation. The YZ cross-section (Figure 3.8 (i)) is dominated by a few thick, continuous columnar grains spanning nearly the entire build height, and no fine equiaxed grains are observed along the centerline. This confirms that the high growth velocity effectively suppresses the conditions necessary for additional nucleation events, resulting in a coarse, directional microstructure.

These results demonstrate that even though the total number of predetermined nucleation sites is constant in the simulation setup, the kinetics of grain growth strongly influence which sites actually activate. Faster growth coefficients limit the time available for local undercooling to exceed the critical thresholds, reducing nucleation density and promoting coarse, continuous grains. Conversely, slower kinetics extend the period during which undercooling can reach activation conditions, resulting in finer and more fragmented microstructures.

Table 3.3 Growth coefficient values α and β used in the simulations to investigate the influence of solidification kinetics on microstructure evolution

	α	β
Simulation 1	9×10^{-8} m k^{-3}	3×10^{-5} m k^{-2}
Simulation 2	9×10^{-6} m k^{-3}	3×10^{-3} m k^{-2}
Simulation 3	9×10^{-4} m k^{-3}	3×10^{-1} m k^{-2}

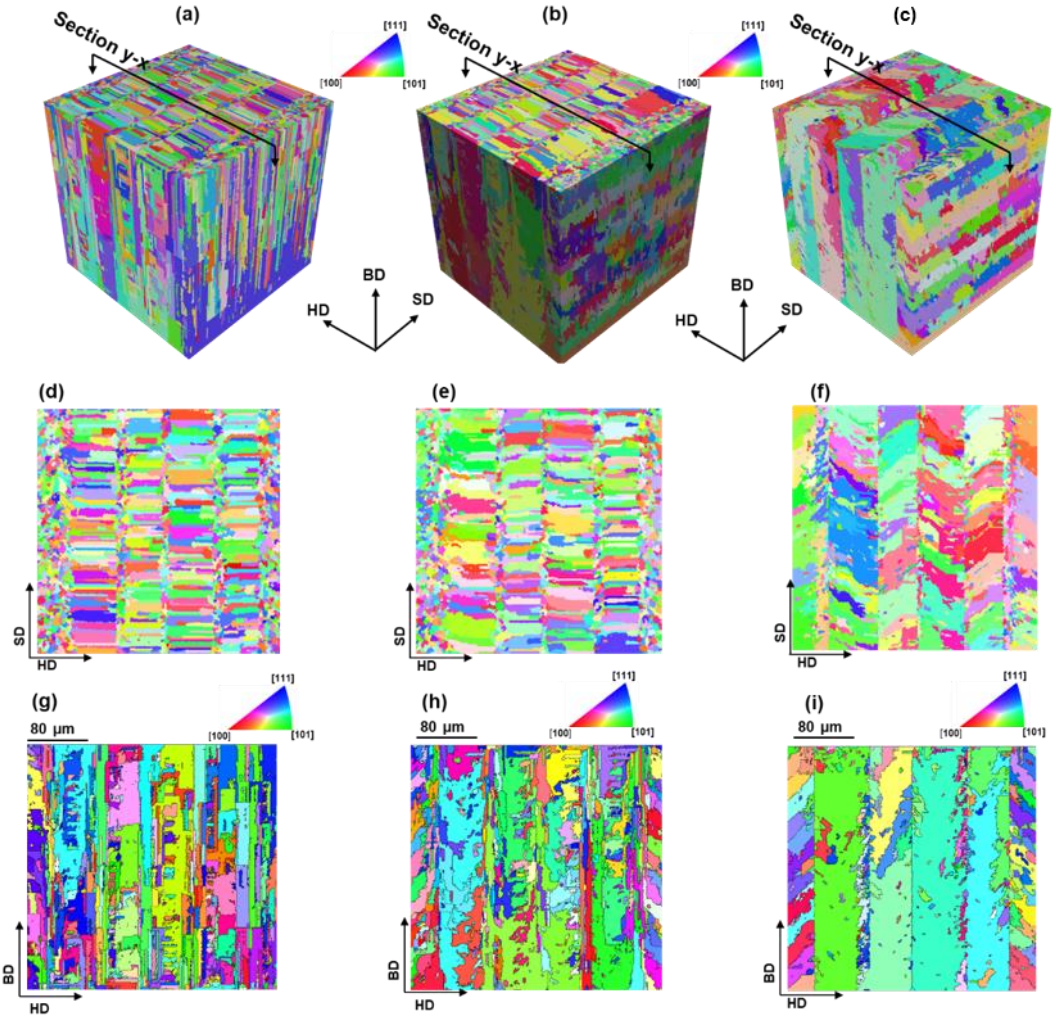


Figure 3.8 Simulated 3D grain morphologies and cross-sectional views illustrating the influence of solidification kinetics on microstructure evolution. (a–c) 3D grain structures obtained using (a) reduced growth kinetics(simulation 1), (b) baseline growth kinetics fitted from Equation 2.25 (simulation 2), and (c) enhanced growth kinetics (simulation 3). (d–f) Top surface views corresponding to each scenario, showing the distribution and size of grains at the build surface. (g–i) YZ cross-sectional views highlighting the columnar growth morphology and extent of grain impingement.

3.3 Conclusion

The simulation results discussed in this chapter confirm that the developed RA-CA framework behaves in a physically consistent manner. Trends such as the formation of fine, fragmented grains under reduced growth kinetics, the development of coarse columnar grains under enhanced kinetics, and the clear sensitivity of grain size to the

growth coefficients α and β are consistent with theoretical behaviors discussed in chapter 2. Furthermore, observations like the grain structure in bulk nucleation, the formation of small equiaxed grains near the melt pool centerline, and the dominant <101> texture along the build direction align well with features commonly reported in experimental studies. This demonstrates that the new framework, even after incorporating remelting handling, retains its ability to capture key grain evolution phenomena in LPBF.

Importantly, the parametric insights gained in this chapter provide technical guidance for the experimental validation in Chapter 4. The sensitivity of grain size distribution to the growth law coefficients highlights the role of material-dependent kinetics in governing refinement. Since, these coefficients being derived from alloy thermos-physical properties; it offers a physically consistent basis for comparison with experimental results. Likewise, the contrasting morphologies predicted under bulk and epitaxial nucleation define the simulation conditions relevant for benchmarking against experimentally observed grain structures. These findings provide a strong foundation for the experimental validation presented in Chapter 4, where the RA-CA predictions are compared against EBSD data from X30Mn21 LPBF samples.

Chapter 4

Microstructure development in a LPBF-processed Steel

4.1 Introduction

The credibility of computational microstructure models depends fundamentally on their alignment with experimental observations. In this chapter, the accuracy of the developed RA-CA model by comparing its simulated grain structures with the experiments. To do this, experiments were carried out and the specimen were produced using LPBF. The resulting microstructure was then analysed using electron backscatter diffraction (EBSD). The specimen for this validation was prepared at the RWTH Aachen University Steel Institute, Germany. Furthermore, the developed RA-CA model was used to simulate the microstructure under the same process parameters using two different spatial resolutions to assess the model's sensitivity to cell size. The test material for this assessment was the same as that is discussed in section 3 namely a single-phase austenitic (FCC) advanced high strength steel (AHSS), namely X30Mn21. This chapter presents a structured comparison between simulation and experiment, focusing on both qualitative features e.g., grain structure, texture orientation and quantitative metrics e.g., grain size distribution, aspect ratio, texture intensity.

4.2 Experimental Procedure

To validate the CA model, experimental data was collected from additively manufactured specimens of X30Mn21 austenitic high-manganese steel. This alloy was

chosen because it shows a clear solidification structure and texture, making it a good candidate for comparing with simulation results. The average particle size of X3Mn21 alloy was 14.94 µm. The chemical composition of metallic powder is reported in Table 4.2. The cubical specimen of 10mm X 10mm X 10mm was fabricated using an Aconity Mini L-PBF machine (Aconity-3D GmbH, Germany). The built was carried out in an inert argon atmosphere. A set of fixed process parameters was used to ensure repeatability. The specifics of the experiments, including laser power, scan speed, layer thickness, and hatch distances (HD), are outlined Table 4.1. The process parameters, including the layer thickness, laser power, and hatch distance, were selected based on available literature for LPBF processing of austenitic steels[119,120]. These parameters promote sufficient melt pool overlap and layer bonding, thereby contributing to dense parts and influencing the development of the resulting grain structure. Bi-directional laser scan strategy was used for building the specimen. The printed specimens were cut along the build direction (BD) and polished for microstructure analysis. Electron backscatter diffraction (EBSD) was used to study the grain morphology and crystallographic orientation. EBSD measurements were performed on a GeminiSEM field emission gun (Carl Zeiss AG, Germany). The EBSD data was analysed using the MTEX toolbox within MATLAB [97] to visualize the orientation maps, calculate pole figures and grain size and aspect ratios. This experimental dataset serves as the benchmark against which the simulation results will be compared in the following sections.

Table 4.1 LPBF process parameter

Parameter	Value	Unit
Laser Power	120	W
Spot diameter	80	µm
Hatch spacing	70	µm
Layer thickness	30	µm
Scan speed	750	mm/sec

Table 4.2 Chemical compositions of X30Mn21 metal powder

	Fe	Mn	C	Al	Cr	Ni	O
Metal powder	Base	21.00 %	0.33 %	0.03 %	0.15 %	0.08 %	0.10 %

4.2.1 Microstructural Characterization of LPBF-Processed X30Mn21

The microstructure of the specimen obtained experimentally is presented in Figure 4.1.The EBSD mapping in Figure 4.1 exhibits a distinct lamellar microstructure where it can be seen that there are alternating grains with <100> and <101> crystallographic orientation with respect to the build direction. This kind of alternating grain structure is referred to as "crystallographic lamellar microstructure" (CLM) [121]. For texture analysis, the inverse pole figure (IPF) map and respective pole figures (PF) are reported in Figure 4.2 and Figure 4.3 respectively. For quantitative metrics, the grain size and aspect ratio distribution is presented in Figure 4.4 and Figure 4.5 respectively.

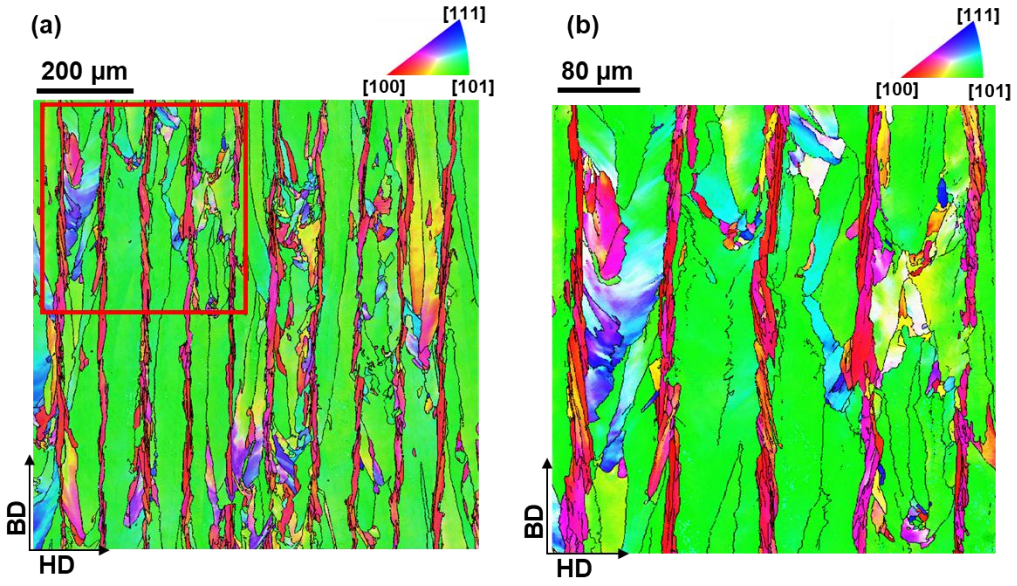


Figure 4.1 (a) EBSD inverse pole figure (IPF) map of the X30Mn21 specimen, with BD as the reference axis, (b) a magnified view, highlighting alternating <101> and <100> orientations and finer sub grain features

4.2.1.1 Grain Morphology and Crystallographic Orientation

From the EBSD map in Figure 4.1, most grains appear elongated along the build direction. <101> grains (which appear in green in the IPF coloring) dominate the areas outside the centerline of the melt pool. On the other hand, the grains at the melt pool centerline are mostly <100> oriented (red coloring). This difference in orientation is observed because the heat flow at the centerline is mainly vertical, which led to the grains to be oriented towards <100> [93]. Nearby grains are solidified under slightly tilted thermal gradients, which leads to growth in the <101> direction.

In section 1.3.5.4, it was discussed that the texture in LPBF mostly comes from the solidification texture mechanism, where the preferred growth direction of the crystal tends to align along with the heat flow direction. Since X30Mn21 has an FCC lattice structure, the preferred growth direction is the <100> direction and at the centerline of the melt pool, the thermal gradient is mostly vertical ,along the build direction, so the grains at the centerline tend to align their <100> direction with the thermal gradient which is along the build direction. Nevertheless, farther away from the centerline, the thermal gradient becomes tilted instead of straight up. Because of this tilt, which can sometimes be up to 25° from the build direction [119], grains in these areas grow along the <101> direction instead. This change in growth direction across the melt pool is what leads to the formation of what's called a crystallographic lamellar microstructure (CLM), where alternating grains of <100> and <101> are visible.

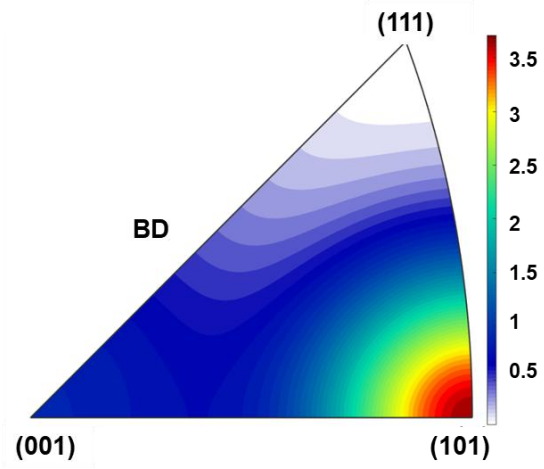


Figure 4.2 The IPF for X30Mn21 fabricated with LPBF

The IPF in Figure 4.2 shows that most of the grains are oriented near the <101> corner (BD as the projection axis). This confirms a strong <101> texture, especially in regions outside the melt pool centerline. There is also some spread towards <100> orientations, which matches the <100> oriented grains seen at the centerline in the IPF map. This is further confirmed by the <100> pole figure showing strong intensity along the build direction. The <101> pole figure shows a higher intensity near the BD, which fits with tilted thermal gradients leading to a <101> texture in surrounding grains. The <111> pole figure shows very low intensity parallel to BD, so the BD || <111> orientation is not predominant here. Altogether, these plots confirm the formation of a CLM structure with alternating <100> and <101> grains, as discussed earlier.

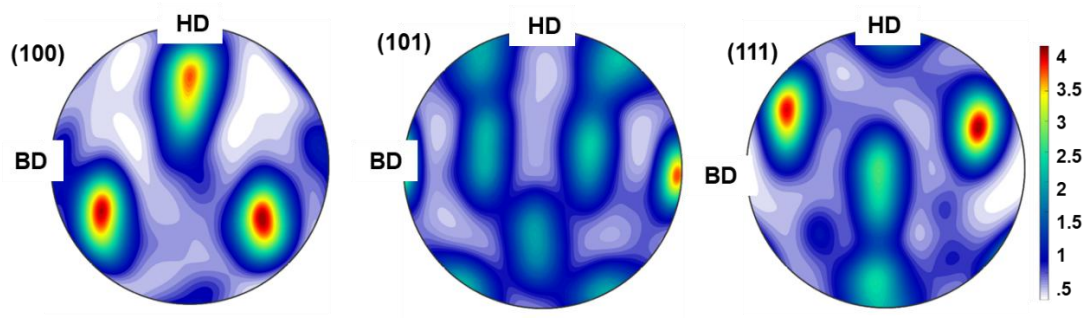


Figure 4.3 Pole figures <100>, <101> and, <111> crystallographic direction for specimen fabricated with LPBF

4.2.1.2 Grain Size and Aspect Ratio Distributions

The grain size and aspect ratio distributions are shown in Figure 4.4 and, Figure 4.5, respectively. Grain size was calculated using equivalent circle diameter and the average grain size was found to be 11.81 µm (±18.49 µm), as calculated using number weighted averaging technique. The trend in the histogram shows that as the grain size increases, the number of grains in that range decreases, which is typically observed in LPBF. The aspect ratio distribution also shows a similar pattern, where most grains fall in the lower aspect ratio bins. More than 80% of the grains have a size below 20 µm and an aspect ratio lower than 7. This reflects rapid solidification near the melt pool centerline, where conditions promote the formation of smaller and equiaxed grains. This pattern matches the IPF map (please refer Figure 4.1), where small, equiaxed grains can be seen near the melt pool centerline and elongated grains appear along the build direction. The distribution observed here is consistent with what is reported in LPBF literature and reflects how the solidification behavior and thermal gradient shape the final grain morphology [112].

These experimental observations, that is the mix of <100> and <101> textures, the fine grain formation near the centerline, and elongated grains near the boundaries, will be used as reference to check the accuracy of developed RA-CA.

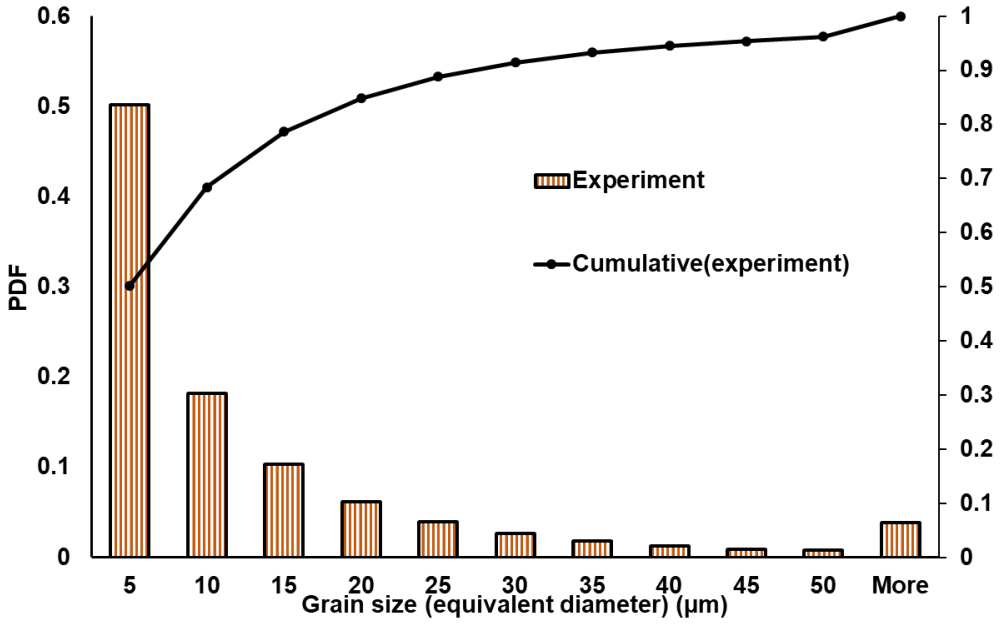


Figure 4.4 Histogram of grain size distribution obtained from experiments

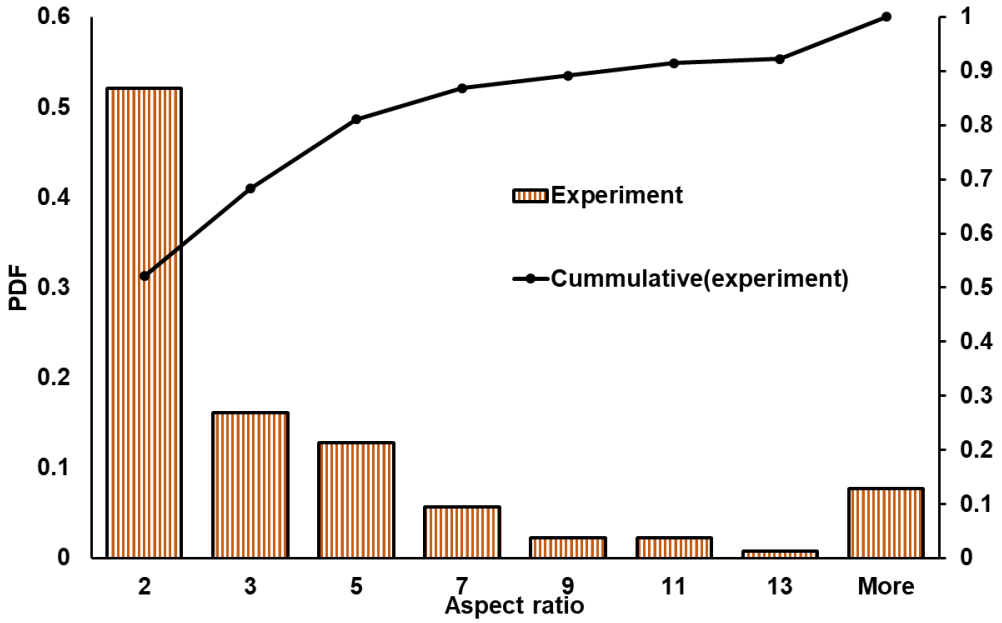


Figure 4.5 Histogram of grain aspect ratio distribution obtained from experiments

4.3 RA-CA Simulation Analysis

Simulations were performed to validate the developed RA-CA model by predicting morphology, grain size, and crystallographic texture of X30Mn21 for certain LPBF process parameters. The process parameters such as laser power, scan speed, hatch spacing, and layer thickness were taken the same as the experiment (please refer Table 4.1 LPBF process parameter). Simulations were performed using two different CA cell sizes 0.8 μm and 2 μm to study the effect of spatial resolution of the automaton on the accuracy. 3D grain structures were rendered in Paraview, and the MTEX toolbox in MATLAB was used for texture analysis same as that of experimental analysis. Additionally, the efficiency of the implemented parallelization strategy in the RA-CA model was evaluated.

4.3.1 CA Simulation Setup

The remelting-aware CA model (RA-CA) was coupled with the temperature field generated during the LPBF process. This was done in accordance with section 2.3. The temperature field for the LPBF process was simulated using ABAQUS using the process parameters given in Table 4.1. The setup for generating the thermal field was discussed in previous section (please refer section 3). The RA-CA model parameters are listed in Table 4.3. Based on the discussion in section 3, for this study, both bulk and epitaxial nucleation were enabled to reflect realistic LPBF solidification conditions. The selection of the nuclei site and assignment of crystallographic orientation followed the methodology described in section 2.3 and 2.4.1 respectively. It has been reported that the typical values for mean nucleation undercooling temperatures range between 1°C and 5°C for both nucleation types [12,100] for both epitaxial and bulk nucleation with standard deviations often less than 1^{o} C for heterogeneous nucleation [23]. The parameters are chosen based on these considerations [12,22,23,100]. The nucleation densities for bulk ($\emptyset_v$) and epitaxial ($\emptyset_s$)sites were calculated using the method described by Yian et al. [22], where the number of nuclei is estimated based on experimental grain

size data. For bulk nucleation, the grain count was obtained by dividing the simulation domain volume by the volume of spherical grains, using the average experimentally observed grain diameter. For surface nucleation, a similar approach was applied using 2D grain size data to estimate nuclei per unit area. The values used here were adapted from Patrick et al. [119], who studied X30Mn21 processed under similar LPBF parameters. All temperature-dependent material properties and inputs for X30Mn21 were retained as described earlier (please refer to Table 3.1). Furthermore, the growth kinetics followed the LGK model, using the same α and β coefficients determined in Section 3.

Table 4.3 RA-CA model parameters

Parameters	Value
$\emptyset_{\mathbf{v}}$ (mm^{-3})	3.9×10^4
$\emptyset_{\mathbf{s}}$ (mm^{-2})	1.25×10^4
mean nucleation undercooling for bulk nucleation distribution $(\Delta T_m)_b$ (°C)	5
mean nucleation undercooling for surface nucleation distribution $(\Delta T_m)_s$ (°C)	1
standard deviation for bulk nucleation distribution $(\Delta T_\sigma)_b$ (°C)	0.2
standard deviation for surface nucleation distribution $(\Delta T_\sigma)_s$ (°C)	0.2
growth coefficients α	9×10^{-6}
growth coefficients β	3×10^{-3}

4.3.2 Microstructural Characterization of Simulated X30Mn21

The simulated grain structure obtained from the RA-CA model is shown in Figure Figure 4.6, rendered using Paraview. The figure shows the 3D morphology of the grains in the simulated domain. For better clarity, 2D grain maps were extracted from the same volume and are reported in Figure 4.7 for two different CA resolutions. Figure 4.8 and Figure 4.9 show the inverse pole figure (IPF) map and pole figures (PF), respectively, which were used to evaluate the crystallographic texture developed during the simulation. The corresponding grain size distribution and aspect ratio distribution from the simulations are presented in Figure 4.10 and Figure 4.11.

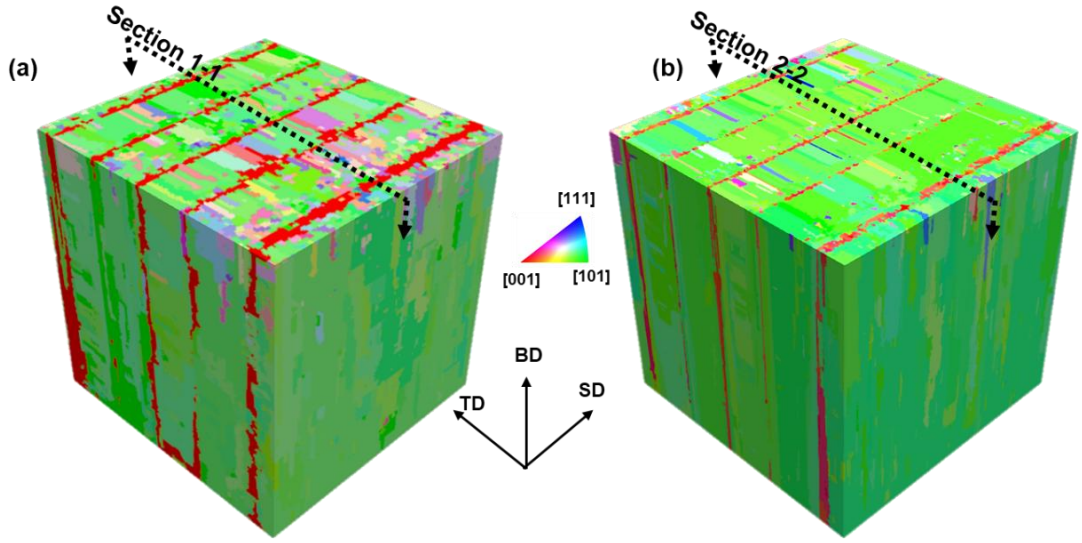


Figure 4.6 Isometric view of the simulated grain structure at different CA cell sizes: (a) d_{cell}= 2 µm and (b) d_{cell} = 0.8 µm.

4.3.2.1 Grain Morphology and Crystallographic Orientation

The grain simulated grain structure (along section 1-1 and section 2-2 (please refer Figure 4.6)) obtained from the RA-CA model for two different cell sizes is reported in Figure 4.7 Figure. Figure 4.7 (a) corresponds to the 2 µm resolution whereas Figure

4.7 (b) to the finer 0.8 µm cell size. In both the simulations, the grains are clearly elongated and seem to grow along the build direction. However, the simulation with the finer cell size shows more well-defined and narrower grains, especially near the centerline. This improvement could be attributed to the fact that a smaller cell size allows the model to resolve more local features at grain boundaries and more accurately represent variations in local grain morphology.

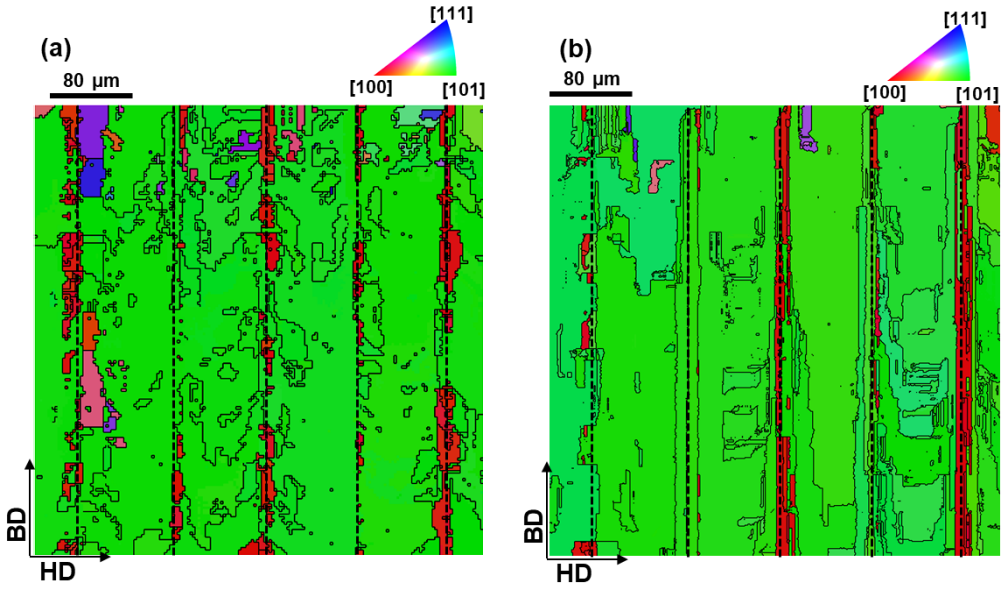


Figure 4.7 IPF map of the X30Mn21 sample obtained with: (a) RA-CA simulation with CA cell size of d d_{cell}= 2 µm; (b) RA-CA simulation with CA cell size of d_{cell}= 0.8 µm

The corresponding IPFs for both simulations are reported in Figure 4.8. The orientation density in both is mainly concentrated near the <101> corner, which confirms a strong <101> fiber texture along the build direction. The plot for 0.8 µm also shows a slightly sharper texture peak, meaning that the orientation alignment is better captured with the finer resolution.

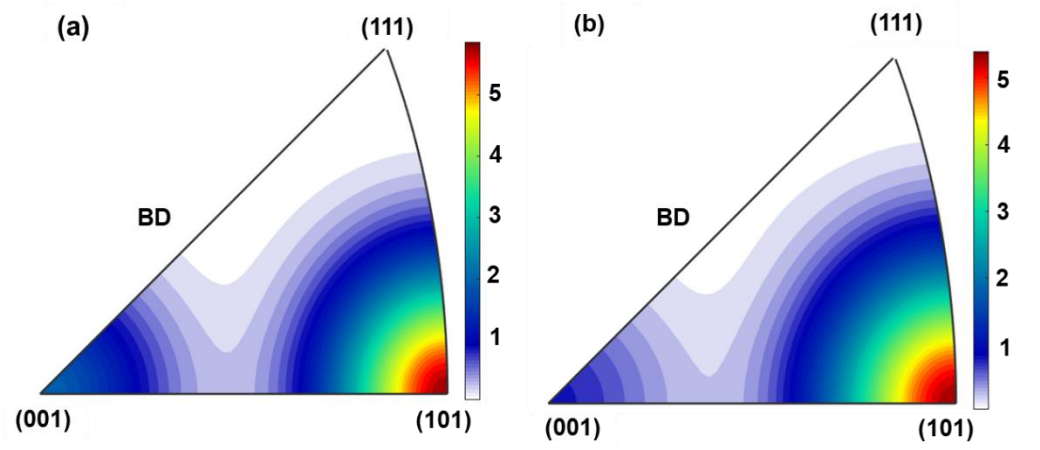


Figure 4.8 The IPF for X30Mn21 (a) RA-CA simulation with CA cell size of d d_{cell}= 2 µm; (b) CA simulation with CA cell size of d_{cell}= 0.8

The pole figures reported in Figure 4.9 also support the same texture trend. The <101> pole figure shows strong intensity along the BD for both simulations, which matches what is seen in the IPFs. The <100> pole figure shows moderate intensity in both cases, and the <111> pole figure shows low intensity across the map. So overall, the simulation can reproduce the typical LPBF texture with dominant <101> alignment and some <100> orientation, just like what is usually seen in FCC alloys under strong thermal gradients.

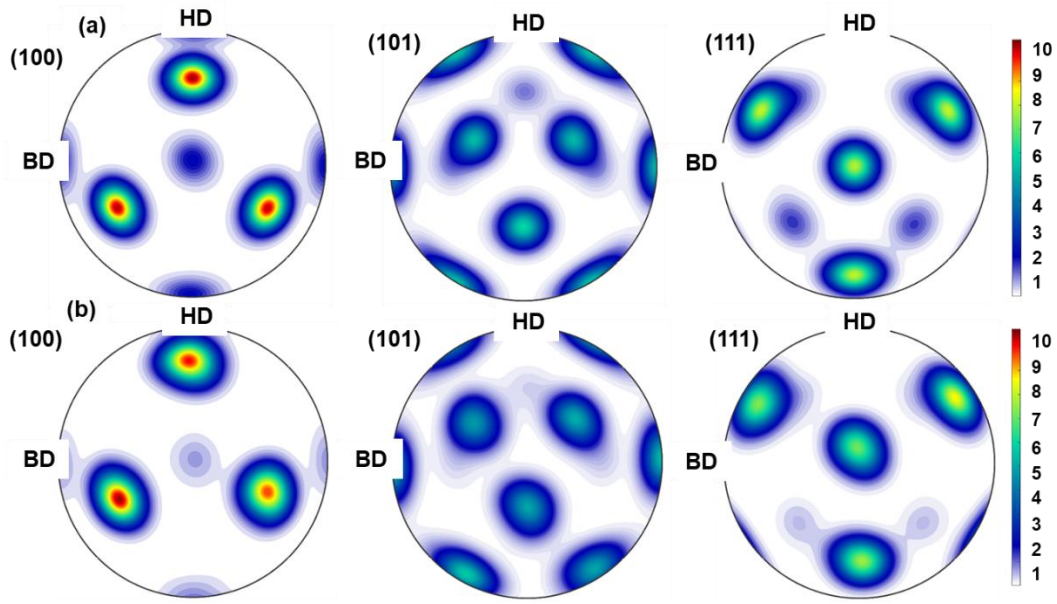


Figure 4.9 Pole figures <100>, <101> and, <111> crystallographic direction for: (a) CA simulation with CA cell size of d_{cell}= 2 µm; (b) CA simulation with CA cell size of d_{cell}= 0.8

4.3.2.2 Grain Size and Aspect Ratio Distribution

The grain size distribution obtained from the simulations is reported in Figure 4.10. The average equivalent spherical diameter for the simulation with CA cell size of 0.8 µm and for 2 µm was calculated as 10.11 µm and 12.65 µm respectively. As seen in the figure, the simulation with finer resolution predicts a greater number of grains with size less than 5 µm, which the 2 µm simulation fails to capture. The cumulative frequency plot also confirms this, showing a sharper rise for the finer cell resolution. This could be attributed to the fact that with a smaller CA cell size, the model is able to track finer grains better and resolve more detail in the microstructure.

Furthermore, it could be seen that more than 80% of the grains in both simulations are smaller than 20 µm, which is consistent with LPBF solidification trends. However, it is also seen that the 2 µm simulation slightly overestimates the average grain size, mainly due to missing the smallest grains that are typically present near the melt

pool centerline. This again highlights the role of CA cell resolution in predicting accurate grain features.

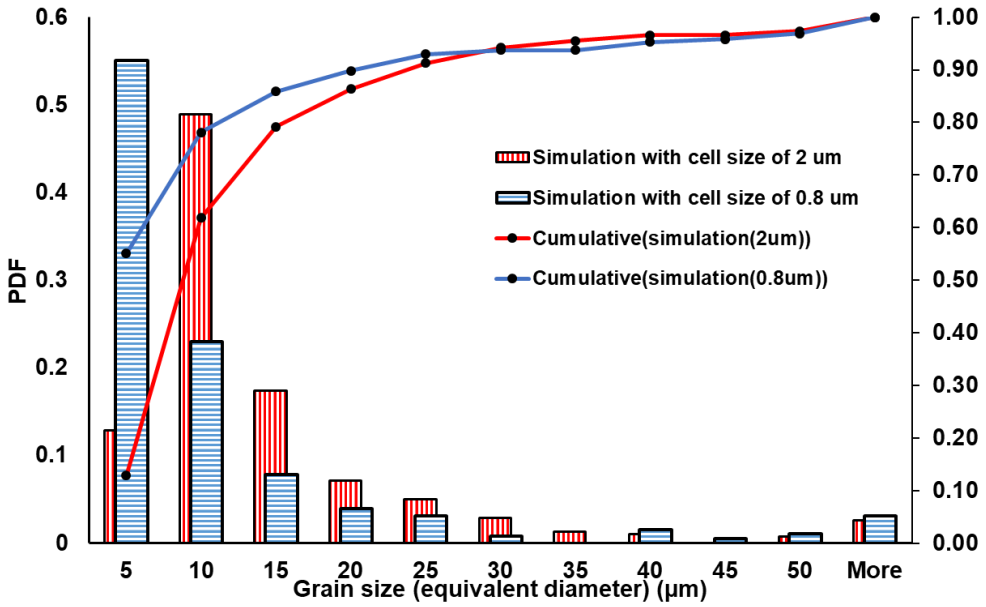


Figure 4.10 Histogram of grain size distribution obtained from simulation

The aspect ratio distribution from the simulations is shown in Figure 4.11. Similar to grain size, the finer CA resolution captures slightly more variation in aspect ratio bins, especially in the lower ranges. Nevertheless, the overall trend remains the same for both cases most grains have aspect ratios below 7, which matches the expected LPBF morphology. Grains with aspect ratios between 2 and 5 are the most frequent, showing the presence of elongated grains growing in the direction of the thermal gradient. The simulation with 0.8 μm cell size picks up more detail in shape boundaries, but even the 2 μm result manages to follow the trend well.

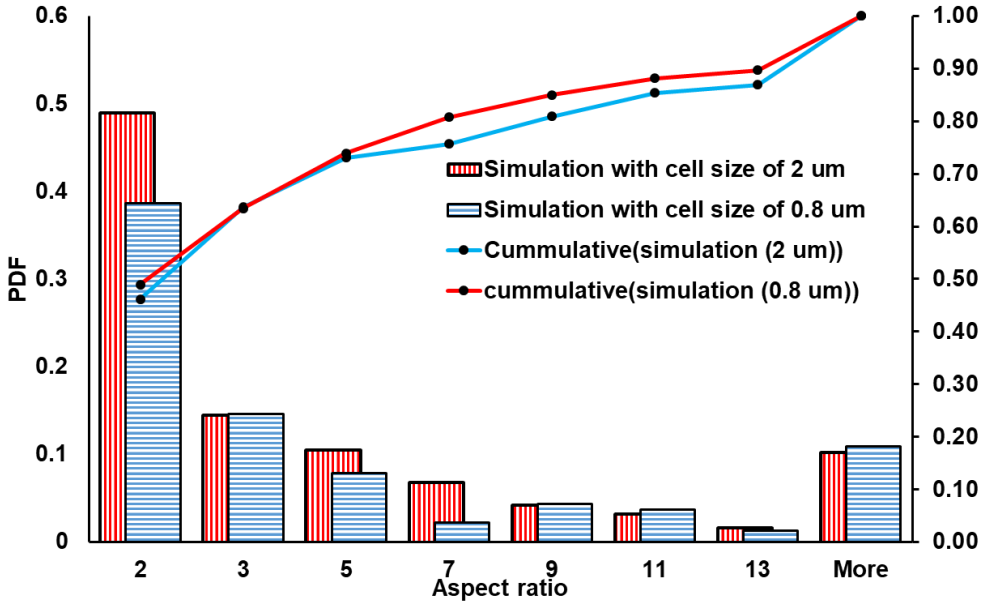


Figure 4.11 Histogram of grain aspect ratio distribution obtained from simulation

4.3.3 Comparison between Simulations and Experiments

In this section the results obtained from the RA-CA simulations with the experimental data are compared to evaluate the accuracy of the model regarding the microstructural features. The comparison includes grain morphology, grain size, aspect ratio, spatial arrangement using PCF, and crystallographic texture by plotting the subtraction of the ODF for experiments and simulations.

4.3.4 Morphology Comparison and Statistical Comparison

By comparing the simulated grain morphology reported in Figure 4.7 and experimentally observed structure reported in Figure 4.1, it is quite evident that in both cases, elongated grains were generated and aligned with the build direction, forming a typical columnar microstructure. The CA simulation was able to reproduce this trend with both 0.8 µm and 2 µm cell sizes. Along the melt pool centerline, the presence of equiaxed grains were also captured, though finer details were better resolved with the smaller cell size.

The grain size and aspect ratio distributions from both experiment and simulation are shown in Figure 4.4, Figure 4.5, Figure 4.10 and Figure 4.11. More than 80% of the grains from the simulation have an equivalent diameter below 20 µm, which matches well with experimental findings. The simulation with a cell size of 0.8 µm predicted an average grain size of 10.68 µm, while the one with 2 µm resolution gave 12.46 µm. The experimental average grain size was 12.22 µm. The increase of the CA cell size from 0.8 µm to 2 µm led to an approx. 15% increase in predicted grain size. This increase is expected because a larger cell size reduces spatial resolution, which can lead to missing the fine grains formed during rapid solidification. The experimental grain size distribution also shows that 50% of grains are smaller than or equal to 5 µm. The simulation with 0.8 µm resolution captured this fine-grain population, while the 2 µm simulation failed to do so. However, for larger grain sizes, the trend was similar across all cases.

In terms of aspect ratio, both simulations agreed faithfully with the simulations. Most grains evinced an aspect ratio below 7. The distribution in Figure 4.11 shows that grains with aspect ratios between 2 and 5 were most frequent; matching what is expected in LPBF due to columnar growth along the build direction. The simulation with 0.8 µm resolution captured more shape variation, but the overall trend remained consistent even for the 2 µm case.

To compare the spatial arrangement of grains, the pair correlation function (PCF) was plotted in Figure 4.12. The PCF is a statistical measure widely used to describe the spatial distribution of points or objects within a microstructure. The PCF quantifies the probability of finding the center of another grain at a given distance *r* from a reference grain, normalized by the probability expected for a random distribution[122]. This provides a measure of the spatial arrangement and correlation of grains within the microstructure [123].

The experimental and simulated curves show a very similar trend, especially for the 0.8 µm simulation. A steep initial drop and low correlation after 0.05 mm indicates a packed, irregular grain structure. The 2µm simulation deviated slightly, likely due to underestimation of fine grains. Still, the close agreement between the experimental PCF and 0.8 µm simulation confirms that the model is able to capture spatial grain features effectively.

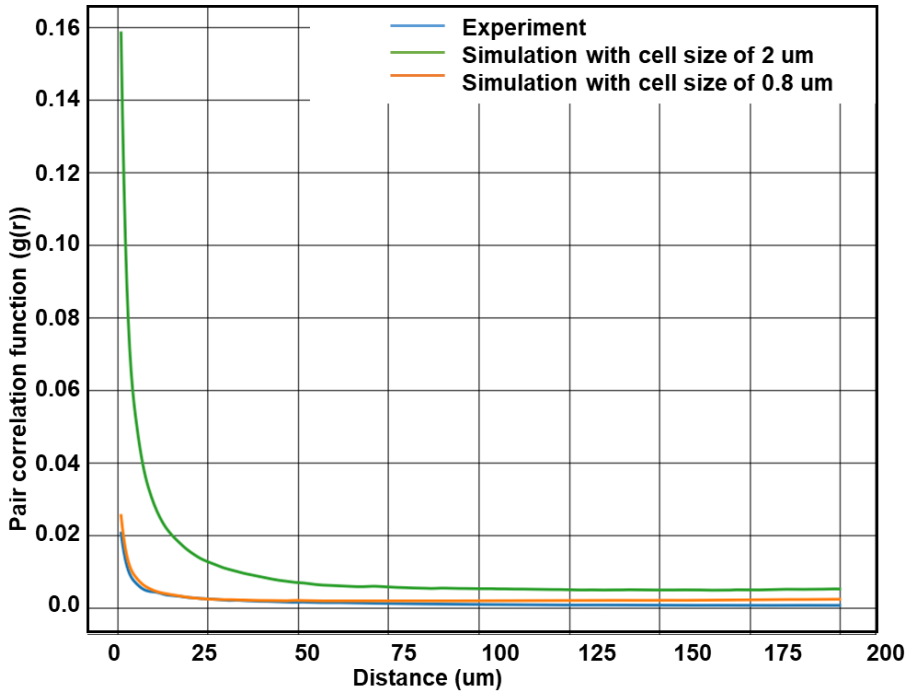


Figure 4.12 Pair Correlation Functions (PCF) of microstructures obtained by simulation and experiment.

4.3.5 Texture and Orientation Comparison

The texture from both simulations and experiments was compared using IPF and pole figures. In both, a strong <101> texture was observed along the build direction. RA-CA model, with both cell sizes, was able to predict this trend well. This kind of texture is commonly seen in LPBF due to inclined thermal gradients which lead grains to align their <101> direction with the build direction instead of <100>. The IPF triangle plots and pole

figures reported in Figure 4.2 and Figure 4.8 confirm this behavior for both simulation and experiment.

To better assess the agreement, the pole figures of the simulation and experiment were subtracted, and differential pole figures were generated using Mtex [97]. These are reported in Figure 4.13. From these images, it can be seen that the main <101> texture components are consistent in both simulations and experiments. However, there are some small differences, especially in the <100> and <111> pole figures. The simulation with 2 µm cell size shows slightly more variation and a few offset spots, while the 0.8 µm simulation matches more closely. This confirms that finer CA resolution leads to better prediction of the texture pattern.

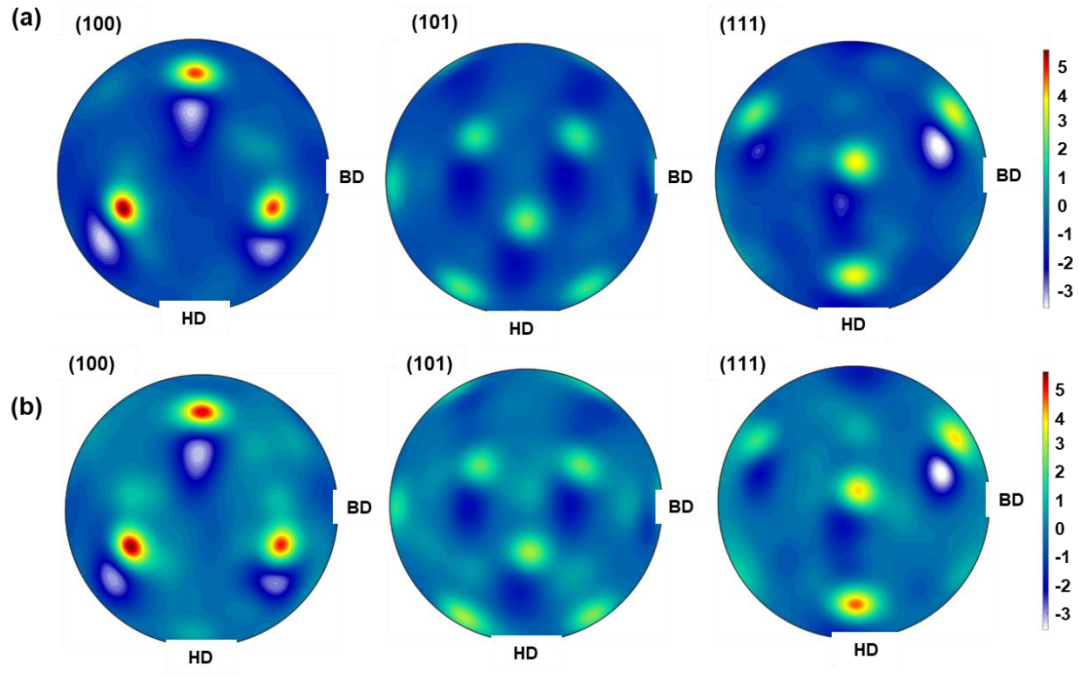


Figure 4.13 Pole figures subtraction of: (a)RA-CA simulation with cell size of 2 µm and experiment; (b RA-CA simulation with cell size of 0.8um and experiment

Some weak random components were still present in the simulated pole figures, which are not seen in the experiments. These random components most likely originate from bulk-nucleated grains in the simulation that were assigned random orientations. If such

grains are aligned so that they experience a strong driving force during solidification, they may still grow even if they are not aligned with the thermal gradient. However, since the intensity of these off <101> orientations is low, it shows that these cases are rare.

Overall, the CA simulation was able to reproduce the dominant <101> texture well. The use of a finer cell size improved the alignment with experimental pole figures, although some random texture components still appeared due to how nucleation was defined in the model.

4.4 Efficiency of the Cellular Automaton model and simulation setup

To evaluate the effectiveness of parallelization on the presented CA model, a CA simulation using CA cell size of 0.8 µm was performed with varying number of computational processes. The process and simulation parameters are detailed in Table 4.1 and Table 4.3, respectively. With a total of 125×10^6 CA cells, the computational time, and the parallel efficiency with respect to the number of processors were studied and are presented in Figure 4.14 . A significant increase in simulation speed of up to 40% was observed by doubling the number of processors from 1 to 2. However, further increase in the number of processors did not result in the proportional simulation speed. This leads to the drop in the efficiency of each processor, as indicated in Figure 4.14. Specifically, efficiency dropped from 80% with 2 processors to 50% with 6 processors. This decline of efficiency could be attributed to the spatial division within the simulation domain among the processors, which potentially lead to load imbalances within the processors. Each processor has its own domain and is activated only when the cells within it get activated. However, when it comes to LPBF, not all the domains are activated simultaneously. They wait for their respective melting times. Consequently, processors may idly wait during these intervals, leading to uneven workload distribution. Some processors may carry heavier loads than others at certain points, resulting in suboptimal utilization of resources and decreased overall efficiency [16]. Moreover, the

presented parallelized RA-CA model has an innovative approach to manage the remelting in LPBF, which aims to reduce the computation load. The CA model is effective in reducing the simulation time. Considering the time of simulation and number of CA cells, simulation time per CA cell comes out to be 1.04 µmin which is about 30% less than that reported in literature under similar conditions [16]. This increment in performance is crucial for simulating the microstructure at the part scale, where millions or even billions of additional CA cells would be involved. Moreover, it is worth noting that the performance of the model may be further improved depending on specific parameters, such as an increase in remelting volume. This suggests promising potential of the presented model for even greater efficiency enhancements under varying conditions.

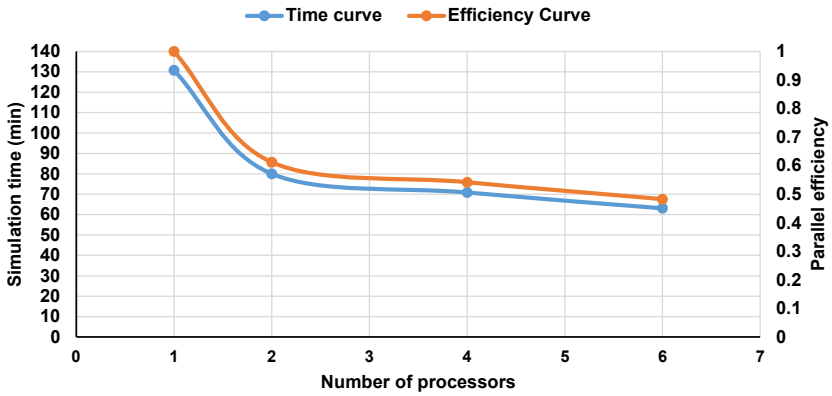


Figure 4.14 Computational time and the efficiency of parallelization of the 3D CA model.

4.5 Discrepancies between Simulation and Experiment

Although the simulations reproduce the dominant morphological and textural features observed in EBSD, certain discrepancies remain that clarify the limits of the current framework. First, the model does not fully capture the crystallographic lamellar microstructure (CLM), particularly the <100>-oriented bands frequently observed along the melt-pool centerline. In the RA-CA implementation, nuclei are oriented along the local thermal gradient, which should in principle favor <100> alignment near the centerline; however, bulk nucleation sites are placed stochastically in space and time. This random placement does not always coincide with the locations where periodic

lamellar arrangements form experimentally under weak/perturbed gradients, leading to incomplete reproduction of CLM-like patterns. Second, resolution effects are evident, the 0.8 µm grid resolves the sub 5 µm grain population seen in EBSD, whereas the 2 µm grid underrepresents these grains and slightly shifts the average size upward. Together, these observations indicate that nucleation statistics (placement) and grid resolution are the primary sources of mismatch.

4.6 Conclusions

This section has evaluated the ability of the developed Remelting-Aware Cellular Automaton (RA-CA) model to predict the microstructure of X30Mn21 steel processed by LPBF. The model was coupled with thermal profile generated with FE method and then simulated microstructural predictions were compared with the one obtained with the experiments. The results show that the RA-CA model can capture the key features of LPBF microstructures. The predicted grain morphology shows a strong columnar structure growing along the build direction, consistent with what is observed in experiments. The grain size distribution and aspect ratio trends were also reproduced well. In particular, simulations with a finer CA cell size (0.8 µm) were able to capture the fine grains and sharper boundaries more accurately, while the 2 µm simulations slightly overestimated grain size due to resolution limitations.

The model also predicted the dominant <101> texture observed in the experimental specimen. This texture is typical for LPBF processes where the thermal gradient is inclined, and <101> tends to align with the build direction. However, the model did not fully capture the crystallographic lamellar microstructure (CLM), especially the <100>oriented grains along the centerline. This discrepancy can be linked to the phenomenological treatment of nucleation. Since bulk nucleation is assigned randomly in the model, it may not always produce the correct orientation relationships observed experimentally, particularly in regions where thermal gradients are complex or weak.

Overall, the RA-CA model shows good predictive capability in simulating the microstructure of LPBF-processed X30Mn21. The findings support the applicability of the model for capturing solidification-driven morphology and texture features. Given the fact that this model is designed to reject redundant remelting-related events, it is at least 30% faster than conventional CA models. This speed-up allows for rapid prediction of microstructure and makes the framework useful for generating a first approximation of grain structure in LPBF simulations. In the next chapter, this framework will be tested further under different processing conditions to evaluate its broader applicability.

Chapter 5

Effect of Preheating on Microstructure and Property Relationships in LPBF-Processed X30Mn21

5.1 Introduction

As discussed in chapter 1, the LPBF process is extensively used for processing new materials and complex design. However, rapid cooling and high thermal gradients associated with LPBF lead to formation of distinct microstructure. These differences also lead to variations in mechanical properties. Preheating the build platform is often considered as an effective strategy to mitigate the high thermal gradients. It can help improve solidification stability and influence grain morphology, texture, and possibly mechanical behavior [124,125] . Preheating of the build platform also helps in reducing thermal stresses and improve mechanical properties. Such a technique is also commonly utilized in in various application to even reduce the porosity defects [126]

This chapter presents a computational investigation into the effect of preheating on the grain structures of X30Mn21 austenitic advanced high-strength steel (AHSS) processed via LPBF. The grain structure under different preheat conditions was simulated using the RA-CA model developed in earlier chapters. The model was coupled with thermal fields that account for the preheat temperatures. The goal was not only to observe how the preheating affects the microstructure, but also to explore if this simulated output can be used to build a structure–property (P–S–P) linkages. To this aim, in addition to the microstructural simulations, the mechanical behavior corresponding to the different grain structures was also evaluated. The mechanical response, including

stress–strain prediction, was obtained using CP-FEM (Crystal Plasticity Finite Element Method). It is important to mention that the CP-FEM simulations were carried out by J. Chen [127] in the framework of his doctoral research [128]. The results from the CP-FEM simulations were used here to establish the P-S-P linkages and to assess the accuracy of the predictions.

5.2 RA-CA Simulation Setup

The grain structure of X30Mn21 at four different preheating temperatures: 200°C, 400°C, 600°C, and 800°C was simulated using the RA-CA model developed in the previous chapter. The LPBF process parameters such as laser power, scan speed, hatch spacing, and layer thickness are reported in Table 5.3. The scan pattern used for thermal simulation is presented in Figure 5.2. The temperature fields for each preheat condition were generated using the ABAQUS simulation explained in section 3. The growth kinetics coefficients and β also remained unchanged and was based on the undercooling-based polynomial used earlier. The nucleation density values were selected based on the literature as discussed in chapter 4 (please refer section 4.3.1). These values are listed in Table 5.2. Other RA-CA parameters are the same as those discussed in previous sections. To illustrate the thermal conditions used as input for the RA-CA simulations, the melt pool profiles were extracted from the ABAQUS thermal analysis. Figure 5.1 shows both the longitudinal and cross-sectional sections of the melt pool at different preheating conditions. These views highlight the variation in melt pool shape with increasing preheat temperature, which directly governs the local thermal gradients and solidification rates applied in the subsequent grain structure simulations. The melt pool geometry at different pre heat temperature is summarized in Table 5.1. With increasing preheat temperature, both melt pool depth and width increase gradually. The depth rises from 60 µm (no preheat) to 80 µm at 800 °C, while the width increases more significantly, from 103 µm to 150 µm.

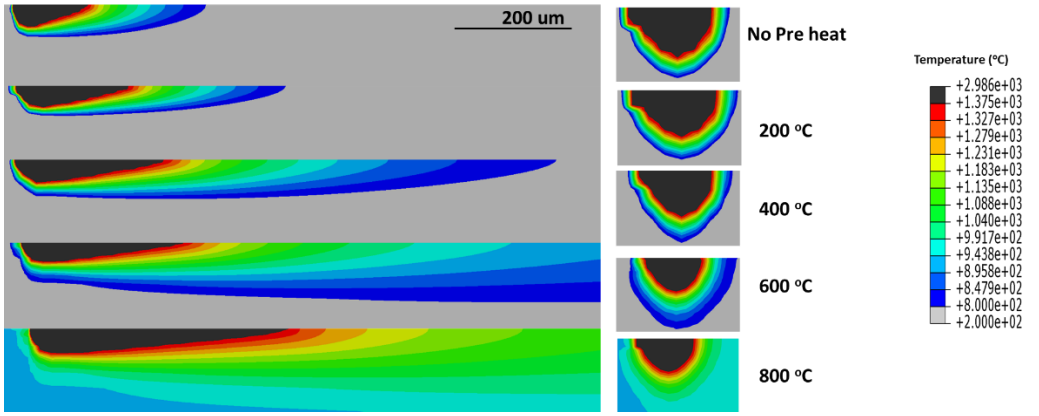


Figure 5.1 Longitudinal and cross-sectional views of melt pool profiles at different preheating temperatures obtained from ABAQUS thermal simulations

Table 5.1 Melt pool dimensions obtained from ABAQUS thermal simulations at different preheating temperatures.

Pre-Heat Temperature (°C)	Melt pool Depth (µm)	Melt Width (µm)
No Preheat	60	103
200	65	105
400	71	112
600	77	137
800	80	150

The material properties for X30Mn21 were the same as in Chapter 3 (please refer Table 3.1). This includes thermal conductivity, density, and temperature-dependent specific heat, all of which were derived using Thermo-Calc and TCFE9 database. The growth kinetics coefficients and β also remained unchanged and was based on the undercooling-based polynomial used earlier. The nucleation density values were selected based on the literature as discussed in chapter 4 (please refer section 4.3.1). These values are listed in Table 5.2. Other RA-CA parameters are the same as those discussed in previous sections.

The mechanical properties corresponding to the simulated microstructures were calculated by means of the CP-FEM [129]. The CP-FEM framework used in this study incorporates grain-level crystallographic orientation and size as inputs and accounts for slip system activity under applied loads. A brief detail of the CP-FEM model is provided in section 5.3

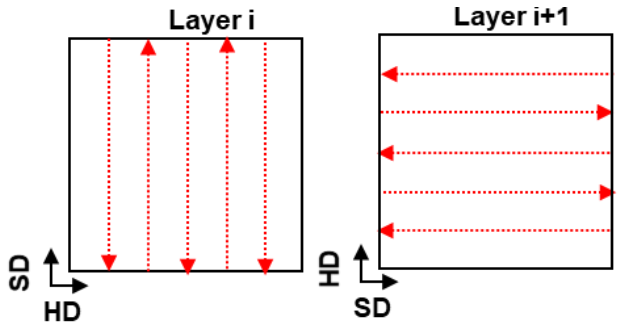


Figure 5.2 A schematic of laser scan pattern

Table 5.2 RA-CA model parameters

Parameters	Value
$\emptyset_v$ (mm^{-3})	2.6 x 10^4, 2.5 x 10^4 , 2.4 x 10^4, 1.87 x 10^4 ,1.2 x 10^4
$\emptyset_s$ (mm^{-2})	3.1 x 10^4, 2.4 x 10^4 , 2.1 x 10^4, 1.82 x 10^4 ,1.4 x 10^4
mean nucleation undercooling for bulk nucleation distribution $(\Delta T_m)_b$ (°C)	5
mean nucleation undercooling for surface nucleation distribution $(\Delta T_m)_s$ (°C)	1
standard deviation for bulk nucleation distribution $(\Delta T_\sigma)_b$ (°C)	0.2
standard deviation for surface nucleation distribution $(\Delta T_\sigma)_s$ (°C)	0.2
growth coefficients α	9×10^{-6}
growth coefficients β	3×10^{-3}

Table 5.3 LPBF process parameters for the microstructure simulation

Parameter	Value	Unit
Laser Power	120	W
Spot diameter	80	µm
Hatch spacing	70	µm
Layer thickness	30	µm
Scan speed	750	mm/sec
Preheat temperature	200°,400° 600°,800	°C

5.3 Overview of the Crystal Plasticity Finite Element Method

The main objective of this thesis was to develop an efficient CA framework and to establish a computational P-S-P linkage computationally. Hence, CP-FEM is described here in briefly for the completeness. The defining characteristic of CP-FEM is its explicit utilization of crystallographic orientations along with the grain size within its constitutive plasticity models. Therefore, the most critical part in CP-FEM simulation is the microstructure description, which serves as the input and foundation for the mechanical property prediction. In this technique, the microstructure is first represented as a three-dimensional finite element mesh, wherein each element is assigned both the orientation of the grain it belongs to and the grain size. The orientation information determines how the applied stress resolves onto the available slip system within the crystal lattices Slip systems are specific planes and directions along which dislocations can move and create plastic deformation during loading[130]. The grain size on the other hand limits the distance dislocations can move before they are blocked by a grain boundary, which directly influences the hardening behavior of the material during deformation.

In CP-FEM, the deformation gradient F for each element can be decomposed into plastic and elastic part as given by equation (5.1) . The elastic strain is used to calculate the stress in the material. The plastic part is given by the plastic velocity gradient, which adds permanent deformation by dislocation slip and other mechanisms such that twinning[130].

$$F = \mathrm{F_e}.\mathrm{F_p} \tag{5.1}$$

Where in $\mathrm{F_e}$, and $\mathrm{F_p}$ are elastic and plastic deformation gradient respectively. While the elastic deformation is computed using the generalized Hooke's law, the evolution plastic deformation is given by equation (5.2)[131]. In addition, the stress field is required to satisfy the balance of linear momentum, which is enforced by the finite element solver to ensure equilibrium between internal stresses and external forces.

$$\dot{F}_\mathrm{p} = \mathrm{L_p}.\mathrm{F_p} \tag{5.2}$$

Wherein $\mathrm{L_p}$ is the plastic velocity gradient or slip rate, and $\dot{F}_\mathrm{p}$ represent the rate of plastic deformation.

Dislocation slip is the most important mechanism of plastic deformation at room temperature. However, depending on the chemical composition of the material, additional deformation mechanisms can also contribute to plasticity. In the particular case of the investigated advanced high-strength steel X30Mn21, experimental findings have shown that Twinning-Induced Plasticity (TWIP) and Transformation-Induced Plasticity (TRIP) occur during deformation [11,110,119]. For this reason, the constitutive model employed in this work includes the effects of both twinning and ε-martensite transformation on the plastic behavior. Both twinning and transformation-induced plasticity are treated as additional, but unidirectional, deformation systems [132]. As a result, the total plastic velocity gradient consists of the combined contributions from these three strengthening mechanisms and is given by:

$$\mathbf{L_p} = (1 - f_{tw} - f_{tr}) \sum_{\alpha=1}^{N_s} \dot{\gamma_s^\alpha} s_s^\alpha \otimes m_s^\alpha + f_{tw} \left(\sum_{\beta=1}^{N_{tw}} \dot{\gamma_{tw}^\beta} s_{tw}^\beta \otimes m_{tw}^\beta \right) + f_{tr} \left(\sum_{\xi=1}^{N_{tr}} \dot{\gamma_{tr}^\xi} s_{tr}^\xi \otimes m_{tr}^\xi \right) \tag{5.3}$$

Wherein f_{tw} and f_{tr} are the volume fraction of twinned regions and transformed regions, respectively. $\dot{\gamma_s^\alpha}$ is the shear rate on slip system α, and N_s is the total number

of slip systems. For face-centered cubic (FCC) materials, there are typically 12 octahedral slip systems characterized by the Miller indices {111} ⟨ 110 ⟩. The unit vectors s_s^α and m_s^α represent the slip direction and the normal direction of the slip plane in the current configuration, respectively. The parameters N_{tw} and N_{tr} denote the total number of twinning and transformation systems. $\dot{\gamma_s^\alpha}$, $\dot{\gamma_{tw}^\beta}$ and $\dot{\gamma_{tr}^\xi}$ are the corresponding shear rates for slip, twinning and transformation-induced plasticity. s_{tw}^β and s_{tr}^ξ is slip direction in twinning and transformation respectively, while m_{tw}^β and, m_{tr}^ξ is the plane normal to twinning and transformation respectively.

The Grain size is incorporated by its influence on the dislocation mean free path, which leads to the slip strengthening. In this CP-FEM model, grain size is coupled into the evolution equation of mobile dislocation density as given in equation (5.4)

$$\dot{\rho_m} = \frac{|\dot{\gamma}|}{b_s \Lambda_s} - \frac{2\hat{d}}{b_s}\rho|\dot{\gamma}| \tag{5.4}$$

Where $\dot{\rho_m}$, $|\dot{\gamma}|$, b_s, Λ_s, $\hat{d}$, ρ denote, respectively : the rate of change of the mobile dislocation density ($m^{-2}s^{-1}$); the magnitude of the accumulated shear rate over all active deformation systems; the Burgers vector magnitude, representing the magnitude of lattice distortion due to a dislocation; the dislocation mean free path, i.e., the average distance a dislocation can travel before being blocked; a material-specific parameter related to dipole formation, the current dislocation density(m^{-2}) respectively.

The total mean free path (Λ_s) is further given by:

$$\frac{1}{\Lambda_s} = \frac{1}{D} + \frac{1}{\lambda_s} + \frac{1}{\lambda_{tw}} + \frac{1}{\lambda_{tr}} \tag{5.5}$$

where D is the average grain size, λ_s denotes the mean spacing between dislocation-related obstacles; λ_{tw} is the mean spacing between obstacles formed by deformation twins; and λ_{tr} represents the mean spacing between obstacles created by

transformed regions such as ε-martensite. Comprehensive and detailed equations of this constitutive law have already been clearly stated in literature [133,134]. Equation (5.5) shows that the grain size D directly limits the mean free path Λ_s, thereby increasing the rate of dislocation accumulation and contributing to strain hardening.

During the CP-FEM simulation, an external load or strain is incrementally applied to the mesh. For each element, the model calculates the resolved shear stress acting on all slip systems and, at each time step, the model computes the plastics and the elastic contributions together. This approach allows CP-FEM to capture the correct stress evolution, anisotropic elastic behavior, and the combination of elastic and plastic deformation during loading and unloading.

Overall, this modeling framework enables a physically based prediction of plastic deformation by explicitly incorporating crystallographic orientation, grain size, and multiple deformation mechanisms. In this work, the input microstructure data used for CP-FEM simulations was generated by the RA-CA model described in earlier chapters. The combined use of Equation (5.3) for the plastic velocity gradient and Equation (5.4) for the evolution of dislocation density provides a comprehensive description of how microstructural features influence the mechanical response. This approach allows the simulation to establish a direct process–structure–property linkage, which is essential for evaluating the effect of additive manufacturing parameters on the final performance of the material.

5.4 Microstructure Evolution under Different Preheating Temperatures

The grain structure of X30Mn21 was obtained from the RA-CA simulation under different preheating conditions. The IPF maps were generated for preheat temperatures of 200°C, 400°C, 600°C, and 800°C. Along with these, the inverse pole figure (IPF) maps and pole figures (PF) are reported to study the effects of preheating on the orientation.

For quantitative comparison, the grain size and aspect ratio distributions are reported as well.

5.4.1 Grain Morphology and Crystallographic Orientation

The simulated grain structure of X30Mn21 at different preheat temperatures is presented in Figure 5.3 The 3D grain morphology, IPF map, and the IPF plot with respect to the build direction (BD) are reported for each sample. From Figure 5.3, it could be seen that across all conditions, the grains appear elongated and show strong directional growth along the BD. This kind of morphology is typical of LPBF where directional solidification is driven by a steep thermal gradient [121,135].

In the case of no preheating or with a lower preheat temperature of 200°C, the grains are finer and have more irregular, zigzag-shaped boundaries. But as the preheat temperature increases, especially at 600°C and 800°C, the grains become longer and more columnar, and their boundaries appear straighter and more continuous.

The cooling rates at different preheating temperature is presented in Figure 5.4. The data clearly shows that the cooling rate decreases with increasing preheat temperature. For the no-preheat case, cooling rates exceed 3×10^5 K/s near the surface and increases with increasing depth of the melt pool. Nevertheless, with a preheating temperature of 800°C, the maximum cooling rate drops below 2×10^5 K/s but the rate of change of the cooling rate does not change as much as for lower preheating temperature. Moreover, the ABAQUS thermal fields (please refer Figure 5.1) reveal that the melt pool geometry becomes shallower and wider with increasing preheat, causing the thermal gradient to tilt more horizontally instead of being predominantly vertical. This means that preheating reduces the cooling rate and flattens the thermal gradient. This led to a more stable and less aggressive solidification front wherein the grains have more time to grow in a uniform direction without being interrupted by competing grains. The improved thermal stability at higher preheating temperatures also reduces grain boundary curvature, which leads to straighter boundaries and more directional growth

along the build direction. The transition from fine equiaxed grains to elongated columnar grains observed in this study can be explained by the reduction of the G/R ratio with increasing preheat temperature, as described by Kurz and Fisher [53]. Lower cooling rates reduce constitutional supercooling ahead of the solidification front, which suppresses heterogeneous nucleation and favors directional growth. Additionally, the decreased thermal gradient at higher preheats promotes competitive growth along preferred crystallographic directions, resulting in the observed <100> columnar textures.

From the intensities of the IPF, it is clear that the microstructure without preheating shows a dominant <101> || BD texture. This trend continues at 200°C. However, as the preheating temperature increases to 400°C and above, a gradual texture transition occurs. A weak but visible <100> || BD component starts to appear, and at 800°C it becomes more prominent. Meanwhile, the strength of the <101> texture begins to reduce. This shift in dominant orientation is a well-known feature in LPBF and is closely tied to changes in melt pool geometry and thermal gradient direction [119]. Higher preheat temperatures flatten the melt pool, changing the gradient direction slightly and weakening the <101> orientation. As a result, <100> oriented grains start to grow faster.

This behavior is confirmed in the IPF plots in Figure 5.3(c), where most orientations are clustered near the <101> corner for lower preheats, but begin to spread toward <100> as the preheat increases. The RA-CA model captures this texture transition well. In the model, grain growth direction is governed by alignment with the thermal gradient, as discussed earlier in Section 2.2. Since the thermal gradient is process-driven, it remains inclined in most LPBF setups, which favors <101> growth in FCC materials. However, as the preheat reduces the cooling rate and changes melt pool shape, the gradient starts shifting more vertically, which allows <100> grains to grow along the building direction. This shift aligns with literature observations [25,81,119] .

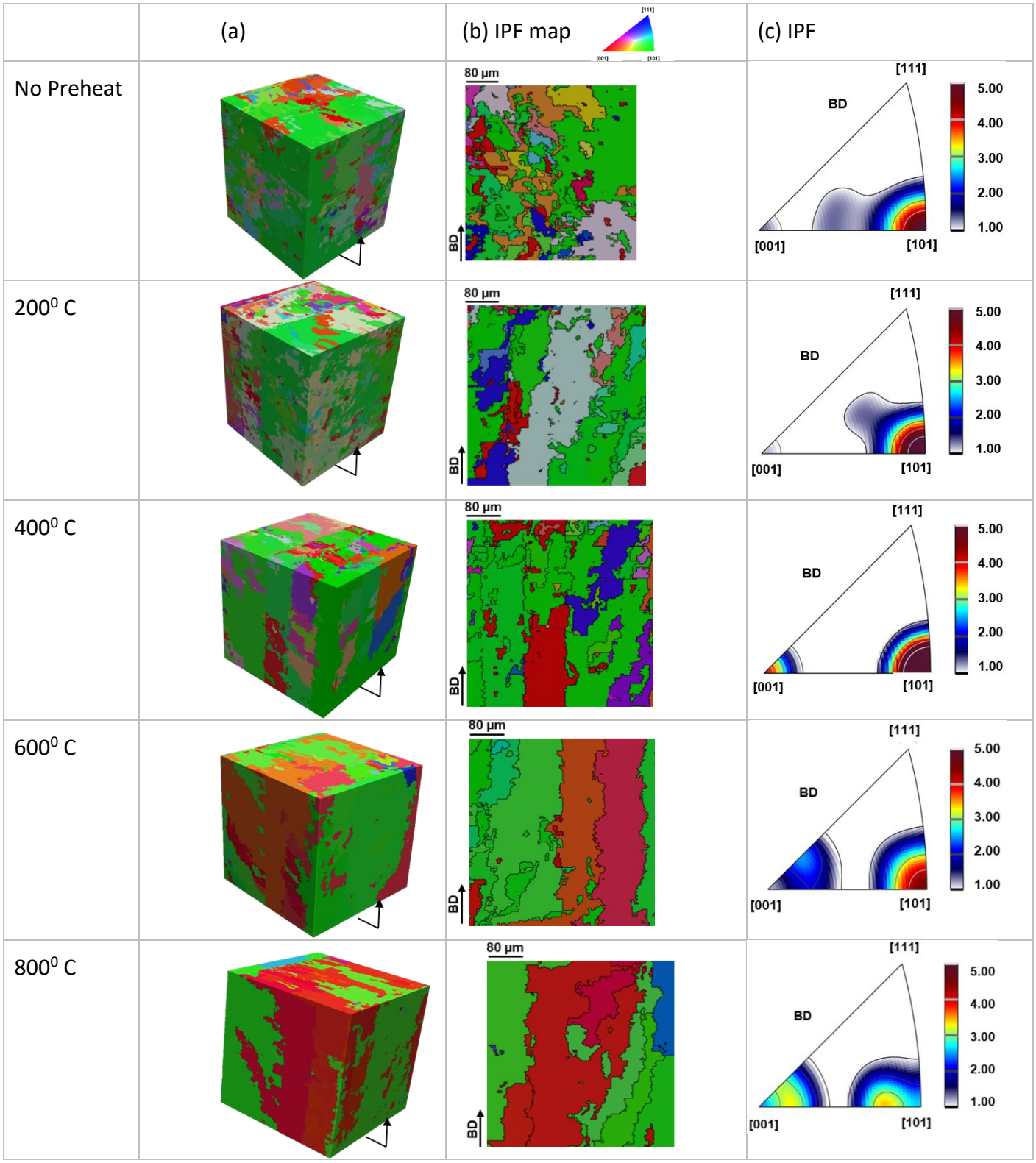


Figure 5.3 3D grain morphologies, IPF map across the portioned section and corresponding IPF of the simulated microstructure of X30Mn21

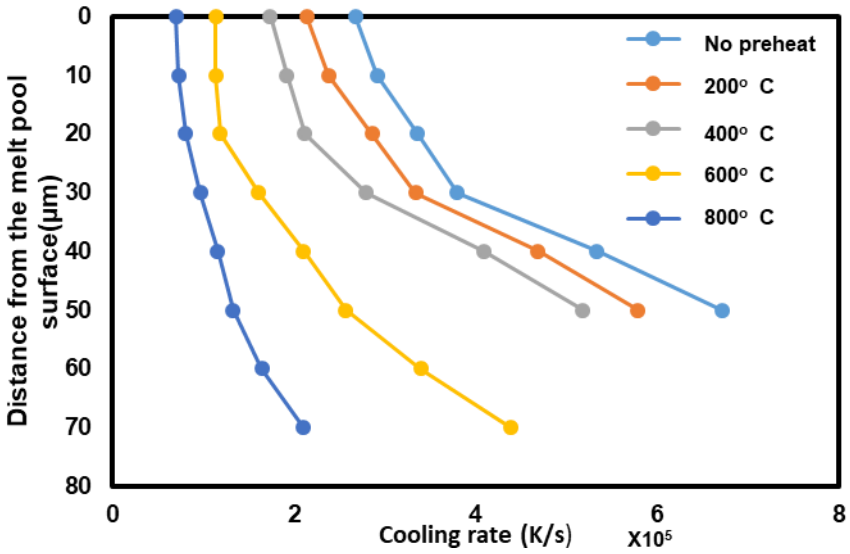


Figure 5.4 Cooling rate along the center of the melt pool depth at different pre-heat temperature

Overall, the RA-CA model was able to simulate not just the morphology changes but also the subtle crystallographic transitions induced by preheating. The transition from a mostly <101> texture to a mixed (major) <101> and <100> (minor) character becomes particularly noticeable at preheats beyond 400°C.

5.4.2 Grain Size Distributions

The average grain size for each preheating condition is presented in Figure 5.5 . The experimentally determined grain size for the same process parameters is also reported in Figure 5.5 . The experimental grain size data was taken from the work done by Kohnen at al[119]. Without preheating, the average grain size was 11.86 µm. With preheating at 800°C, the size increased to 29.14 µm i.e. a 144% increase. The model captures this coarsening behaviour well, and the simulated grain sizes closely follow the experimental trend. The effect becomes more significant above 400°C; where grain size rises rapidly with preheating temperature.

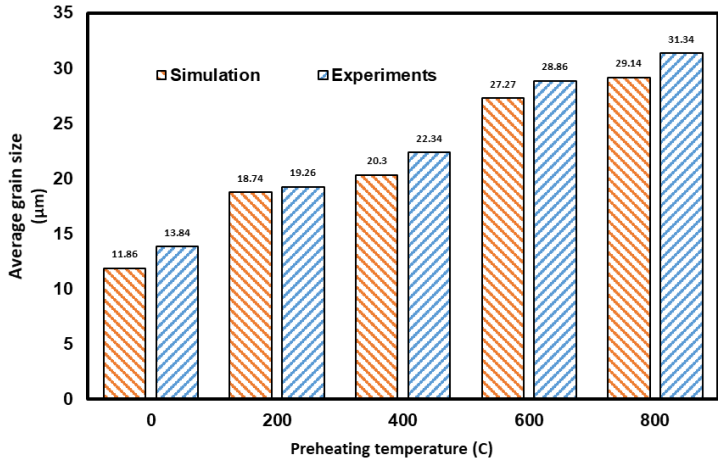


Figure 5.5 Simulated average grain size of X30Mn21 at different preheat temperatures in comparison with experimental grain sizes reported by Köhnen et al. [119]*under similar LPBF conditions.*

The grain sizes distributions for each preheating condition are shown in Figure 5.6. The histogram shows a clear drop in the number of finer grains (<10 µm) as the preheat temperature increases, and a corresponding rise in the fraction of coarser grains (>20 µm). At 800°C, the highest number of grains distribute into the largest size bins, indicating substantial coarsening. The cumulative frequency curves also shift rightwards and flatten at higher preheat temperatures, meaning the grain size range is broader and the distribution is more spread out. This further confirms that increasing preheating temperature shifts the grain population towards larger, more elongated grains due to reduced nucleation and slower solidification.

.

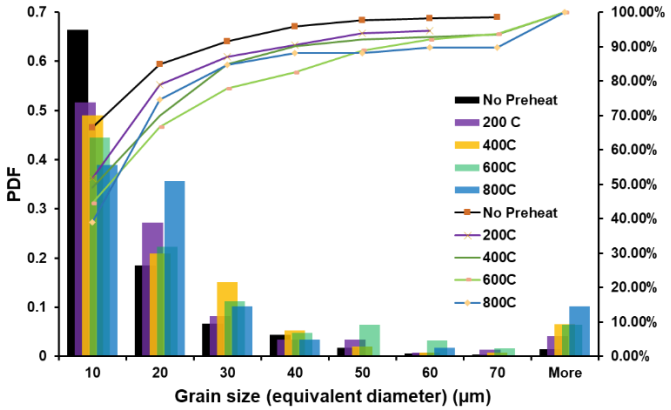


Figure 5.6 Grain size distribution and cumulative frequency plots for X30Mn21 simulated at different preheat temperatures.

These results confirm that the RA-CA model correctly links cooling conditions to grain morphology. It also captures how thermal stability introduced by preheating affects the final grain size and structure. The grain-coarsening trend observed in simulation aligns with experimental data and reflects the well-established role of thermal gradient and solidification rate in LPBF microstructure evolution.

5.4.3 Mechanical Behavior and P–S–P Linkage

In this section, the correlation between the simulated microstructures, as predicted by the RA-CA model, and the calculated mechanical properties is discussed. The input for the CP-FEM framework was the voxelized microstructure in the form of a 3D EBSD mapping. The tensile test simulations were carried out at the room temperature.

Specifically, the effect of preheat temperature, through its influence on grain size and morphology, on the stress–strain response of X30Mn21 is discussed here. The objective is to link now the structure with the properties (S–P) using CP-FEM framework to complete, thereby, the process-structure-property linkages.

The stress–strain curves corresponding to each preheat temperature are shown Figure 5.7(a), and the calculated 0.2% yield strength (YS) values are plotted in Figure 5.7 (b)

alongside experimental values taken from Köhnen et al. under similar LPBF conditions [119].

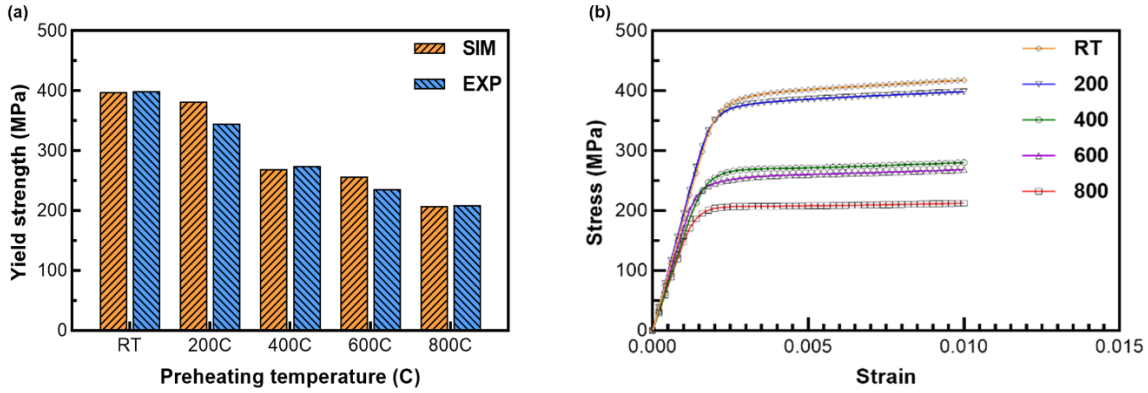


Figure 5.7 a) tensile test stress strain relations, (b) 0.2% yield strength for different preheating temperatures

The results clearly show a drop in YS with increasing preheat temperature. The highest YS of 398 MPa was obtained for the no-preheat case, which also had the smallest grain size. The lowest YS was 207.2 MPa at 800 °C, where the grains were coarsest. The difference between simulation and experiment is also within an acceptable range, with the largest deviation being around 14% at 200 °C. The CP-FEM results reflect the expected mechanical behavior based on the microstructure. The decrease in strength with increasing preheat temperature is primarily due to grain coarsening and, to a lesser extent, texture evolution. In FCC materials, the dominant slip systems are {111}<110> [136]. Considering the aforementioned slip systems, the Schmid factor remains the same for <100> and <101> loading directions [136–138]. This indicates that the observed changes in texture components (<101> || BD and <100> || BD in Figure 5.3) will have limited effects on the YS. Therefore, the grain coarsening caused by preheating plays a major role in controlling the YS. In the CP-FEM framework, grain size influences the yield strength by affecting the dislocation mean free path as given by equation (5.4). With increasing average grain size, dislocations travel further without encountering boundaries, reducing dislocation accumulation and therefore the hardening rate. This

mechanism explains the observed decrease in yield strength as grain size increases with preheating.

While the macroscopic yield strength reflects the combined influence of the grain size and the texture. However, it is indeed important to note that in the CP-FEM framework, contributions from other strengthening mechanisms such as lattice friction stress, solid solution hardening, and initial dislocation density are also included and are considered constants in the constitutive law. This serve as the baseline resistance to dislocation motion. In CP-FEM simulations, the dislocation density evolves dynamically in each iteration as a function of the applied load and the local microstructure which provides a realistic description of strain hardening. Moreover, the model explicitly includes for twinning-induced plasticity (TWIP) and transformation-induced plasticity (TRIP) (please refer equation (5.3)). Although these mechanisms are present, their influence on the early-stage plastic deformation and yield stress is bare minimum in this case due to their extremely low volume fractions (approximately 0.01%) during the initial loading phase. This observation is consistent with in-situ experimental studies that report a relatively flat stress-strain response during the early plastic deformation of this steel [139,140]. Nevertheless, twinning and transformation are known to contribute significantly to the hardening behavior beyond the yield point and become increasingly important at higher strains. It should also be emphasized that a complete prediction of the material behavior up to failure would require the incorporation of fracture mechanics models and more detailed treatment of damage evolution, which are beyond the scope of the present study.

5.5 Conclusion

In this Chapter the effects of Preheating on the microstructure and resulting mechanical property of LPBfed of X30Mn21 alloys were studied. At first, the developed RA-CA model was employed to predict the microstructure of X30Mn21 under various

preheat conditions ranging from 0 °C to 800 °C. The simulated microstructures were then integrated into CP-FEM framework to predict the respective mechanical property. This chapter concludes the followings key findings:

1. The preheating of the bed has a significant effect on the cooling rate of the melt pool. Moreover, the cooling rate along the melt pool depth becomes more uniform at elevated preheat temperatures.

2. A gradual reduction in thermal gradients with increasing preheat temperature promotes the growth of coarser grains and suppresses random nucleation.

3. Texture evolution is strongly affected by preheat temperature. At lower preheat temperatures, a dominant <101> || build direction (BD) texture is observed, while a secondary <100> || BD texture becomes evident when preheat temperature exceeds 400 °C.

4. Grain morphology transitions from fine, equiaxed, and weakly textured at 0–200 °C to elongated, columnar, and well-oriented at 600–800 °C and is consistent with experimental observations in the literature.

5. The simulated mechanical response indicates a reduction in yield strength with increasing preheat temperature, which aligns with experimental observations.

6. The integrated CA-CPFEM framework effectively captures the Process–Structure–Property (P-S-P) relationships, demonstrating its utility for predictive design and first-order property estimation in materials research.

Overall, this chapter demonstrates the potential of predictive modeling in tailoring microstructure and mechanical properties of additively manufactured components through thermal process control, thus helping to establish a reliable process–structure–property (P–S–P) linkage for LPBF.

Chapter 6

General Conclusion and Future Scope

This thesis presents a comprehensive and efficient computational framework for predicting microstructure evolution in Laser Powder Bed Fusion (LPBF).The objective was to develop a fast yet physically consistent Remelting Aware Cellular Automaton (CA) framework that could handle the computational redundancies that arises due to remelting and solidification during LPBF. This was done by introducing a key algorithm in the conventional CA framework, which tracks the final solidification time of each cell during LPBF thereby improving computational efficiency without sacrificing physical accuracy.

One of the key features of this framework is its orientation assignment strategy for nucleated grains. The orientations of the grains in this framework were systematically assigned to align along the local thermal gradient. Because of this physically motivated approach, the model demonstrated a strong ability to replicate the typical grain anisotropy seen in metal fabricated with LPBF.

The performance of the model was tested under the different nucleation strategy and its effect on microstructure was evaluated. It was found that the model responds logically to changes in nucleation type and behaves in a way consistent with reported LPBF solidification trends such as equiaxed grain formation near the centerline with bulk nucleation and columnar grains with epitaxial seeding.

The model's robustness was further demonstrated through rigorous comparison with experimental data from LPBF-processed X30Mn21 steel alloy. The simulated microstructural features like grain morphology, grain size distribution and texture, showed strong resemblance with the one obtained from the experiments. Moreover, due to the efficient handling of remelting during LPBF, the present RA-CA model turns out to be at least 30% faster than a conventional CA model for LPBF. Moreover, to further enhance the effectiveness of the simulation, the RA-CA model was parallelized using MPI. The parallelization of RA-CA significantly increase the simulation speed. This becomes particularly important for scaling the model to part-level simulations in the future.

Moreover, the framework was also extended to analyze the influence of powder bed preheating on the microstructure evolution, and it was able to predict the transition in grain morphology and orientation as a function of thermal input. The ability to reproduce such process responsive features reinforces the reliability of RA-CA model as a predictive tool. Apart from predicting fidelity, the potential for developing a Process-Structure-Property (P-S-P) was also evaluated. The grain level features obtained with RA-CA simulation were coupled with CP-FEM simulation and the corresponding mechanical behavior was studied. The CP-FEM simulations based on the RA-CA simulation were able to capture both the grain size and the crystallographic texture influence on the yield strength of X30Mn21 alloy. This framework serves as a foundational tool for understanding how microstructural characteristics evolve and influence downstream mechanical behavior.

Furthermore, although the validation in this thesis was carried out for a high-manganese steel (X30Mn21), the developed RA-CA framework is not restricted to only this material. In principle, the model is applicable to all single-phase alloys processed by LPBF. With a change of material, the growth kinetics can be recalculated based on the relevant thermophysical properties, and the nucleation parameters can be adapted

according to alloy chemistry and process parameters. This flexibility makes the framework broadly applicable beyond the case study presented here.

6.1 Limitations of the Present Model

While the developed RA-CA framework has proven effective in capturing key features of LPBF microstructure and has shown strong agreement with experimental observations, the present model is not without limitations. Several important phenomena known to affect microstructural and mechanical responses in LPBF remain outside the scope of this work. Recognizing these limitations is important, as their inclusion in future developments could further enhance the predictive capability and broaden the applicability of the framework.

- The current framework focuses solely on solidification-driven grain evolution and does not incorporate static or dynamic recrystallization, which may occur during LPBF or subsequent thermal exposure.

- The simulations are restricted to directly melted and resolidified regions. The surrounding HAZ, commonly observed in LPBF due to localized thermal cycling, is not represented, limiting the ability to capture grain coarsening or substructure evolution.

- The model does not resolve solute redistribution or microsegregation effects within the melt pool. Phenomena such as, segregation, secondary phase formation is not considered

- The present RA-CA framework focuses exclusively on solidification-driven grain structure evolution (nucleation, growth, and texture) and does not include dislocation dynamics. Cellular Automaton models are mesoscale in nature and operate on grain-scale phenomena, while dislocation density arises from sub-grain plasticity mechanisms that require crystal plasticity or dislocation dynamics frameworks. As such, the RA-CA model cannot directly provide dislocation density predictions.

6.2 Future Scope

Based upon the limitations of the model, the following directions are identified to extend the framework and overcome current challenge. The most relevant are outlined as below:

1. **Integration with Multi-Phase and Precipitation Models**

   Many advanced alloys used in additive manufacturing, such as aluminum-scandium systems, are often subjected to precipitation and the performance of such alloys does not only depends on its grain structure and texture but also on the secondary phase or precipitation. Coupling the RA-CA simulation with precipitation models would provide a more complete picture of microstructural evolution in such complex alloys.

2. **Machine Learning-Based Surrogate Modeling**

   The RA-CA model can generate large datasets mapping processing conditions to microstructure, and when coupled with CP FEM, can also generate the mechanical properties. These datasets can be used to train machine learning models that predict grain morphology, texture, and mechanical properties without full simulations. This will

allow faster screening of process windows and open opportunities for real-time process optimization.

3. **Optimization of Parallel Efficiency**

While the remelting-aware logic improved runtime, efficiency losses were reported at higher processor counts. The static domain decomposition strategy reduces the efficiency of the processors because of load imbalances among the processors. To further increase the efficiency of the parallel computing, other techniques like dynamic domain decomposition can be used

In conclusion, this dissertation introduced a new computational model (RA-CA) that successfully addresses the key microstructural challenges associated with LPBF. The framework combined thermally informed grain orientation, remelting-aware logic, and validated accuracy to offer both speed and realism in simulation. Its demonstrated capability to predict and analyze microstructural evolution under various process conditions, along with its extensibility to data-driven and multi-phase modeling, positions it as a valuable tool for both scientific exploration and industrial application in metal additive manufacturing.

Funding

The research presented in this thesis was conducted within the framework of the XS-Meta Consortium, an Innovative Training Network dedicated to advancing cross-scale modeling and experimental approaches in metallic materials. This project received funding from the European Union's Horizon 2020 Research and Innovation Programme under the Marie Skłodowska-Curie Grant Agreement No. 956401 (XS-Meta).

Appendix A: Pseudocode Algorithms

A.1 Generate Uniform Random Quaternion

This pseudocode generates a uniformly distributed random orientation in 3D space by constructing a unit quaternion. The method samples two random angles and transforms them into quaternion components using trigonometric functions and square root scaling. This ensures that the generated orientations are uniformly distributed over the rotation group SO(3), avoiding bias that would arise from naive Euler angle sampling. The resulting quaternion can be used to assign random crystal orientations in microstructure simulations.

Input:
None

Output:
$q = (q_0, q_1, q_2, q_3)$: A unit quaternion representing a uniform random 3D orientation

Procedure:
Generate random number $s \in [0, 1]$ → $s \leftarrow$ rand()
Compute auxiliary variables:
$\sigma_1 \leftarrow \text{sqrt}(1 - s)$
$\sigma_2 \leftarrow \text{sqrt}(s)$

Generate random angles $\theta_1, \theta_2 \in [0, 2\pi]$:
$\theta_1 \leftarrow 2\pi \times$ rand()
$\theta_2 \leftarrow 2\pi \times$ rand()

Compute quaternion components:
$q_0 \leftarrow \sigma_2 \times \cos(\theta_2)$ // scalar part
$q_1 \leftarrow \sigma_1 \times \sin(\theta_1)$ // $\hat{i}$ component
$q_2 \leftarrow \sigma_1 \times \cos(\theta_1)$ // $\hat{j}$ component
$q_3 \leftarrow \sigma_2 \times \sin(\theta_2)$ // $\hat{k}$ component

Set $q \leftarrow (q_0, q_1, q_2, q_3)$
Return q

A.2 Final Solidification Time Tracking (CA Cell Activation)

This pseudocode determines the final solidification time for each CA cell by scanning the temperature history backward in time. The goal is to find the last time the cell transitions from liquid to solid after all remelting events have occurred. This ensures that each cell is only activated once, after its final solidification.

```
Input:
| T_i(t): Temperature history of CA cell i
| T_liquidus: Liquidus temperature of the alloy
| Δt: Time step of CA simulation

Output:
| t_final[i]: Final solidification time for each CA cell

For each CA cell i do:
|   Set t_final[i] ← None
|   For t ← t_max down to t_0 step -Δt do:
|   |   If T_i(t) ≤ T_liquidus AND T_i(t + Δt) > T_liquidus then:
|   |   |   t_final[i] ← t       // Final transition from liquid to solid
|   |   |   Break
|   |   End If
|   End For
End For
For each simulation time step t do:
|   For each cell i where t_final[i] == t do:
|   |   Activate cell i for nucleation and grain growth
|   End For
End For
```

Abstract

Additive manufacturing (AM) is a novel technology that consists of fabricating 3D components by joining materials, usually layer by layer. Among all the AM techniques, laser powder bed fusion process (LPBF) has become a leading technique for manufacturing near-net-shape metallic parts. LPBF employs a laser beam, in which the laser beam scans the layer of powder in a controlled trajectory and induces melting and solidification of the material locally, giving the designer design flexibilities. The LPBF process is extensively used for processing new materials and complex designs. However, rapid cooling and high thermal gradients associated with LPBF often lead to formation of distinct microstructure, often generating different mechanical properties compared to conventional methods. In this work, a novel parallelized Remelting Aware Cellular Automaton (RA-CA) framework is presented for modelling the evolution of microstructure during the LPBF. One of the major challenges in modeling microstructure in LPBF is handling the repeated remelting and re-solidification that occurs during the LPBF process. This repeated cycle of melting and solidification during LPBF elevates the computational load. In this study, a new approach to nucleation seeding and crystal growth is implemented, which focuses solely on the final stages of melting and solidification. This approach streamlines the simulation process, making it efficient and effective. The RA-CA framework was validated for an advanced austenitic high strength steel (AHSS) X30Mn21 alloy. For validating the model, the simulated microstructure features were qualitatively and quantitatively compared with the experimental data. The RA-CA model was further extended to investigate the effect of preheating on the grain structure and mechanical properties of the X30Mn21 alloy. Preheating the build platform is an effective strategy to mitigate thermal gradients involved in LPBF, offering improved control over microstructure evolution. Therefore, simulation was performed at different preheat temperatures starting from no preheat, 200°C, 400°C, 600°C, and

800°C. The simulated microstructures were then analyzed, and corresponding mechanical properties were predicted using crystal plasticity finite element modeling (CPFEM) within the DAMASK framework. The model predictions were in agreement with the results reported in the literature. The results demonstrate a clear correlation between preheat temperature, grain orientation, and mechanical response, supporting the use of a physics-based Process–Structure–Property (P–S–P) linkage for alloy design and process optimization in additive manufacturing. This work also shows the potential P–S–P linkage computationally, thereby reducing dependency on the experiment for new material processing techniques.

Keywords: LPBF, Microstructure, Cellular Automaton, Modelling, Simulation

Résumé

La fabrication additive (FA) est une technologie novatrice qui consiste à fabriquer des composants 3D par l'assemblage de matériaux, généralement couche par couche. Parmi toutes les techniques de FA, le procédé de fusion laser sur lit de poudre (LPBF) est devenu une technique de pointe pour la fabrication de pièces métalliques proches de la forme finale. Le procédé LPBF est largement utilisé pour le traitement de nouveaux matériaux et de conceptions complexes. Cependant, le refroidissement rapide et les gradients thermiques élevés associés au LPBF conduisent souvent à la formation de microstructures distinctes, générant des propriétés mécaniques différentes par rapport aux méthodes conventionnelles. Dans ce travail, un nouveau cadre d'automate cellulaire parallèle, sensible au refusionnage (RA-CA), est présenté pour modéliser l'évolution de la microstructure pendant le procédé LPBF. L'un des principaux défis de la modélisation de la microstructure dans le LPBF est la gestion des refusionnages et re-solidifications répétés qui se produisent au cours du procédé LPBF. Ce cycle répété de fusion et de solidification pendant le LPBF augmente considérablement la charge de calcul. Dans cette étude, une nouvelle approche de nucléation et de croissance cristalline est mise en œuvre, se concentrant uniquement sur les étapes finales de fusion et de solidification. Cette approche élimine les redondances dues au refusionnage, rendant ainsi la simulation efficace. Le cadre RA-CA a été validé pour un acier austénitique à haute résistance avancé (AHSS), l'alliage X30Mn21. Les caractéristiques microstructurales simulées ont été comparées qualitativement et quantitativement aux données expérimentales pour la validation. Le modèle RA-CA a été ensuite étendu afin d'étudier l'effet du préchauffage sur la structure des grains et les propriétés mécaniques de l'alliage X30Mn21. Le préchauffage de la plateforme de fabrication est une stratégie efficace pour atténuer les gradients thermiques impliqués dans le LPBF, offrant un meilleur contrôle de l'évolution microstructurale. Par conséquent, des simulations ont été effectuées à différentes températures de préchauffage allant de l'absence de préchauffage à 200 °C, 400 °C, 600 °C et 800 °C. Les microstructures simulées ont ensuite

été analysées, et les propriétés mécaniques correspondantes ont été prédites à l'aide de la modélisation éléments finis en plasticité cristalline (CPFEM) dans le cadre de DAMASK. Les prédictions du modèle étaient en accord avec les résultats rapportés dans la littérature. Les résultats montrent une corrélation claire entre la température de préchauffage, l'orientation des grains et la réponse mécanique, soutenant l'utilisation d'un lien physique Processus–Structure–Propriété (P–S–P) pour la conception d'alliages et l'optimisation des procédés en fabrication additive. Ce travail montre également le potentiel du lien P–S–P de manière computationnelle, réduisant ainsi la dépendance à l'expérimentation pour les nouvelles techniques de traitement des matériaux

Mots-clés : LPBF, microstructure, automate cellulaire, modélisation, simulation

Bibliography

[1] K. V. Wong, A. Hernandez, A Review of Additive Manufacturing, ISRN Mech. Eng. 2012 (2012) 1–10. https://doi.org/10.5402/2012/208760.

[2] ASTM INTERNATIONAL,] I. Gibson, D. Rosen, and B. Stucker, Additive Manufacturing Technologies. NewYork, NY: Springer New York, 2015, Rapid Manuf. Assoc. (2013) 1–3. https://doi.org/10.1520/F2792-12A.2.

[3] N. Guo, M.C. Leu, Additive manufacturing: Technology, applications and research needs, Front. Mech. Eng. 8 (2013) 215–243. https://doi.org/10.1007/s11465-013-0248-8.

[4] L.-C. Zhang, H. Attar, M. Calin, J. Eckert, Review on manufacture by selective laser melting and properties of titanium based materials for biomedical applications, Mater. Technol. 31 (2015) 66–76. https://doi.org/10.1179/1753555715y.0000000076.

[5] C.Y. Yap, C.K. Chua, Z.L. Dong, Z.H. Liu, D.Q. Zhang, L.E. Loh, S.L. Sing, Review of selective laser melting: Materials and applications, Appl. Phys. Rev. 2 (2015) 041101. https://doi.org/10.1063/1.4935926.

[6] E.O. Olakanmi, R.F. Cochrane, K.W. Dalgarno, A review on selective laser sintering/melting (SLS/SLM) of aluminium alloy powders: Processing, microstructure, and properties, Prog. Mater. Sci. 74 (2015) 401–477. https://doi.org/10.1016/j.pmatsci.2015.03.002.

[7] W.E. Frazier, Metal additive manufacturing: A review, J. Mater. Eng. Perform. 23 (2014) 1917–1928. https://doi.org/10.1007/s11665-014-0958-z.

[8] A. Yadollahi, N. Shamsaei, Additive manufacturing of fatigue resistant materials: Challenges and opportunities, Int. J. Fatigue. 98 (2017) 14–31. https://doi.org/10.1016/j.ijfatigue.2017.01.001.

[9] J. Pakkanen, M. Lombardi, M. Lorusso, F. Trevisan, P. Fino, D. Manfredi, A. Aversa, E. Ambrosio, F. Calignano, On the Selective Laser Melting (SLM) of the AlSi10Mg Alloy: Process, Microstructure, and Mechanical Properties, Materials (Basel). 10 (2017) 76. https://doi.org/10.3390/ma10010076.

[10] B. Song, X. Zhao, S. Li, C. Han, Q. Wei, S. Wen, J. Liu, Y. Shi, Differences in microstructure and properties between selective laser melting and traditional manufacturing for fabrication of metal parts : A review, 10 (2015) 111–125. https://doi.org/10.1007/s11465-015-0341-2.

[11] P. Bajaj, A. Hariharan, A. Kini, P. Kürnsteiner, D. Raabe, E.A. Jägle, Steels in additive manufacturing: A review of their microstructure and properties, Mater. Sci. Eng. A. 772 (2020). https://doi.org/10.1016/j.msea.2019.138633.

[12] C. Körner, M. Markl, J.A. Koepf, Modeling and Simulation of Microstructure Evolution for Additive Manufacturing of Metals: A Critical Review, Metall. Mater. Trans. A Phys. Metall. Mater. Sci. 51 (2020) 4970–4983. https://doi.org/10.1007/s11661-020-05946-3.

[13] K.H. Lee, G.J. Yun, Prediction of melt pool dimension and residual stress evolution with thermodynamically-consistent phase field and consolidation models during re-melting process of SLM, Comput. Mater. Contin. 66 (2021) 87–112. https://doi.org/10.32604/cmc.2020.012688.

[14] Y. Zhang, X. Xiao, J. Zhang, Kinetic Monte Carlo simulation of sintering behavior of additively manufactured stainless steel powder particles using reconstructed microstructures from synchrotron X-ray microtomography, Results Phys. 13 (2019) 102336. https://doi.org/10.1016/j.rinp.2019.102336.

[15] T.M. Rodgers, J.D. Madison, V. Tikare, Simulation of metal additive manufacturing microstructures using kinetic Monte Carlo, Comput. Mater. Sci. 135 (2017) 78–89. https://doi.org/10.1016/j.commatsci.2017.03.053.

[16] Y. Lian, S. Lin, W. Yan, W.K. Liu, G.J. Wagner, A parallelized three-dimensional cellular automaton model for grain growth during additive manufacturing, Comput. Mech. 61 (2018) 543–558. https://doi.org/10.1007/s00466-017-1535-8.

[17] J. Yang, H. Yu, H. Yang, F. Li, Z. Wang, X. Zeng, Prediction of microstructure in selective laser melted Ti–6Al–4V alloy by cellular automaton, J. Alloys Compd. 748 (2018) 281–290. https://doi.org/10.1016/j.jallcom.2018.03.116.

[18] X. Zhang, C.J. Yocom, B. Mao, Y. Liao, Microstructure evolution during selective laser melting of metallic materials: A review, J. Laser Appl. 31 (2019) 031201. https://doi.org/10.2351/1.5085206.

[19] J.A. Koepf, D. Soldner, M. Ramsperger, J. Mergheim, M. Markl, C. Körner, Numerical microstructure prediction by a coupled finite element cellular automaton model for selective electron beam melting, Comput. Mater. Sci. 162 (2019) 148–155. https://doi.org/10.1016/j.commatsci.2019.03.004.

[20] Q.L. Liu, X.M. Li, Y.H. Jiang, Microstructure evolution of large-scale titanium slab ingot based on CAFE method during EBCHM, J. Mater. Res. 32 (2017) 3175–3182. https://doi.org/10.1557/jmr.2017.174.

[21] J. Kundin, A. Ramazani, U. Prahl, C. Haase, Microstructure Evolution of Binary and Multicomponent Manganese Steels During Selective Laser Melting: Phase-Field Modeling and Experimental Validation, Metall. Mater. Trans. A. 50 (2019) 2022–2040. https://doi.org/10.1007/s11661-019-05143-x.

[22] Y. Lian, Z. Gan, C. Yu, D. Kats, W.K. Liu, G.J. Wagner, A cellular automaton finite volume method for microstructure evolution during additive manufacturing, Mater. Des. 169 (2019) 107672. https://doi.org/10.1016/j.matdes.2019.107672.

[23] M.S. Mohebbi, V. Ploshikhin, Implementation of nucleation in cellular automaton simulation of microstructural evolution during additive

manufacturing of Al alloys, Addit. Manuf. 36 (2020) 101726. https://doi.org/10.1016/j.addma.2020.101726.

[24] C.H. Fu, Y.B. Guo, Three-Dimensional Temperature Gradient Mechanism in Selective Laser Melting of Ti-6Al-4V, J. Manuf. Sci. Eng. Trans. ASME. 136 (2014) 1–7. https://doi.org/10.1115/1.4028539.

[25] K. Teferra, D.J. Rowenhorst, Optimizing the cellular automata finite element model for additive manufacturing to simulate large microstructures, Acta Mater. 213 (2021). https://doi.org/10.1016/j.actamat.2021.116930.

[26] D.S. Bulgarevich, S. Nomoto, M. Watanabe, M. Demura, Crystal plasticity simulations with representative volume element of as-build laser powder bed fusion materials, Sci. Rep. 13 (2023) 1–16. https://doi.org/10.1038/s41598-023-47651-2.

[27] K.G. Prashanth, S. Scudino, T. Maity, J. Das, J. Eckert, Is the energy density a reliable parameter for materials synthesis by selective laser melting?, Mater. Res. Lett. 5 (2017) 386–390. https://doi.org/10.1080/21663831.2017.1299808.

[28] K. Kempen, E. Yasa, L. Thijs, J.P. Kruth, J. Van Humbeeck, Microstructure and mechanical properties of selective laser melted 18Ni-300 steel, Phys. Procedia. 12 (2011) 255–263. https://doi.org/10.1016/j.phpro.2011.03.033.

[29] V.S. Sufiiarov, A.A. Popovich, E. V. Borisov, I.A. Polozov, D. V. Masaylo, A. V. Orlov, The Effect of Layer Thickness at Selective Laser Melting, Procedia Eng. 174 (2017) 126–134. https://doi.org/10.1016/j.proeng.2017.01.179.

[30] A. Singh, L. Caprio, B. Previtali, A.G. Demir, Processability of pure Cu by LPBF using a ns-pulsed green fiber laser, Opt. Laser Technol. 154 (2022) 108310. https://doi.org/10.1016/J.OPTLASTEC.2022.108310.

[31] M. Shiomi, K. Osakada, K. Nakamura, T. Yamashita, F. Abe, Residual stress within metallic model made by selective laser melting process, CIRP Ann. - Manuf.

Technol. 53 (2004) 195–198. https://doi.org/10.1016/S0007-8506(07)60677-5.

[32] L. Caprio, A.G. Demir, B. Previtali, Influence of pulsed and continuous wave emission on melting efficiency in selective laser melting, J. Mater. Process. Technol. 266 (2019) 429–441. https://doi.org/10.1016/j.jmatprotec.2018.11.019.

[33] W.J. Sames, F.A. List, S. Pannala, R.R. Dehoff, S.S. Babu, The metallurgy and processing science of metal additive manufacturing, Int. Mater. Rev. 61 (2016) 315–360. https://doi.org/10.1080/09506608.2015.1116649.

[34] Y. Qin, U.M. Dilberoglu, B. Gharehpapagh, U. Yaman, M. Dolen, N. Guo, M.C. Leu, M.N. Jahangir, M.A.H. Mamun, M.P. Sealy, A. Rashid, ASTM INTERNATIONAL, ASTM F2792-12a, Rapid Manuf. Assoc. 11 (2013) 39–46. https://doi.org/10.1520/F2792-12A.2.

[35] N.T. Aboulkhair, N.M. Everitt, I. Ashcroft, C. Tuck, Reducing porosity in AlSi10Mg parts processed by selective laser melting, Addit. Manuf. 1 (2014) 77–86. https://doi.org/10.1016/j.addma.2014.08.001.

[36] M.A. Buhairi, F.M. Foudzi, F.I. Jamhari, A.B. Sulong, N.A.M. Radzuan, N. Muhamad, I.F. Mohamed, A.H. Azman, W.S.W. Harun, M.S.H. Al-Furjan, Review on volumetric energy density: influence on morphology and mechanical properties of Ti6Al4V manufactured via laser powder bed fusion, Prog. Addit. Manuf. 8 (2023) 265–283. https://doi.org/10.1007/s40964-022-00328-0.

[37] T.D. Ngo, A. Kashani, G. Imbalzano, K.T.Q. Nguyen, D. Hui, Additive manufacturing (3D printing): A review of materials, methods, applications and challenges, Compos. Part B Eng. 143 (2018) 172–196. https://doi.org/10.1016/j.compositesb.2018.02.012.

[38] Q. Jia, D. Gu, Selective laser melting additive manufacturing of Inconel 718 superalloy parts: Densification, microstructure and properties, J. Alloys Compd.

585 (2014) 713–721. https://doi.org/10.1016/j.jallcom.2013.09.171.

[39] D. Bourell, J.P. Kruth, M. Leu, G. Levy, D. Rosen, A.M. Beese, A. Clare, Materials for additive manufacturing, CIRP Ann. - Manuf. Technol. 66 (2017) 659–681. https://doi.org/10.1016/j.cirp.2017.05.009.

[40] I. Minkoff, Solidification/Liquid State Processes, in: Mater. Process., 1992: pp. 1–31. https://doi.org/10.1007/978-3-642-95562-4_1.

[41] W.D. Callister, Materials science and engineering : an introduction, John Wiley & Sons, 2007.

[42] U. Kumar Mohanty, H. Sarangi, Solidification of Metals and Alloys, in: Cast. Process. Model. Met. Mater., IntechOpen, 2021. https://doi.org/10.5772/intechopen.94393.

[43] D.M. Stefanescu, R. Ruxanda, Fundamentals of Solidification, Metallogr. Microstruct. (2018) 71–92. https://doi.org/10.31399/asm.hb.v09.a0003724.

[44] J.L. Kenty, J.P. Hirth, Epitaxy and heterogeneous nucleation theory, Surf. Sci. 15 (1969) 403–424. https://doi.org/10.1016/0039-6028(69)90132-0.

[45] J.H. Hollomon, D. Turnbull, Nucleation, Prog. Met. Phys. 4 (1953) 333–388. https://doi.org/10.1016/0502-8205(53)90020-3.

[46] S. Kou, Welding Metallurgy, Wiley, 2002. https://doi.org/10.1002/0471434027.

[47] Q. Zhang, J. Chen, L. Wang, H. Tan, X. Lin, W. Huang, Solidification Microstructure of Laser Additive Manufactured Ti6Al2Zr2Sn3Mo1.5Cr2Nb Titanium Alloy, J. Mater. Sci. Technol. 32 (2016) 381–386. https://doi.org/10.1016/j.jmst.2015.11.019.

[48] X. Li, W. Tan, Numerical investigation of effects of nucleation mechanisms on grain structure in metal additive manufacturing, Comput. Mater. Sci. 153 (2018) 159–169. https://doi.org/10.1016/j.commatsci.2018.06.019.

[49] W. Metallurgy, Welding Metallurgy, (2003).

[50] Z. Dong, Y. Liu, W. Wen, J. Ge, J. Liang, Effect of hatch spacing on melt pool and as-built quality during selective laser melting of stainless steel: Modeling and experimental approaches, Materials (Basel). 12 (2018). https://doi.org/10.3390/ma12010050.

[51] J. Wang, W.J. Wu, W. Jing, X. Tan, G.J. Bi, S.B. Tor, K.F. Leong, C.K. Chua, E. Liu, Improvement of densification and microstructure of ASTM A131 EH36 steel samples additively manufactured via selective laser melting with varying laser scanning speed and hatch spacing, Mater. Sci. Eng. A. 746 (2019) 300–313. https://doi.org/10.1016/j.msea.2019.01.019.

[52] K. Herfurth, S. Scharf, Casting, Springer Handbooks. (2021) 325–356. https://doi.org/10.1007/978-3-030-47035-7_10.

[53] W. Kurz, D.J. Fisher, M. Rappaz, Fundamentals of Solidification 5th Edition, 103 (2023) 372. https://www.scientific.net/book/fundamentals-of-solidification-5th-edition/978-3-0364-1015-9%0Ahttps://www.scientific.net/FoMSE.103%0Ahttps://www-scientific-net.remotexs.ntu.edu.sg/book/fundamentals-of-solidification-5th-edition/978-3-0364-1015-9.

[54] K.F. Kelton, A.L. Greer, Solidification, in: 2010: pp. 461–510. https://doi.org/10.1016/S1470-1804(09)01513-2.

[55] T. DebRoy, H.L. Wei, J.S. Zuback, T. Mukherjee, J.W. Elmer, J.O. Milewski, A.M. Beese, A. Wilson-Heid, A. De, W. Zhang, Additive manufacturing of metallic components – Process, structure and properties, Prog. Mater. Sci. 92 (2018) 112–224. https://doi.org/10.1016/j.pmatsci.2017.10.001.

[56] S. Suwas, R.K. Ray, Crystallographic Texture of Materials, Springer London, London, 2014. https://doi.org/10.1007/978-1-4471-6314-5.

[57] O. Engler, V. Randle, Introduction to Texture Analysis, CRC Press, 2009. https://doi.org/10.1201/9781420063660.

[58] O. Andreau, I. Koutiri, P. Peyre, J.D. Penot, N. Saintier, E. Pessard, T. De Terris, C. Dupuy, T. Baudin, Texture control of 316L parts by modulation of the melt pool morphology in selective laser melting, J. Mater. Process. Technol. 264 (2019) 21–31. https://doi.org/10.1016/j.jmatprotec.2018.08.049.

[59] P. Ansari, A.U. Rehman, F. Pitir, S. Veziroglu, Y.K. Mishra, O.C. Aktas, M.U. Salamci, Selective laser melting of 316l austenitic stainless steel: Detailed process understanding using multiphysics simulation and experimentation, Metals (Basel). 11 (2021). https://doi.org/10.3390/met11071076.

[60] M. Simonelli, Y.Y. Tse, C. Tuck, Microstructure of Ti-6Al-4V produced by selective laser melting, J. Phys. Conf. Ser. 371 (2012). https://doi.org/10.1088/1742-6596/371/1/012084.

[61] L.Q. Chen, Phase-field models for microstructure evolution, Annu. Rev. Mater. Sci. 32 (2002) 113–140. https://doi.org/10.1146/annurev.matsci.32.112001.132041.

[62] W.J. Boettinger, J.A. Warren, C. Beckermann, A. Karma, Phase-field simulation of solidification, Annu. Rev. Mater. Sci. 32 (2002) 163–194. https://doi.org/10.1146/annurev.matsci.32.101901.155803.

[63] M. Yang, L. Wang, W. Yan, Phase-field modeling of grain evolutions in additive manufacturing from nucleation, growth, to coarsening, Npj Comput. Mater. 7 (2021) 56. https://doi.org/10.1038/s41524-021-00524-6.

[64] L. Ma, H. Liu, A. Ramazani, M. Williams, L. Levine, A. Ramazani, Integrating Phase Field Modeling and Machine Learning to Develop Process-Microstructure Relationships in Laser Powder Bed Fusion of IN718, Metallogr. Microstruct. Anal. 13 (2024) 983–995. https://doi.org/10.1007/s13632-024-01130-w.

[65] M. Chen, Q. Du, R. Shi, H. Fu, Z. Liu, J. Xie, Phase field simulation of microstructure evolution and process optimization during homogenization of additively manufactured Inconel 718 alloy, Front. Mater. 9 (2022). https://doi.org/10.3389/fmats.2022.1043249.

[66] B. Radhakrishnan, S.B. Gorti, J.A. Turner, R. Acharya, J.A. Sharon, A. Staroselsky, T. El-Wardany, Phase field simulations of microstructure evolution in IN718 using a surrogate Ni–Fe–Nb alloy during laser powder bed fusion, Metals (Basel). 9 (2019). https://doi.org/10.3390/met9010014.

[67] M. Kühbach, L.A. Barrales-Mora, G. Gottstein, A massively parallel cellular automaton for the simulation of recrystallization, Model. Simul. Mater. Sci. Eng. 22 (2014) 075016. https://doi.org/10.1088/0965-0393/22/7/075016.

[68] C. Haase, M. Kühbach, L.A. Barrales-Mora, S.L. Wong, F. Roters, D.A. Molodov, G. Gottstein, Recrystallization behavior of a high-manganese steel: Experiments and simulations, Acta Mater. 100 (2015) 155–168. https://doi.org/10.1016/j.actamat.2015.08.057.

[69] M. Kühbach, G. Gottstein, L.A. Barrales-Mora, A statistical ensemble cellular automaton microstructure model for primary recrystallization, Acta Mater. 107 (2016) 366–376. https://doi.org/10.1016/j.actamat.2016.01.068.

[70] R. Ding, Z.X. Guo, Microstructural modelling of dynamic recrystallisation using an extended cellular automaton approach, Comput. Mater. Sci. 23 (2002) 209–218. https://doi.org/10.1016/S0927-0256(01)00211-7.

[71] C.-A. Gandin, M. Rappaz, A 3D Cellular Automaton algorithm for the prediction of dendritic grain growth, Acta Mater. 45 (1997) 2187–2195. https://doi.org/10.1016/S1359-6454(96)00303-5.

[72] A. Zinoviev, O. Zinovieva, V. Ploshikhin, V. Romanova, R. Balokhonov, On the numerical simulation of the microstructural evolution induced by laser additive

manufacturing of steel products, in: AIP Conf. Proc., American Institute of Physics Inc., 2016. https://doi.org/10.1063/1.4967154.

[73] S. Chen, Modélisation tridimensionnelle Automate Cellulaire - Éléments Finis (CAFE) pour la simulation du développement des structures de grains dans les procédés de soudage GTAW / GMAW, Http://Www.Theses.Fr. (2014). http://www.theses.fr/2014ENMP0010.

[74] W. Tan, Y.C. Shin, Multi-scale modeling of solidification and microstructure development in laser keyhole welding process for austenitic stainless steel, Comput. Mater. Sci. 98 (2015) 446–458. https://doi.org/10.1016/j.commatsci.2014.10.063.

[75] N. Mangelinck-Noël, J.E. Spinelli, C.A. Gandin, G. Reinhart, H. Nguyen-Thi, B. Billia, A method to determine the active particle nucleation undercooling distribution in a refined alloy, IOP Conf. Ser. Mater. Sci. Eng. 27 (2011). https://doi.org/10.1088/1757-899X/27/1/012090.

[76] J.T. Schwartz, J. von Neumann, A.W. Burks, Theory of Self-Reproducing Automata, Math. Comput. 21 (1967) 745. https://doi.org/10.2307/2005041.

[77] M.B. Cortie, E.M.L.E.M. Jackson, Simulation of the precipitation of sigma phase in duplex stainless steels, Metall. Mater. Trans. A Phys. Metall. Mater. Sci. 28 (1997) 2477–2484. https://doi.org/10.1007/s11661-997-0005-x.

[78] M. Rappaz, C.-A.A. Gandin, Probabilistic modelling of microstructure formation in solidification processes, Acta Metall. Mater. 41 (1993) 345–360. https://doi.org/10.1016/0956-7151(93)90065-Z.

[79] C.A. Gandin, M. Rappaz, R. Tintillier, Three-dimensional probabilistic simulation of solidification grain structures: Application to superalloy precision castings, Metall. Trans. A. 24 (1993) 467–479. https://doi.org/10.1007/BF02657334.

[80] C.-A. Gandin, M. Rappaz, A coupled finite element-cellular automaton model for

the prediction of dendritic grain structures in solidification processes, Acta Metall. Mater. 42 (1994) 2233–2246. https://doi.org/10.1016/0956-7151(94)90302-6.

[81] W. Kurz, B. Giovanola, R. Trivedi, THEORY OF ~I~ROSTRUCTURAL DEVELOPMENT DURING RAPID SOLIDIFICATION, 1986.

[82] A. Zinoviev, O. Zinovieva, V. Ploshikhin, V. Romanova, R. Balokhonov, Evolution of grain structure during laser additive manufacturing. Simulation by a cellular automata method, Mater. Des. 106 (2016) 321–329. https://doi.org/10.1016/j.matdes.2016.05.125.

[83] J. Eiken, B. Böttger, I. Steinbach, Multiphase-field approach for multicomponent alloys with extrapolation scheme for numerical application, Phys. Rev. E - Stat. Nonlinear, Soft Matter Phys. 73 (2006). https://doi.org/10.1103/PhysRevE.73.066122.

[84] Dipl.-Ing. Markus Tobias Kühbach, (2017).

[85] X. Ao, H. Xia, J. Liu, Q. He, Simulations of microstructure coupling with moving molten pool by selective laser melting using a cellular automaton, Mater. Des. 185 (2020). https://doi.org/10.1016/j.matdes.2019.108230.

[86] P. Mukhopadhyay, M. Loeck, G. Gottstein, A cellular operator model for the simulation of static recrystallization, Acta Mater. 55 (2007) 551–564. https://doi.org/10.1016/j.actamat.2006.08.045.

[87] C. Schäfer, G. Pomana, V. Mohles, G. Gottstein, O. Engler, J. Hirsch, Recrystallization modeling of AA8XXX alloys with cellular automata considering recovering kinetics, Adv. Eng. Mater. 12 (2010) 131–140. https://doi.org/10.1002/adem.201000026.

[88] O. Bittredge, H. Hassanin, M.A. El-Sayed, H.M. Eldessouky, N.A. Alsaleh, N.H. Alrasheedi, K. Essa, M. Ahmadein, Fabrication and Optimisation of Ti-6Al-4V

Lattice-Structured Total Shoulder Implants Using Laser Additive Manufacturing, Materials (Basel). 15 (2022). https://doi.org/10.3390/ma15093095.

[89] H.W. Hesselbarth, I.R. Göbel, Simulation of recrystallization by cellular automata, Acta Metall. Mater. 39 (1991) 2135–2143. https://doi.org/10.1016/0956-7151(91)90183-2.

[90] J. Li, X. Zhou, M. Brochu, N. Provatas, Y.F. Zhao, Y.F. Zhao, Solidification Microstruc-ture Simulation of Ti-6Al-4V in Metal Additive Manufacturing: A Review. Additive Manufacturing, (2020) 31. https://doi.org/10.1016/j.addma.2019.100989ï.

[91] M. Ghosh, R. Kumar, M. Saha, B.K. Sikdar, Cellular automata and its applications, Proc. - 2018 IEEE Int. Conf. Autom. Control Intell. Syst. I2CACIS 2018. (2019) 52–56. https://doi.org/10.1109/I2CACIS.2018.8603689.

[92] C.A. Reiter, Cyclic cellular automata in 3D, Chaos, Solitons and Fractals. 44 (2011) 764–768. https://doi.org/10.1016/j.chaos.2011.06.014.

[93] K. Hagihara, T. Nakano, Control of Anisotropic Crystallographic Texture in Powder Bed Fusion Additive Manufacturing of Metals and Ceramics—A Review, Jom. 74 (2021) 1760–1773. https://doi.org/10.1007/s11837-021-04966-7.

[94] A. Turnali, S.A.H. Motaman, Y. Chang, B. Böttger, A. Serafeim, L. Sayk, N.J. Peter, S. Richter, A. Schwedt, S. Höges, C. Haase, Evolution of microstructural heterogeneities in additively manufactured low-alloy steel, Addit. Manuf. 78 (2023). https://doi.org/10.1016/j.addma.2023.103859.

[95] W.A. de Morais, F.J.G. Landgraf, Crystallographic texture configured by laser powder bed fusion additive manufacturing process: a review and its potential application to adjust mechanical properties of metallic products, Tecnol. Em Metal. Mater. e Mineração. 20 (2023) e2802. https://doi.org/10.4322/2176-1523.20222802.

[96] J.J. Kuffner, Effective sampling and distance metrics for 3D rigid body path planning, Proc. - IEEE Int. Conf. Robot. Autom. 2004 (2004) 3993–3998. https://doi.org/10.1109/robot.2004.1308895.

[97] F. Bachmann, R. Hielscher, H. Schaeben, Texture analysis with MTEX- Free and open source software toolbox, Solid State Phenom. 160 (2010) 63–68. https://doi.org/10.4028/www.scientific.net/SSP.160.63.

[98] J.-J.F. B. Beausir, B. Beausir, J. Fundenberger, Analysis Tools for Electron and X-ray diffraction, ATEX723 software, Universite de Lorraine - Metz (2017)., (n.d.). www.atex-software.eu.

[99] J. Lipton, M.E. Glicksman, W. Kurz, Dendritic growth into undercooled alloy metals, Mater. Sci. Eng. 65 (1984) 57–63. https://doi.org/10.1016/0025-5416(84)90199-X.

[100] A.R.A. Dezfoli, W.S. Hwang, W.C. Huang, T.W. Tsai, Determination and controlling of grain structure of metals after laser incidence: Theoretical approach, Sci. Rep. 7 (2017) 1–11. https://doi.org/10.1038/srep41527.

[101] Z. Huang, W. Jia, H. Wang, Z. Yang, C. Li, J. Liang, Y. Zhong, A new heat source model for selective laser melting simulations based on energy distribution on the powder layer and the surface of substrate, (2021). https://doi.org/https://doi.org/10.48550/arXiv.2106.03482.

[102] G. Ivantsov, Temperature field around a spherical, cylindrical, and needle-shaped crystal, growing in a pre-cooled melt, (1985) 567–569, (n.d.). https://doi.org/https://ui.adsabs.harvard.edu/abs/1985tfas.rept..567I.

[103] R. Trivedi, Theory of dendritic growth during the directional solidification of binary alloys, J. Cryst. Growth. 49 (1980) 219–232. https://doi.org/10.1016/0022-0248(80)90157-8.

[104] W. Kurz, D.J. Fisher, Dendrite growth at the limit of stability: tip radius and

spacing, Acta Metall. 29 (1981) 11–20. https://doi.org/10.1016/0001-6160(81)90082-1.

[105] C.A.-A. Gandin, J.L.-L. Desbiolles, M. Rappaz, P. Thevoz, P. Thévoz, A three-dimensional cellular automation-finite element model for the prediction of solidification grain structures, Metall. Mater. Trans. A. 30 (1999) 3153–3165. https://doi.org/10.1007/s11661-999-0226-2.

[106] E. Villa, P.R. Rios, On modelling recrystallization processes with random growth velocities of the grains in materials science, Image Anal. Stereol. 31 (2012) 149–162. https://doi.org/10.5566/ias.v31.p149-162.

[107] R. Böhme, M. Brenner, T. Moore, M. Smith, Financial cryptography and data security, 2014. https://doi.org/10.1007/978-3-662-44774-1.

[108] B. Geveci, C. Law, ParaView : An End-User Tool for Large Data Visualization LA-UR-03-1560 Title : ParaView : An End-User Tool for Large Data Visualization Author (s): James Ahrens , Berk Geveci , Charles Law Submitted to : Technical Report, (2014).

[109] C. Suryanarayana, Non-equilibrium Processing of Materials, 1999.

[110] P. Köhnen, S. Ewald, J.H. Schleifenbaum, A. Belyakov, C. Haase, Controlling microstructure and mechanical properties of additively manufactured high-strength steels by tailored solidification, Addit. Manuf. 35 (2020) 101389. https://doi.org/10.1016/j.addma.2020.101389.

[111] S. Ghosh, J. Zollinger, M. Zaloznik, D. Banerjee, C.K. Newman, R. Arroyave, Modeling of hierarchical solidification microstructures in metal additive manufacturing: Challenges and opportunities, Addit. Manuf. 78 (2023) 103845. https://doi.org/10.1016/j.addma.2023.103845.

[112] P. Liu, Z. Wang, Y. Xiao, M.F. Horstemeyer, X. Cui, L. Chen, Insight into the mechanisms of columnar to equiaxed grain transition during metallic additive

manufacturing, Addit. Manuf. 26 (2019) 22–29. https://doi.org/10.1016/j.addma.2018.12.019.

[113] M. Bermingham, D. StJohn, M. Easton, L. Yuan, M. Dargusch, Revealing the Mechanisms of Grain Nucleation and Formation During Additive Manufacturing, Jom. 72 (2020) 1065–1073. https://doi.org/10.1007/s11837-020-04019-5.

[114] V.P. Narayana Samy, M. Schäfle, F. Brasche, U. Krupp, C. Haase, Understanding the mechanism of columnar–to-equiaxed transition and grain refinement in additively manufactured steel during laser powder bed fusion, Addit. Manuf. 73 (2023). https://doi.org/10.1016/j.addma.2023.103702.

[115] O.E. Lopez Botello, Simulation of Microstructural Evolution of Selective Laser Melting of Metal Powders, 2016.

[116] O. Zinovieva, A. Zinoviev, V. Romanova, R. Balokhonov, Three-dimensional analysis of grain structure and texture of additively manufactured 316L austenitic stainless steel, Addit. Manuf. 36 (2020). https://doi.org/10.1016/j.addma.2020.101521.

[117] T.F.W. van Nuland, J.A.W. van Dommelen, M.G.D. Geers, Microstructural modeling of anisotropic plasticity in large scale additively manufactured 316L stainless steel, Mech. Mater. 153 (2021) 103664. https://doi.org/10.1016/j.mechmat.2020.103664.

[118] A. Basak, S. Das, Epitaxy and Microstructure Evolution in Metal Additive Manufacturing, Annu. Rev. Mater. Res. 46 (2016) 125–149. https://doi.org/10.1146/annurev-matsci-070115-031728.

[119] P. Köhnen, M. Létang, M. Voshage, J.H. Schleifenbaum, C. Haase, Understanding the process-microstructure correlations for tailoring the mechanical properties of L-PBF produced austenitic advanced high strength steel, Addit. Manuf. 30 (2019). https://doi.org/10.1016/j.addma.2019.100914.

[120] J. Pauza, A. Rollett, Simulation Study of Hatch Spacing and Layer Thickness Effects on Microstructure in Laser Powder Bed Fusion Additive Manufacturing using a Texture-Aware Solidification Potts Model, J. Mater. Eng. Perform. 30 (2021) 7007–7018. https://doi.org/10.1007/s11665-021-06110-7.

[121] S.H. Sun, T. Ishimoto, K. Hagihara, Y. Tsutsumi, T. Hanawa, T. Nakano, Excellent mechanical and corrosion properties of austenitic stainless steel with a unique crystallographic lamellar microstructure via selective laser melting, Scr. Mater. 159 (2019) 89–93. https://doi.org/10.1016/j.scriptamat.2018.09.017.

[122] E. Gavagnin, J.P. Owen, C.A. Yates, Pair correlation functions for identifying spatial correlation in discrete domains, Phys. Rev. E. 97 (2018). https://doi.org/10.1103/PhysRevE.97.062104.

[123] R. Pyrz, Correlation of microstructure variability and local stress field in two-phase materials, Mater. Sci. Eng. A. 177 (1994) 253–259. https://doi.org/10.1016/0921-5093(94)90497-9.

[124] A.G. Demir, B. Previtali, Investigation of remelting and preheating in SLM of 18Ni300 maraging steel as corrective and preventive measures for porosity reduction, Int. J. Adv. Manuf. Technol. 93 (2017) 2697–2709. https://doi.org/10.1007/s00170-017-0697-z.

[125] Y. Chen, W. Wang, Y. Ou, D. Li, H. Chang, Y. Wu, R. Yang, Z. Zhai, C. Li, Effect of high preheating on the microstructure and mechanical properties of high gamma prime Ni-based superalloy manufactured by laser powder bed fusion, J. Alloys Compd. 960 (2023) 170598. https://doi.org/10.1016/j.jallcom.2023.170598.

[126] S. Qin, J. Saewe, J. Kunz, S. Herzog, A. Kaletsch, J.H. Schleifenbaum, C. Broeckmann, Influence of Preheating Temperature on Microstructure Evolution and Hardness of High-Speed Steel AISI M50 Processed by Laser Powder Bed

Fusion, Steel Res. Int. 94 (2023). https://doi.org/10.1002/srin.202200784.

[127] J. Chen, J. Xu, J. Moverare, L.A. Barrales-Mora, Effect of the building direction on the high-temperature mechanical properties of an IN738LC superalloy processed by laser-powder bed fusion, Mater. Sci. Eng. A. 909 (2024) 146756. https://doi.org/10.1016/j.msea.2024.146756.

[128] J. Chen, Crystal Plasticity Finite Element Modeling of Mechanical Properties in Laser Powder Bed Fusion Additive Manufacturing, Georgia Institute of Technology, 2026.

[129] G. Huang, T. Shen, B. Li, Microstructural evolution modelling and low-stress fatigue performance of bimodal-structured Al-Mg-Sc-Zr alloy produced by laser powder bed fusion additive manufacturing, Virtual Phys. Prototyp. 19 (2024) 1–22. https://doi.org/10.1080/17452759.2024.2346287.

[130] L.R. Chen, X.Z. Xiao, L. Yu, H.J. Chu, H.J. Chu, H.L. Duan, Texture evolution and mechanical behaviour of irradiated face-centred cubic metals, Proc. R. Soc. A Math. Phys. Eng. Sci. 474 (2018) 20170604. https://doi.org/10.1098/rspa.2017.0604.

[131] F. Roters, P. Eisenlohr, L. Hantcherli, D.D. Tjahjanto, T.R. Bieler, D. Raabe, Overview of constitutive laws, kinematics, homogenization and multiscale methods in crystal plasticity finite-element modeling: Theory, experiments, applications, Acta Mater. 58 (2010) 1152–1211. https://doi.org/10.1016/j.actamat.2009.10.058.

[132] S.R. Kalidindi, Incorporation of deformation twinning in crystal plasticity models, J. Mech. Phys. Solids. 46 (1998) 267–290. https://doi.org/10.1016/S0022-5096(97)00051-3.

[133] F. Roters, M. Diehl, P. Shanthraj, P. Eisenlohr, C. Reuber, S.L. Wong, T. Maiti, A. Ebrahimi, T. Hochrainer, H.-O. Fabritius, S. Nikolov, M. Friák, N. Fujita, N. Grilli,

K.G.F. Janssens, N. Jia, P.J.J. Kok, D. Ma, F. Meier, E. Werner, M. Stricker, D. Weygand, D. Raabe, DAMASK – The Düsseldorf Advanced Material Simulation Kit for modeling multi-physics crystal plasticity, thermal, and damage phenomena from the single crystal up to the component scale, Comput. Mater. Sci. 158 (2019) 420–478. https://doi.org/10.1016/j.commatsci.2018.04.030.

[134] S.L. Wong, M. Madivala, U. Prahl, F. Roters, D. Raabe, A crystal plasticity model for twinning- and transformation-induced plasticity, Acta Mater. 118 (2016) 140–151. https://doi.org/10.1016/j.actamat.2016.07.032.

[135] M.G. Jiang, Z.W. Chen, J.D. Tong, C.Y. Liu, G. Xu, H.B. Liao, P. Wang, X.Y. Wang, M. Xu, C.S. Lao, Strong and ductile reduced activation ferritic/martensitic steel additively manufactured by selective laser melting, Mater. Res. Lett. 7 (2019) 426–432. https://doi.org/10.1080/21663831.2019.1631224.

[136] J. Hirsch, E. Aryshesnkij, S. Konovalov, Slip System Selection and Taylor Factor Evolution in FCC Metals, SSRN Electron. J. (2020). https://doi.org/10.2139/ssrn.3618715.

[137] I. Salehinia, D.F. Bahr, Crystal orientation effect on dislocation nucleation and multiplication in FCC single crystal under uniaxial loading, Int. J. Plast. 52 (2014) 133–146. https://doi.org/10.1016/j.ijplas.2013.04.010.

[138] W.F. Hosford, Mechanical Behavior of Materials,2nd Edition, 2nd ed., 2009.

[139] F. Liu, W.J. Dan, W.G. Zhang, Strain hardening model of TWIP steels with manganese content, Mater. Sci. Eng. A. 674 (2016) 178–185. https://doi.org/10.1016/j.msea.2016.07.115.

[140] I. Janeiro, O. Hubert, J.H. Schmitt, In-situ strain induced martensitic transformation measurement and consequences for the modeling of medium Mn stainless steels mechanical behavior, Int. J. Plast. 154 (2022) 103248. https://doi.org/10.1016/j.ijplas.2022.103248.

Extended Summaries in French

La fabrication additive (FA) est une technique de fabrication innovante permettant de réaliser aisément des composants complexes avec une efficacité matière élevée et une flexibilité de conception considérable. Contrairement aux méthodes soustractives traditionnelles, la FA construit les pièces couche par couche, ce qui autorise la fabrication de géométries complexes qui seraient autrement difficiles, voire impossibles, à produire [1]. Cette nouveauté qu'apporte la FA a suscité, au cours des deux dernières décennies, d'intenses efforts de recherche dans ce domaine. La fabrication additive est initialement apparue comme un outil de prototypage. Cependant, avec le développement de procédés tels que la fusion sur lit de poudre par laser (Laser Powder Bed Fusion, LPBF), la déposition directe d'énergie (Direct Energy Deposition, DED) et la fusion par faisceau d'électrons (Electron Beam Melting, EBM), la FA a évolué pour inclure la fabrication additive métallique (FAM), laquelle est, à notre époque, envisagée comme un substitut potentiel aux techniques de fabrication conventionnelles [2]. Dans des secteurs tels que l'aéronautique, l'automobile ou le biomédical, où les composants doivent répondre à des spécifications très strictes et parfois présenter des géométries extrêmement complexes, la transition des procédés conventionnels vers la fabrication additive métallique (FAM) a déjà commencé [3]. La technique LPBF est un type de FAM qui utilise un laser de haute qualité comme source d'énergie afin de fusionner sélectivement des poudres métalliques et de créer des composants tridimensionnels [4].

Parmi toutes les techniques de FA, la LPBF s'est imposée comme une méthode de référence pour la production de pièces métalliques proches de la forme nette (near-net-shape). La LPBF emploie un faisceau laser qui balaye la couche de poudre selon une trajectoire contrôlée, provoquant la fusion et la solidification locale du matériau. En tant que procédé de fabrication couche par couche, la LPBF peut produire des pièces de toute

conception et structure complexes, ce qui en fait une technique particulièrement prisée des industriels [5–7].

L'un des avantages essentiels de la LPBF réside également dans sa capacité à ajuster localement les propriétés mécaniques en contrôlant la microstructure. Ce potentiel découle de l'apport thermique extrêmement localisé du procédé, qui permet aux concepteurs d'affiner la microstructure dans des zones spécifiques d'un composant. En ajustant la vitesse de balayage, l'espacement des passes (hatch spacing) ou la puissance laser, il est possible de favoriser de façon intentionnelle la croissance de grains colonnaires ou équiaxes, permettant ainsi d'optimiser les performances localement au sein d'une même pièce [8] . De plus, il est envisageable de modifier la composition chimique locale afin d'obtenir des matériaux à gradients de propriétés. Par conséquent, la compréhension des mécanismes qui gouvernent l'évolution microstructurale au cours de la LPBF est un sujet d'intérêt majeur.

Bien que la LPBF offre des capacités de fabrication et une flexibilité de conception exceptionnelles, elle n'a pas encore atteint son plein potentiel. L'un des principaux défis concerne la microstructure, la texture et les propriétés mécaniques des composants produits par LPBF, qui diffèrent souvent de manière notable de celles obtenues par les procédés conventionnels [9,10]. Ces écarts s'expliquent principalement par les vitesses de solidification rapides et les gradients thermiques élevés inhérents au procédé LPBF. Par ailleurs, la gamme de matériaux pouvant être traités par LPBF reste limitée, ce qui constitue un autre défi majeur auquel la FA est confrontée aujourd'hui. En pratique, un programme expérimental rigoureux est élaboré chaque fois qu'un nouveau matériau doit être mis en œuvre avec la LPBF.

En outre, la LPBF implique de nombreux paramètres de procédé, tels que la puissance laser, la vitesse de balayage, l'espacement entre les passes et l'épaisseur de

couche, qui génèrent un espace paramétrique vaste, rendant quasi impossible la réalisation d'études expérimentales exhaustives [6,7,9,11].

Pour surmonter ces limitations, les techniques de modélisation computationnelle sont de plus en plus utilisées comme alternatives ou compléments aux travaux expérimentaux. Diverses approches de modélisation ont été proposées, notamment le Phase Field (PF) [12,13], le Kinetic Monte Carlo (KMC) [14,15] et l'automate cellulaire (Cellular Automaton, CA) [16–20], chacune présentant ses propres capacités et limites. Les modèles PF permettent de simuler en détail la croissance dendritique et la redistribution des solutés, mais ils sont coûteux en calcul et limités en échelle [21]. Les modèles KMC offrent une efficacité statistique et une bonne évolutivité, mais ne couplent pas explicitement les champs cristallographiques [12]. Les modèles CA constituent un compromis en permettant des simulations relativement efficaces tout en capturant des phénomènes physiques importants tels que la morphologie des grains et l'évolution de la texture [22,23].

Néanmoins, les modèles CA existants présentent deux limites majeures : (i) la nécessité de maillages haute résolution pour capturer les fines structures dendritiques, ce qui augmente la charge de calcul, et (ii) l'absence de stratégies efficaces pour gérer les cycles de refusion, qui constituent un aspect fondamental du procédé LPBF. Comme le suggèrent études, jusqu'à 80 % du volume construit peut subir une refusion, ce qui introduit une redondance computationnelle et allonge significativement le temps de simulation [24]. Bien que des stratégies de parallélisation aient été adoptées pour maîtriser la charge computationnelle liée aux tailles de cellules fines [16,25], il existe un déficit notable de littérature traitant spécifiquement la redondance engendrée par les cycles répétés de refusion-solidification.

Dans ce contexte, l'objectif principal de cette thèse est de développer un cadre de modélisation accéléré, combinant Éléments Finis (EF) et Automate Cellulaire (AC),

spécifiquement adapté au procédé LPBF**.** Cet objectif général se décline en quatre axes spécifiques :

1. Éliminer la redondance computationnelle associée aux cycles de refusion grâce à l'introduction d'un algorithme de suivi tenant compte de la refusion. Cet algorithme enregistre l'historique thermique de chaque cellule et ne traite que l'événement final de solidification, aboutissant au développement d'un modèle d'Automate Cellulaire conscient de la refusion (RA-CA)**.**
2. Améliorer l'efficacité computationnelle par la parallélisation du cadre développé à l'aide de l'interface MPI (Message Passing Interface), afin de simuler des domaines représentatifs de grande taille.
3. Intégrer une physique microstructurale réaliste via l'implémentation d'un mécanisme de nucléation stochastique et d'un modèle de croissance cinétique gouverné par les gradients thermiques locaux et l'orientation cristallographique.
4. Établir un lien Procédé–Structure–Propriété (P–S–P) en couplant les microstructures simulées avec des calculs CP-FEM afin d'évaluer leur influence sur le comportement mécanique.

La thèse est structurée en six chapitres :

- Chapitre 1 : présentation de l'état de l'art relatif à la LPBF et aux approches de modélisation microstructurale.
- Chapitre 2 : développement du modèle RA-CA et description détaillée de l'algorithme conscient de la refusion.
- Chapitre 3 **:** études paramétriques menées à l'aide du RA-CA, portant sur l'effet de la densité de nucléation, des coefficients de croissance et des conditions thermiques. Les résultats mettent en évidence des microstructures réalistes, avec des grains colonnaires le long des frontières de bain de fusion et des grains

équiaxes en zone centrale, confirmant la capacité du modèle à reproduire le comportement attendu en LPBF.

- Chapitre 4 : validation du RA-CA par confrontation avec des données expérimentales (EBSD). Les comparaisons portant sur la morphologie, l'orientation, la distribution de taille des grains et la fonction de corrélation montrent un bon accord, attestant de la crédibilité du modèle.
- Chapitre 5 : application du RA-CA à l'étude du préchauffage en LPBF. Les simulations réalisées à différentes températures montrent l'impact du préchauffage sur les gradients thermiques, le raffinement des grains et la texture. Les microstructures simulées sont ensuite couplées à des calculs CP-FEM afin de relier les évolutions microstructurales aux propriétés mécaniques. Ce chapitre illustre pleinement le lien Procédé–Structure–Propriété.
- Chapitre 6 : conclusion de la thèse. Les contributions majeures sont synthétisées : élimination de la redondance liée à la refusion, gains notables en efficacité, reproduction fidèle des microstructures de la LPBF, validation expérimentale et démonstration de l'effet du préchauffage sur le lien P–S–P. Les limites identifiées (validation restreinte à un seul alliage, hypothèses simplifiées de nucléation) sont discutées, et des perspectives sont proposées, notamment l'extension à d'autres alliages et l'intégration de la modélisation des défauts.

Chapitre 1

Revue de la littérature.

Le Chapitre 1 présente le contexte de la fabrication additive et plus particulièrement du procédé LPBF. Une revue de littérature détaillée est proposée sur différentes techniques de modélisation telles que le Phase Field, le Kinetic Monte Carlo et l'Automate Cellulaire. Le procédé LPBF repose essentiellement sur la fusion et la solidification, et les concepts liés à la solidification et à l'évolution microstructurale y sont également expliqués. Le procédé LPBF est l'un des principaux procédés de fabrication additive (FA), dans lequel un faisceau laser en mouvement fond sélectivement une poudre métallique pour construire un objet 3D couche par couche. Une analyse détaillée des différentes techniques de modélisation ,Phase Field, Kinetic Monte Carlo et Automate Cellulaire est présentée, avec leurs forces et leurs limites. Sur la base de l'état de l'art, ce chapitre conclut que l'Automate Cellulaire constitue l'approche la plus appropriée pour modéliser l'évolution microstructurale en LPBF, offrant un compromis entre coût computationnel et niveau de détail requis.

Chapitre 2

Développement d'un modèle 3D d'automate cellulaire conscient de la refusion (RA-CA)

Le Chapitre 2 décrit en détail le modèle développé. L'approche de modélisation par Automate Cellulaire (AC) est un cadre computationnel efficace et polyvalent, adapté à la simulation des processus d'évolution microstructurale caractéristiques de la FA. Fondamentalement, un AC est un modèle mathématique régi par un ensemble de règles de transition déterministes et/ou probabilistes, ce qui lui permet de représenter avec précision l'évolution spatiale et temporelle des systèmes physiques. Dans le cas de la solidification — phénomène dominant en FA — les modèles AC intègrent les mécanismes de nucléation et de croissance cristalline, en tenant compte des orientations cristallographiques (texture) et du champ thermique. Ces constituants influencent fortement l'évolution microstructurale et doivent être représentés par des sous-modèles et des stratégies de calcul appropriés pour garantir la précision des prédictions. Ce chapitre expose en détail le modèle AC développé, ses mécanismes, ses algorithmes de calcul et les interactions entre ses composantes essentielles.

Chapitre 3

Validation du modèle

Le Chapitre 3 présente la validation du modèle RA-CA développé au Chapitre 2. Avant toute application pratique et comparaison expérimentale, il est nécessaire de vérifier que le modèle se comporte de manière stable et physiquement cohérente dans des conditions représentatives de la LPBF. Deux facteurs critiques influençant la morphologie et la texture des grains en LPBF sont la nucléation et la cinétique de croissance. Étant donné que le modèle RA-CA introduit une approche novatrice pour

gérer les cycles de refusion-solidification, il est important d'évaluer sa capacité à reproduire correctement les effets des mécanismes de nucléation et le développement spatial des grains. Pour cela, ce chapitre explore la réponse du modèle selon différents scénarios de nucléation volumique, épitaxiale et mixte, ainsi que différentes cinétiques de croissance. L'objectif est de vérifier la capacité du modèle à capturer la solidification directionnelle, la compétition entre grains et la formation de structures équiaxes. Le matériau choisi pour toutes les simulations est l'acier austénitique X30Mn21, à structure FCC monophasée, utilisé également dans la validation expérimentale (Chapitre 4) et l'étude du lien P–S–P (Chapitre 5).

Chapitre 4

Développement microstructural dans un acier traité par LPBF

La crédibilité des modèles numériques de microstructure repose sur leur alignement avec les observations expérimentales. Dans ce chapitre, la précision du modèle RA-CA est évaluée en comparant les structures de grains simulées avec des résultats expérimentaux. Des éprouvettes ont été fabriquées par LPBF et analysées par diffraction des électrons rétrodiffusés (EBSD). Elles ont été préparées à l'Institut de l'Acier de l'Université RWTH Aachen (Allemagne). En parallèle, le modèle RA-CA a été utilisé pour simuler la microstructure dans les mêmes conditions de procédé, avec deux résolutions spatiales différentes afin d'évaluer la sensibilité à la taille des cellules. Le matériau étudié est le même que dans le Chapitre 3, à savoir l'acier austénitique (FCC) monophasé X30Mn21. Ce chapitre propose une comparaison structurée entre simulations et expériences, en mettant l'accent à la fois sur les caractéristiques qualitatives (morphologie des grains, orientation cristallographique) et sur les métriques quantitatives (distribution de taille de grains, rapport d'aspect, intensité texturale).

Chapitre 5

Effet du préchauffage sur la microstructure et les relations propriétés

Comme mentionné au Chapitre 1, le procédé LPBF est largement utilisé pour le traitement de nouveaux matériaux et la fabrication de conceptions complexes. Toutefois, les vitesses de refroidissement rapides et les gradients thermiques élevés associés au procédé entraînent la formation de microstructures particulières, avec des répercussions sur les propriétés mécaniques. Le préchauffage du plateau est souvent considéré comme une stratégie efficace pour réduire ces gradients, améliorer la stabilité de la solidification et influencer la morphologie des grains, la texture et le comportement mécanique [124,125]. De plus, le préchauffage contribue à réduire les contraintes thermiques et, dans certains cas, les défauts de porosité.

Ce chapitre présente une étude numérique de l'effet du préchauffage sur les structures de grains de l'acier austénitique X30Mn21 (AHSS) fabriqué par LPBF. Le modèle RA-CA a été couplé à des champs thermiques intégrant différentes températures de préchauffage. L'objectif n'était pas seulement d'observer l'impact du préchauffage sur la microstructure, mais aussi d'évaluer si les résultats simulés pouvaient être utilisés pour établir des liens Procédé–Structure–Propriété (P–S–P). À cette fin, en complément des simulations microstructurales, le comportement mécanique a été étudié. Les prédictions contrainte–déformation ont été obtenues à l'aide de la méthode CP-FEM (Crystal Plasticity Finite Element Method). Ces simulations CP-FEM ont été réalisées par J. Chen [127] dans le cadre de sa thèse doctorale [128], et les résultats ont été intégrés pour établir les liens P–S–P et valider la précision des prédictions.

Chapitre 6

Conclusion générale et perspectives

Cette thèse propose un cadre numérique complet et efficace pour prédire l'évolution microstructurale en LPBF. L'objectif était de développer un modèle d'Automate Cellulaire conscient de la refusion (RA-CA), rapide et physiquement cohérent, capable de gérer les redondances computationnelles induites par les cycles répétés de refusion et de solidification. Cela a été réalisé grâce à l'introduction d'un algorithme spécifique dans le cadre AC conventionnel, qui enregistre le temps de solidification final de chaque cellule, améliorant ainsi l'efficacité numérique sans compromettre la précision physique.

L'une des caractéristiques majeures de ce cadre est sa stratégie d'assignation des orientations aux grains nucléés. Les orientations sont systématiquement alignées avec le gradient thermique local, ce qui permet au modèle de reproduire l'anisotropie des grains typiquement observée dans les pièces métalliques fabriquées par LPBF. Les performances du modèle ont été testées pour différentes stratégies de nucléation, montrant des réponses cohérentes avec les tendances de solidification rapportées dans la littérature : formation de grains équiaxes avec nucléation volumique et grains colonnaires avec nucléation épitaxiale. La robustesse du modèle a été confirmée par une comparaison approfondie avec des données EBSD sur l'acier X30Mn21 fabriqué par LPBF. Les caractéristiques simulées (morphologie, distribution de taille de grains, texture) se rapprochent fortement des résultats expérimentaux.

Grâce à son algorithme de suivi de refusion, le modèle RA-CA est au moins 30 % plus rapide qu'un AC conventionnel pour la LPBF. Son efficacité a été encore renforcée par la parallélisation MPI, qui augmente considérablement la vitesse de calcul et ouvre la voie à des simulations à l'échelle de la pièce.

Le cadre a également été appliqué à l'étude de l'influence du préchauffage. Il a montré sa capacité à prédire les transitions de morphologie et d'orientation des grains en fonction des apports thermiques, confirmant sa fiabilité comme outil prédictif. En outre, il a permis d'établir des liens P–S–P : les microstructures simulées par RA-CA ont été couplées à des calculs CP-FEM, capables de reproduire l'influence de la taille des grains et de la texture cristallographique sur la limite d'élasticité de l'alliage X30Mn21.

Bien que la validation se soit concentrée sur l'acier à haute teneur en manganèse X30Mn21, le cadre RA-CA développé n'est pas limité à ce matériau. En principe, il peut être appliqué à tout alliage monophasé traité par LPBF. Les cinétiques de croissance peuvent être recalculées en fonction des propriétés thermophysiques pertinentes, et les paramètres de nucléation ajustés selon la chimie de l'alliage et les conditions de procédé, ce qui confère au modèle une large généralisabilité.

Limites du modèle actuel

Malgré son efficacité, le modèle RA-CA présente certaines limites :

- Il se concentre exclusivement sur l'évolution des grains pilotée par la solidification et n'intègre pas les phénomènes de recristallisation statique ou dynamique.
- Les simulations se limitent aux zones fondues et resolidifiées ; la zone affectée thermiquement (ZAT), pourtant fréquente en LPBF, n'est pas représentée.
- La redistribution des solutés et les effets de ségrégation ou de formation de phases secondaires ne sont pas pris en compte.
- Le modèle est de nature mésoscopique (échelle du grain) et ne considère pas la dynamique des dislocations ; il ne peut donc pas prédire directement la densité de dislocations.

Perspectives

À partir de ces limites, plusieurs axes de développement sont identifiés :

1. Intégration avec des modèles multiphasiques et de précipitation
   De nombreux alliages avancés utilisés en FA, tels que les systèmes aluminium–scandium, sont fortement influencés par la précipitation. Le couplage du RA-CA avec des modèles de précipitation permettrait une description plus complète de l'évolution microstructurale dans ces alliages complexes.
2. Modèles substituts basés sur l'apprentissage automatique

   Le RA-CA peut générer de vastes ensembles de données reliant conditions de procédé, microstructures et propriétés mécaniques (via CP-FEM). Ces bases peuvent servir à entraîner des modèles d'apprentissage automatique capables de prédire la morphologie des grains, la texture et le comportement mécanique sans recourir à une simulation complète. Cela permettrait un criblage plus rapide des fenêtres de procédé et ouvrirait la voie à une optimisation en temps réel.

3. Optimisation de l'efficacité parallèle

   Bien que la logique consciente de la refusion améliore les temps de calcul, des pertes d'efficacité apparaissent à haut nombre de processeurs en raison de déséquilibres de charge liés à la décomposition statique du domaine. L'adoption de stratégies dynamiques de décomposition spatiale pourrait améliorer l'efficacité et la scalabilité du modèle pour des simulations à grande échelle.